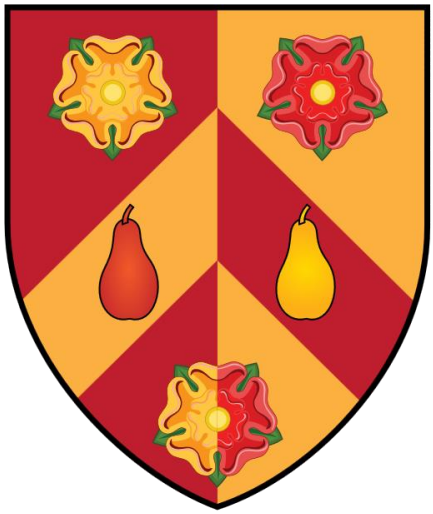
# A High Resolution Electron Backscatter Diffraction Study of Heterogeneous Deformation in Polycrystal Copper


## Jun Jiang






**Wolfson College**

**Department of Materials**

**The University of Oxford**


**Trinity Term 2013**

**Supervisor: Angus. J. Wilkinson**

A thesis submitted for the degree of

Doctor of Philosophy

# Abstract

**Title**: A High Resolution Electron Backscatter Diffraction Study of Heterogeneous Deformation in Polycrystal Copper

**Author**: Jun Jiang, Wolfson College

**Degree**: Doctor of Philosophy

**Date of Submission**: Trinity Term 2013

Understanding the plastic deformation mechanisms in polycrystals is a long-standing fundamental problem and its improvement has significant potential impact on the increase in materials resistance to typical failure modes such as fatigue cracking and stress corrosion cracking and hence the increase in the materials strength. However many deformation models are yet to be validated as quantitative experimental results at mesoscale to correlate dislocations and microstructure features are limited.

This thesis furthers the High Resolution EBSD (HR-EBSD) technique in Geometrically Necessary Dislocation (GND) density measurement from qualitative analysis with a typical map size of 100 μm x100 μm to quantitative analysis with a map of 500 μm x500 μm by determining the optimised scanning step size (0.5 μm) and detector binning level (4x4 binning). This allows a statistically large number of grains to be sampled. Combining with obtained crystallographical information from a conventional EBSD system, systematic studies on GNDs behaviours with respect to a range of microstructure features such as grain boundaries and triple junctions were conducted on monotonically deformed polycrystal copper samples under tension. Relatively high GND density points were found near triple junctions and some grain boundaries whereas the low GND density points tend to appear near the grains' interiors. These tendencies are particularly profound in low and moderately deformed samples. Hence more detailed analyses were performed to investigate the relations of GND density and the properties of grain boundaries and triple junctions.

These quantitative analyses were complemented with direct visual assessment. The visual inspection provides interesting findings such as the strong GND structure dependence on grain orientations and GND structure development through increasing deformation; grain-grain interaction influences on GND structure development and GND structures near triple junctions. These GND density studies provide experimental results to validate some of the existing plastic deformation models for instance Ashby's model of hardening and Hall-Petch relation. However, some of the new observations on GND structures at mesoscale cannot be fully rationalised by existing proposed mechanisms. Hence new models have been proposed that these GND structures might be generated from the intersections of different slip systems which occurred in various parts of a grain, or by the dislocation piling-up at some microstructural features e.g. triple junctions and twin boundaries.

# Preface

This doctoral thesis is an account of the work carried out by the author in the Department of Materials, the University of Oxford between October 2009 and June 2013 under the supervision of Prof Angus Wilkinson. All the work is original. No part of this thesis has been submitted or accepted for any other degree at this university or elsewhere.

Parts of this work have been presented in the following peer reviewed journals and conferences:

## Publications:

Jun Jiang, Ben Britton and Angus Wilkinson (2012): **Accumulation of Geometrically Necessary Dislocations near Grain Boundaries in Deformed Copper**, published in Philosophical Magazine Letters. DOI: 10. 1080/09500839.2012.700412

J Jiang, T.B.Britton and A.J. Wilkinson (2012): **Measurement of Geometrical Necessarily Dislocation Density with High Resolution Electron Backscatter Diffraction: Effects of Detector Binning and Step Size**, published in Ultramicroscopy, ULTRAM-S-12-00267. DOI: 10.1016/j.ultramic.2012.11.003

Jun Jiang, Ben Britton & Angus J. Wilkinson (2013): **Evolution of dislocation density distributions in Copper during tensile deformation,** published in Acta Materialia. DOI:10.1016/j.actamat.2013.8.27

Jun Jiang, Ben Britton & Angus J. Wilkinson (2013): **Mapping type III intra-granular residual stress distributions in deformed copper polycrystals,** published in Acta Materialia. DOI:10.1016/ j.actamat.2013.06.038

T.B. Britton, J.Jiang, R. Clough, E. Tarleton, A.I. Kirkland and A.J. Wilkinson(2013): **Assessing the precision of strain measurements using electron backscatter diffraction - Part 1: Detector assessment,** published in Ultramicroscopy. DOI:10.1016/j.ultramic.2013.08.005

T.B. Britton, J.Jiang, R. Clough, E. Tarleton, A.I. Kirkland and A.J. Wilkinson(2013): **Assessing the precision of strain measurements using electron backscatter diffraction - Part 2: Experimental Demonstration**, published in Ultramicroscopy. DOI:10.1016/j.ultramic.2013.08.006

T Ben Britton, Jun Jiang, Phani S Karamched and Angus J Wilkinson (2013) **Probing deformation and revealing microstructural mechanisms with cross correlation based high resolution electron backscatter diffraction (HR-EBSD)**, published in JOM. DOI: 10.1007/s11837-013-0680-6

## Conferences:

EBSD 2013 The Oxford University, Oxford, UK, 26th-28th March 2013

J. Jiang T.B. Britton and A.J. Wilkinson: **A Study of the evolution of geometrically necessary dislocation density using high resolution EBSD**

International Conference on Strength of Materials, India Institute of Science, Bangalore, India, 20th -26th August

J. Jiang T.B. Britton and A.J. Wilkinson: **Geometrically necessary dislocations distributions in polycrystal Copper after monotonic and cyclic deformation**

EBSD 2012 National Physical Laboratory, Teddington, UK, 26th-28th March 2012

J. Jiang T.B. Britton and A.J. Wilkinson: **Sampling Issues in mapping of geometrically necessary dislocation density distribution in deformed polycrystals**

EBSD 2011 Max-Planck Institute, Dusseldorf, Germany, 28-31 March 2011

J. Jiang T.B. Britton and A.J. Wilkinson: **Evolution of geometrically necessary dislocation distributions during tensile and cyclic deformation of close packed cubic polycrystals**

# Acknowledgements

This thesis could not have been accomplished without the constant guidance, support and help from the best supervisor, Prof Angus Wilkinson and my gifted colleague Dr Ben Britton. Angus and Ben have always been patient and supportive as mentors as well as friends. They showed me the beautiful and exciting side of research. Their passion and enthusiasm on research really inspired me to pursue a research career. I would like to express my deep and sincere gratitude to them for giving me the most enjoyable research experience over the last 4 years.

This work has been greatly benefitted from the contributions of many colleagues and friends. I would like to particularly thank Prof Fionn Dunn, Prof Mike Ashby, Prof Dierk Raabe, Prof David Dingley, Dr Ken Mingard, Dr Graham Meaden, Dr Shirley Northover, Dr David Collins, Dr Ed Tarleton for their interest, advice and helpful discussion on dislocation studies and EBSD development.

The Oxford Micromechanics group has provided a wonderful working atmosphere. I would like to thank them all for helpful discussions and making work enjoyable over the last four year. I would also like to thank my office colleagues, particularly Mahmoud Mostafav and Alisa Stratulat Shuangqing for continued moral support and refreshment.

I would like to thank my basketball teammates: Chen Qi, Wu Guo, Sun Xiaodan, Fei Tianyu, Fang Jiangliang, He Weisong for ensuring that I have fun games outside of labs in the past four years. Also thanks to Wolfson college for providing excellent basketball facilities. I really appreciate the College's constant support given to my basketball team in the past four years.

Further thanks to my close friends met in Oxford: Yi Xiaoou, Jiang Meng, Jiang Xia, He Shuaishuai, Li Tong, Zou Xin, Yang Ke, Chen Xi, Xu Wei, Song Junfang for their support and bringing me a lot of cheer.

Finally I am eternally gratefully to my beloved wife Song Helen, great parents: Yunde and Xiucui, my lovely brother Jiang shuai and Helen's parents. Without their endless love and encouragement, I could never have reached this far.

# Contents

Abstract .....I

Preface .....II

Acknowledgements..... IV

Chapter 1. Introduction .....1

Chapter 2. Literature Review .....9

2.1 Theoretical approaches .....9

2.1.1 Plastic deformation in single crystal Face Centred Cubic (FCC) metals……..……10

2.1.2 Deformation mechanisms in polycrystals .....12

2.2 Experimental observations .....27

2.2.1 Slip line observations .....27

2.2.2 TEM observations .....28

2.2.3 Grain orientation dependence .....33

2.2.4 X-ray diffraction Topography .....34

2.2.5 EBSD and HR-EBSD plastic deformation study.....36

2.3 High resolution EBSD .....45

2.4 Analysis for GND content .....51

Chapter 3. GND Density Measurement Sensitivity: Effects of Detector Binning and Step Size .....58

3.1 Binning size effect .....59

3.1.1 Baseline measurement on Si .....60

3.1.2 Analysis of deformed Cu polycrystal .....66

3.2 Step size effect .....71

3.2.1 Baseline measurement on Si .....72

3.2.2 Analysis of deformed Cu polycrystal .....74

3.3 Conclusion.....78

Chapter 4. Quantitative Analyses on GND Density Distributions and Evolution (I)….....79
4.1 Experimental method.....80
4.2 Results.....83
4.2.1 GND density maps.....83
4.2.2 Evolution of GND distribution with increasing strain.....85
4.2.3 Relation between flow stress and average GND density .....90
4.2.4 GND density distribution with respect to grain boundaries.....91
4.2.5 GND density distribution with respect to triple junctions.....94
4.2.6 Grain averaged GND density with respect to grain size.....96
4.3 Discussion .....98
4.4 Conclusions.....104
Chapter 5. Quantitative Analyses on GND Density Distribution and Evolution (II)….....106
5.1 Analytical method .....108
5.1.1 Taylor factor .....108
5.1.2 Schmid factor .....110
5.1.3 Grain boundary inclination angle with regard to loading axis ...112
5.1.4 Grain boundary disorientation angle .....115
5.2 Results.....120
5.2.1 Texture.....120
5.2.2 Taylor Factor.....124
5.2.3 Schmid Factor.....126
5.2.4 Inclination angle .....129
5.2.5 Disorientation angle .....131
5.3 Discussion .....133
5.4 Conclusions.....139
Chapter 6. Qualitative Analysis of Dislocation Structures.....141

6.1 Analytical methods ..... 142
6.1.1 Grain orientation dependence ..... 142
6.1.2 Annealing twins ..... 144
6.1.3 Triple junctions ..... 146
6.2 Results ..... 148
6.2.1 Characteristic deformation microstructures ..... 148
6.2.2 Grain orientation and deformation microstructures ..... 152
6.2.3 Grain-grain interactions ..... 155
6.2.4 Annealing twins ..... 159
6.2.5 Triple junctions ..... 162
6.3 Discussion ..... 168
6.3.1 Characteristic deformation microstructures ..... 168
6.3.2 Grain orientation dependence ..... 169
6.3.3 Grain-grain interactions ..... 171
6.3.4 Twin boundaries ..... 173
6.3.5 Triple junctions ..... 174
6.4 Conclusion ..... 176
Chapter 7. Summary ..... 178
References ..... 182

***"It (work hardening) is the first problem to be attempted by dislocation theory and may be the last to be solved" ---------- Cottrell 1953***

# Chapter 1. Introduction

Polycrystal metals consisting of numerous grains with various crystal orientations are widely used in virtually all common engineering systems as in most of the cases polycrystal metals possess higher yield stress and higher ultimate strength than single crystal. With the emergence of dislocation theory, mechanical behaviour in metals has been rationalised. Extensive studies have been carried out on dislocation mechanisms during plastic deformation in crystals including dislocation movement, interaction, storage, and nucleation.

In single crystals, the dislocation based theories for work hardening have been well established with sufficient experimental evidence. It is well known that the randomly trapped and stored dislocations are responsible for work hardening processes [1]. However, even though more than a century has past, the dislocation mechanisms for work hardening processes in polycrystals still remain elusive [2].

Various theories or models have been proposed to address the equilibrium or compatibility conditions in polycrystals to explain the observed work hardening phenomena [3-5]. For example, Ashby described dislocations can be classified as statistical stored dislocation (SSD) and geometrically necessary dislocations (GNDs) [1]. SSDs are formed due to mutually trapped dislocations existing as forms of dipoles and multipoles; whereas GNDs are generated as excess dislocations within a Burgers circuit to satisfy

geometrical compatibility. Ashby proposed that the stored SSDs in single crystals play a predominating role in work hardening for the more homogenous deformation of single crystals by acting as obstacles to hinder the movement of additional dislocations on active slip planes. However, for inhomogeneous deformation in polycrystals, GNDs are generated rapidly and at some point will exceeds SSD density and thus dominate work hardening processes.

Ashby's model begins by considering that individual grains in a polycrystal deform independently (i.e. without considering compatibility and equilibrium conditions) and then captures grain–grain interactions by the introduction of GND arrangements to fill-in or hollow-out voids and overlaps that would otherwise be created near grain boundaries [6]. In other words, GNDs are generated to connect the deformation in individual grains within polycrystals so as to ensure the compatibility requirements.

Models at mescoscopic scale have yet to be validated, mostly due to the statistical nature of the problem which requires large numbers of dislocations to be analysed across many grains. The advent of diffraction in the TEM has enabled theories of plasticity to be developed due to the direct observation of dislocations (e.g. [7, 8]). However TEM is prohibitive for a general statistical study, simply due to time consuming sample preparation and analysis which limits the number of areas that can be studied. X-ray or neutron diffraction experiments capture the general statistical nature of the problem well (e.g. the evolution of crystallographic texture) but they tend to lack detail about the nature of grain-to-grain behaviour due to their lack of spatial resolution.

There are two developments in this field which may shed more light on the problem, such as recent developments using high resolution X-ray system at synchrotron beam lines, either through differential aperture x-ray microscopy to reveal cell structures [9, 10], far field high energy x-ray microscopy to separate cell interiors and cell boundaries [11]and near field high energy x-ray microscopy to generate large 3D grain data sets with relatively high angular resolution [12]. The spatial resolution of synchrotron X-ray beam has improved to submicron and preliminary results show dislocation cell structures can be investigated. However, a systematic study on plastic deformation in polycrystals has not been reported yet.

Dislocation density can be analysed using EBSD according to Nye's theory [13], where rotation gradients within a Burger's circuit are linked to the stored GND content. HR-EBSD measures rotation about three orthogonal axes on the surface of a sample and therefore the production of a map can be used to generate six lattice rotation curvature components. As Pantleon notes, these curvatures can be linked directly to five components of the Nye tensor and one difference [14]. From these six rotation curvature components, a physically based L1-based line energy minimisation scheme can be used to extract dislocation densities and report a description of the stored dislocation content [15].

The automated Electron Back Scattered Diffraction (EBSD) technique has developed rapidly in terms of indexing speed and accuracy during last two decades [16]. Commercial EBSD systems are generally utilised for orientation and phase discrimination through a Hough transform-based analysis of the Kikuchi band positions, and in some cases widths [17, 18].

The main limitation for the study of plastic deformation is the relatively low angular resolution provided by the 2-D Hough transform analysis route. By applying kernel averaging in data processing, it is possible to improve the angular resolution of conventional EBSD at the expense of spatial resolution [19]. Fundamentally, the lower bound sensitivity of GND determination is proportional to angular resolution and as Wilkinson and Randman note with a step size of 200nm and a realised angular resolution of $8x10^{-3}$ radians from the Hough-based analysis, the lower bound GND sensitivity is determined as ~$10^{14}$ per $m^2$ [20].

A newer analysis method with significant improvement on angular resolution was developed by Wilkinson et al [21]. They employed cross-correlation based high resolution EBSD (HR-EBSD) analysis, which allows high sensitivity to be achieved without sacrificing spatial resolution. HR-EBSD measures lattice curvature and elastic strain by determining the shifts of a number of regions of interests (ROIs) from a reference EBSP comparing with the rest of the test patterns within the same grain. The major advantage of HR-EBSD is angular resolution which is approximately 100 times better ($4.3x10^{-5}$ radians) [18] than the Hough Transform based analysis ($4.3x10^{-3}$ radians) [22] and rotations about three orthogonal axes are explicitly measured. Consequently Hough–based technique is only capable of detecting relatively large GND densities whereas HR-EBSD is feasible to characterise local low density dislocations at high resolution. (A detailed comparison of the capabilities of HR-EBSD and Hough based EBSD can be found in both the experimental work of Wilkinson and Randman [20] and the computation work of Adams et al) [23].

HR-EBSD is an off-line image processing method and it requires high quality full resolution EBSPs to be captured during EBSD scans when the aim is to extract the highest sensitivity, leading to high fidelity GND density, lattice rotation and elastic strain data [24-30]. Typically the highest bit depth patterns combined with minimum gain and contrast stretching and 1x1 camera binning on a 1K x1K pixel camera is employed. Acquiring patterns of this quality requires long (~1 second) exposure time which can result in experiments with relatively small maps being collected. For example at 1 second exposure time, 12 hours allow a collection of 43,200 data points, so that a little over 100x100μm area can be mapped with a 0.5μm step size. Prior work with HR-EBSD has been limited by the desire to capture high angular resolution information and therefore only small areas have been mapped. Britton et al presented the first polycrystalline analysis of stored dislocation content with this route and similar maps since have only contained ~10s of grains [31]. This has resulted in limited statistical analysis, as only a few grains could be studied and the statistics on the effects of neighbour grains were poor. Larger datasets would be attractive in providing better representative sampling of the inhomogeneity of deformation in polycrystalline materials.

Larger maps could be obtained if either larger step sizes were employed or a shorter exposure time was used. Altering the step size clearly has implications for the division of dislocation density into GND and SSD contributions but also affects the measurement noise on the lattice curvatures. Shorter exposure times can readily be achieved by binning the output from

the CCD. Chapter 3. presents systematic investigations of the effects on GND density measurement of the step size and binning.

OFHC polycrystal copper was selected as testing material due to the importance of understanding plastic deformation in a wide range of applications in microelectronics [32]. Copper has face centre cubic (FCC) atomic structure which has been commonly studied for dislocation plasticity such that direct comparisons with other dislocation characterization techniques is possible [33]. Finally, OFHC polycrystal copper is relatively easy to prepare for EBSD measurements.

In Chapter 3. , the optimum setting for step size and detector binning level were found to provide adequate information for cross-correlation-based-EBSD measurements of stored dislocation content. In order to investigate the general GNDs behaviours (deformation inhomogeneity) during increasing loading process, Chapter 4. presents a systematic quantitative study of GND density of five polycrystalline copper samples deformed in tension to 0%, 6%, 10%, 22.5% and 40% plastic strain. Statistical studies of GND density distribution, variation and accumulation with respect to plastic tensile deformation level and microstructure features such as grain boundaries and triple junctions were carried out.

Studying the dislocation behaviour near or at grain boundaries is of great importance in understanding many important phenomena such as recrystallization [34], creep [35], strength and fracture toughness [36, 37]. For example, it has been found [38] that special grain boundaries for instance, $\sum 3$ and $\sum 9$ grain boundaries, possess low energy and diffusivity which exhibit

considerable improvement in fracture resistance sliding, cavitation, corrosion and stress–corrosion cracking. High angle grain boundaries also manifest properties on grain boundary migration, sliding and formation of annealing twins [39].

In Chapter 5. , two critical grain boundary properties are identified; namely the grain boundary inclination angles with regard to loading axis and grain boundary disorientation angles between two neighbouring grains. The dislocation-grain boundary analysis is furthered to study if these grain boundary characters influence dislocations behaviours.

In polycrystals, where geometrical compatibility must be maintained, Taylor, Hill and Bishop assumed that the same strain occurred everywhere in polycrystals and five independent slip systems must be activated to achieve arbitrary shape change [3, 40]. Taylor factor was defined to determine the set of slip systems with respect to crystal orientation. In other words, similar to Schmid factor, Taylor factor is also an orientation dependent factor but put emphasis on shape changes rather than stress. A lower Taylor factor indicates easier plastic flow for an individual grain.

Various authors using TEM, X-ray diffraction line broadening and microhardness techniques have observed distinctive characters of dislocation structure [41, 42], stored energy [43] and mechanical properties [44] in deformed polycrystals as a function of lattice orientation. Merriman and Field have recently reported a dependence of GND density estimated from conventional Hough-based EBSD upon orientation of the crystalline [45]. In their investigation, four commercial purity aluminium (AL1050) samples

containing ~300 grains were compressed at room temperature in a channel die to 5% 10% 15% and 20% strain. The range of a measured misorientation angle was 0.5° to 5° and 2 μm step size was used to scan 570 μm x 1707 μm maps. Their results indicated that Taylor factor gave a good prediction on grain average dislocation density and that {011} grains have the highest dislocation content, although insufficient numbers of grains were sampled in this study.

The second and third aims of Chapter 5. were to investigate further the Taylor factor correlation reported by Merriman and Field with more representative maps (contain ~1500 grains versus ~300 grains). HR-EBSD maps are reported with higher angular resolution (0.003° versus 0.5°) and better spatial resolution (0.5μm versus 2 μm).

In Chapter 6. , the main emphasis is on qualitative microscopic observations of dislocation networks morphology and their development with respect to microstructure features. There are five aims for this chapter: (1) present general observed deformation microstructural features and make comparisons with the literature, primarily TEM observations; (2) qualitatively assess the effect of grain orientation on the dislocation network structure; (3) visually assess the effects of grain-grain interactions on deformation microstructures and their development with further straining; (4) assess the impact of the twin network on dislocation accumulation; (5) inspect the nature of dislocation structures near triple junctions.

# Chapter 2. Literature Review

## 2.1 Theoretical approaches

In crystalline materials the required geometrical change due to imposed plastic strain is primarily realised by the slip of numerous dislocations at specific crystallographic directions on specific crystallography planes (typically the most closely packed planes). In FCC crystals, there are 12 {111} <-110> potential slip systems, with 18 different types if edge and screw dislocations are considered separately. Dislocation slip occurs if the shear stress acting on a dislocation reaches a critical resolved shear stress (CRSS). The dislocation will move across the slip plane and possibly escape at grain boundaries or free surface leaving an unaltered lattice arrangement. After, plastic deformation slip lines can be commonly observed under optical microscope and scanning electron microscope (SEM). Not all dislocations are able to slip and escape, as some dislocations are stored when they become trapped and form dipoles and multipoles. In addition, dislocations may become trapped at other defects such as grain and phase boundaries. Further motion of dislocations results in interactions between dislocation stress field and those obstacles which increase the strength of materials. When dislocation number increases, the number of dislocation-dislocation interactions increases; therefore the strength of materials increases. This process is called work hardening or strain hardening. In this section, dislocation slip mechanics in both single crystals and polycrystals are reviewed.

### 2.1.1 Plastic deformation in single crystal Face Centred Cubic (FCC) metals

The simplest case to study slip is in single crystals as the number of microstructural variables are reduced to the minimum. Schmid et al in 1935 first proposed that slip begins when shear stress on some slip systems reaches a critical value often called the critical resolved shear stress (CRSS)[46]. The condition necessary for slip can be written as

$$\tau_c = \sigma \cos\varphi \cos\gamma \qquad \text{Equation 2-1}$$

Where $\tau_c$ is the CRSS, $\sigma$ is the external loading stress, $\varphi$ is the angle between the slip direction and loading axis and $\gamma$ is the angle between slip plane and loading axis. The geometrical term $\cos\varphi \cos\gamma$ is defined as Schmid factor $m$.

Hosford [47] thoroughly explained Schmid's theory with various analytical examples. If one conducts a uniaxial tensile test with known crystallographic orientation, the Schmid factor for all 12 slip systems can be easily calculated and the one with the highest Schmid factor will be activated first.

It should be emphasised that Schmid factor is only a geometrical factor to indicate the level of easiness for primary slip to take place and the nature of the local stress field must be considered. Therefore, the Schmid law has limited applicability to predict plasticity undergone in multidimensional deformation. Hosford [47] stated that to satisfy geometrical change, different

numbers of independent slip systems were required for various mechanical testing methods. For example, for tension tests, crystals are extended in single direction such that single slip is sufficient. However, in plane strain compression tests multiple slip (at least three independent systems) must occur to meet the geometrical requirement. Furthermore an arbitrary crystal shape change needs at least five independent slip systems (known as the von Mises condition) which occur commonly in polycrystals [48].

In order to accommodate progressively imposed plastic strain (requiring shape changes), the single crystal begins to rotate due to constraints of the sample grips so that the angle between the tensile axis and the slip direction reduces. At some point, the crystal orientation reaches a position where the CRSS is achieved on more than one slip system. This leads to multiple slip. With continuous rotation, crystals will reach to more stable orientations where higher external stress is required to activate new slip systems for further slip. Crystals' orientation evolution contributes to work hardening and is the basis for texture evolution during plastic deformation.

### 2.1.2Deformation mechanisms in polycrystals

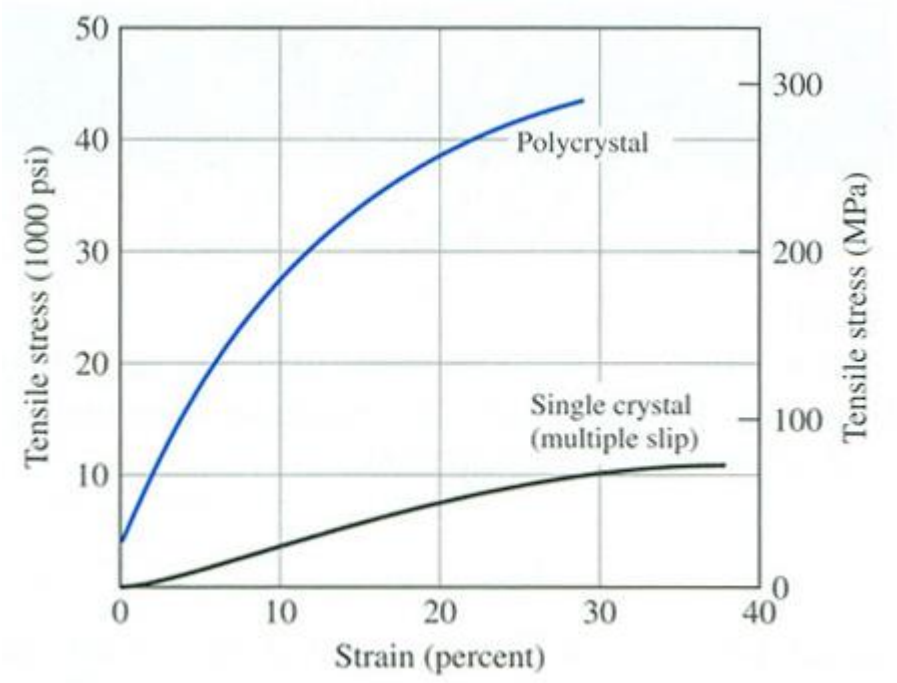



**Figure 2-1, shows the stress and strain curve for a single crystal of copper and a polycrystalline copper[49].**

Sachs [50] proposed that each grain in a polycrystal could be treated as single crystals and the deformation mechanisms of single crystal could be directly applied to individual grains. Sachs, Cox et al [51] attempted to predict the yield strength of polycrystal using Schmid theory in which the minimum geometric factor among all possible slip systems was determined for each grain and the mean value of Schmid factor of all constitute grains was calculated. The prediction had a large divergence from experimental results. Taylor [52, 53] pointed out that this approach omitted the compatibility condition and so grains where not required to deform in a way that keeps grain boundaries intact. Unlike in single crystals in which slip can occur solely in the most favourable slip system, the geometrical shape changes for grains

in polycrystal are further constrained by their encompassing neighbouring grains.

#### 2.1.2.1 Taylor's theory and Taylor factor

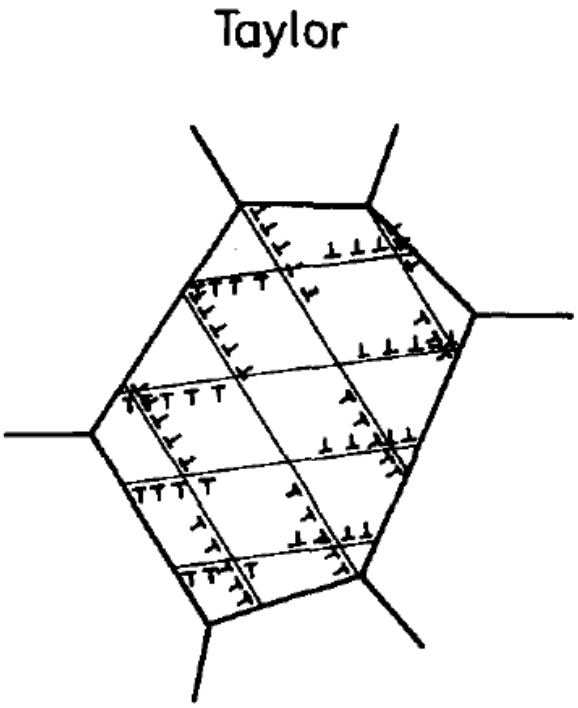



**Figure 2-2, schematic slip pattern expected from Taylor's theory in which homogenous deformation takes place at every element in the polycrystal [54].**

In contrast to Schmid's theory Taylor [53] assumed that in polycrystals arbitrary shape change was expected for all the grains such that minimum five active slip systems with the least total energy expenditure was required to maintain continuity and compatibility conditions. In order to ensure polycrystals reaching their final deformation state, Taylor assumed the all grains undergo the same shape change. The resultant work per unit volume ($dw$) contributed from the minimum five active slip systems was equal at any point within a grain (homogeneous deformation) and thus the product of

resultant stress and strain are equal everywhere (see Figure 2-2). This relationship can be expressed as Equation 2-2:

$$dw = \sum_{i}^{1} \tau \, d\gamma_i = \sigma d\varepsilon \qquad \text{Equation 2-2}$$

Where $w$ is the work done per unit volume, $\tau$ is the magnitude of the CRSS and assumed to be the same for all slip systems, $i$ indicates the number of active slip systems, $\gamma_i$ is the dislocation slip on that slip system and finally $\sigma$ and $\varepsilon$ correspond to the imposed stress and strain on the specimen along the loading direction.

As the resultant stress and strain at any point within a grain is equal to the exerted stress and strain, the underlying shear strain contributed from each activated slip system varies significantly and the combinations of five slip systems are directly depending on the orientation of that point. The Taylor factor, $M$, was proposed to describe such crystallographical effect. It is determined as the ratio of resultant strain over the sum of individual shear strain from all slip systems as shown in Equation 2-3.

$$\frac{\sigma}{\tau} = \frac{d\gamma}{d\epsilon} = M \qquad \text{Equation 2-3}$$

Small $M$ value indicates that under the same resultant strain, the total slip occurred from all slip systems is small. In other words, grains with this specific orientation are easy to deform with respect to its loading axis. By calculating the M for all orientations and averaging to find $\overline{M}$, the stress strain curve for a random polycrystal can be predicted. Experimental stress strain results obtained on polycrystal aluminium agreed reasonably well with Taylor's prediction [52]. For FCC with random grain orientation $\overline{M}$ is 3.06.

Interestingly, Taylor's theory implies that the higher strain hardening rate and higher strength observed in polycrystals is solely due to the increased number of slip systems which are originally stimulated to satisfy the geometrical compatibility condition.

#### 2.1.2.2 Hill and Bishop's theory

In Taylor's theory, determination of the most appropriate combination of five active slip systems was solely based on the calculation of minimum energy expenditure among all possible combinations. The physical feasibility of stress state associated with these selected five active slip systems is disregarded. Hill and Bishop [4, 40] proposed a different approach based on the stress state to calculate Taylor's factor in FCC polycrystals. In Hill and Bishop's analysis, to satisfy the geometrical compatibility, the same assumptions were made as Taylor that crystals were deformed homogeneously and minimum five active slip systems are needed for general shape changes. However, instead of directly identifying the least energy expenditure slip systems, they further constrained the possible combinations

by a criterion: there must be a physical stress state (combination of $\sigma_1, \sigma_2, \ldots \sigma_{23}$) on crystals to simultaneously activate five or more slip systems without excessing CRSS on any other slip systems. 28 potential stress states were found and the one with maximum virtual work (least energy) was determined to give the most reasonable Taylor factor ($M$) value.

Similar predictions were found from both geometrical (Taylor's) and stress state (Hill and Bishop's) approaches; however, the calculation based on Hill and Bishop's approach is significantly simpler.

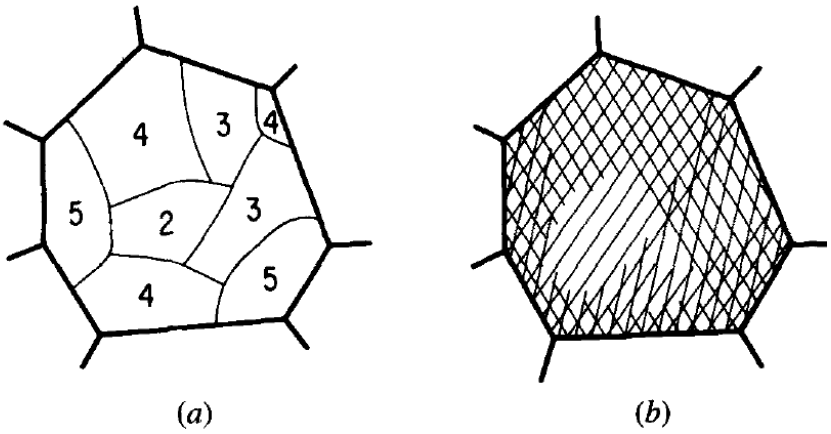



**Figure 2-3, (a) shows the necessary number of active slip systems in a single grain within a polycrystal to achieve compatibility. (b) The schematic drawing of expected surface slip bands patterns within the grain. [55]**

Two critical assumptions were made in both approaches namely the same geometrical shape change occurs everywhere in a polycrystal and the CRSS on all slip systems are the same. These two assumptions have been systematically investigated by Kocks [5, 56, 57]. It was found that in practice the homogeneous deformation assumed for all constitute grains is not the only means to maintain compatibility condition. For example, in a randomly orientated HCP polycrystals in which fewer slip systems are available than

FCC polycrystals so that mechanical twinning greatly accommodates the geometrical shape change[58]. Even in FCC polycrystals, it is unnecessary to require arbitrary shape change in every element of grains as fewer than five slip systems are often sufficient to satisfy the shape change in grain interiors (see Figure 2-3) [55]. It is the grain interfaces and corners where arbitrary shape changes are generally essential to accommodate the deformation gradient between a selected grain and its neighbouring grains due to abrupt change of orientations [59-61]. Fleischer studied the number of active slip systems presented in a deformed polycrystal brass sample by sectioning and etching and concluded that 40% of grains had fewer than five active slip systems, grain boundaries and triple junction showed high fraction of five active slip systems [62].

The second assumption on CRSS suggested that the strain hardening process should not vary drastically with various combinations of slip systems, though distinct dislocation interactions were expected in different combinations. Plane compression tests were conducted on single crystals of copper and aluminium with a wide range of orientations [63-65] undergo polyslip (more than 5 active slip systems) with various slip system combinations. It was concluded that the average work hardening in polycrystals primarily depended on the number of activated slip rather than the particular combinations.

#### 2.1.2.3 Ashby's theory (GND theory to maintain compatibility)

In spite of different deformation ability for each grain due to various orientations in polycrystals, grains prior and after plastic deformation should fit together as a whole unless fracture occurs. As discussed in the previous section, Taylor, Bishop and Hill addressed this problem by assuming uniform deformation would take place in every element in polycrystals and at least five slip systems should be activated to achieve the geometrical compatibility [4, 53]. Ashby was inspired by his experiments using dispersions of hard undeformable particles in otherwise pure single crystals and dislocation observation using TEM[66] and X-ray diffraction [67, 68]. In those experiments, both classic continuum plasticity theory [69] and dislocation mechanics [70] failed to explain the observed participates' size effect on work hardening rate. A new theory is devised that combines classic continuum theory and dislocation mechanics theory to rationalise the observed size effects by introducing GNDs previously described by Nye in 1953 [13]. This model was adapted to explain non-homogenous deformation in polycrystals [1, 71, 72] in which GNDs played an important role by providing geometrical shape change to satisfy compatibility and avoid violation of equilibrium condition. Furthermore, depending on grain size, GNDs could dominate total dislocation density overtaking statistically stored dislocations (SSDs) and actually control the stress strain curve and thus work-hardening process.

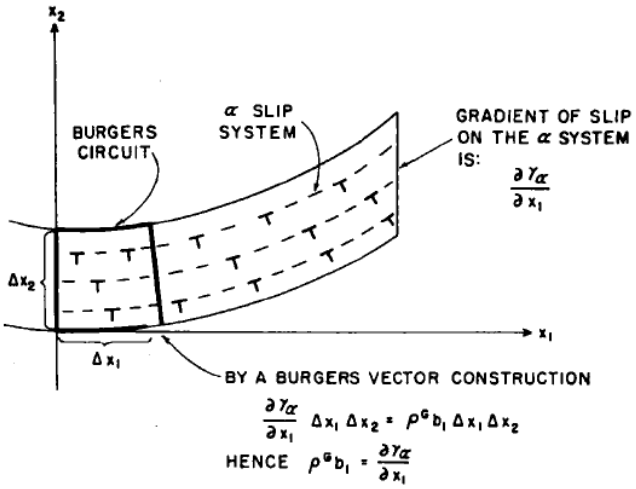



**Figure 2-4, schematically shows the geometrically necessary dislocations (GNDs) presenting in slip system $\alpha$ to accommodate deformation gradient in non-homogeneous deformation. The calculation of GND density is also presented [1].**

During an increment of plastic deformation, dislocations move through the lattice contributing to plastic strain and are then either annihilated or are trapped in the lattice as residual dislocations. These residual dislocations are very important for work-hardening and geometrical shape change and can be further divided into statistically stored dislocations and geometrically necessary dislocations. Statistically stored dislocations (SSDs) are generally accumulated by random and mutual trapping. They are left in forms of dipoles or multipoles working as obstacles on the slip planes to pin subsequence incoming dislocations. In fact, in single crystals (homogeneous deformation), they are the main factor governing work-hardening and controlling the stress strain curve. Geometrical necessary dislocations (GNDs) are generated to accommodate plastically non-homogeneous deformations in which deformation gradients are imposed by microstructure. The concept of GNDs is illustrated in Figure 2-4 in which an element of crystal undergoes non-uniform plastic deformation and the GNDs are present to accommodate the deformation gradient resulting in lattice curvature. The

GND density can be determined from the length of failure closure within a Burgers' circuit as is expressed in Equation 2-4 [1]. It is important to emphasise the fact that we cannot unambiguously assign a specific dislocation to SSD or GND but we can split the overall dislocation density into two contributions depending on the specified size of Burgers circuit. In polycrystals, a large number of GNDs is generated to accommodate the geometrical compatibility condition. The stress-strain curve is thus controlled by both SSDs and GNDs. However the density of GNDs could overtake SSDs to dominate work hardening process if severe plastic strain gradients are imposed.

$$\rho^G b_1 = \frac{\partial \gamma_\alpha}{\partial x_1} \qquad \text{Equation 2-4}$$

Where $\rho^G$ is the GND density within a Burgers circuit, $b_1$ is Burgers vector length, $\gamma_\alpha$ is the shear strain imposed onto the Burgers circuit and $x_1$ is the side length of Burgers' circuit.

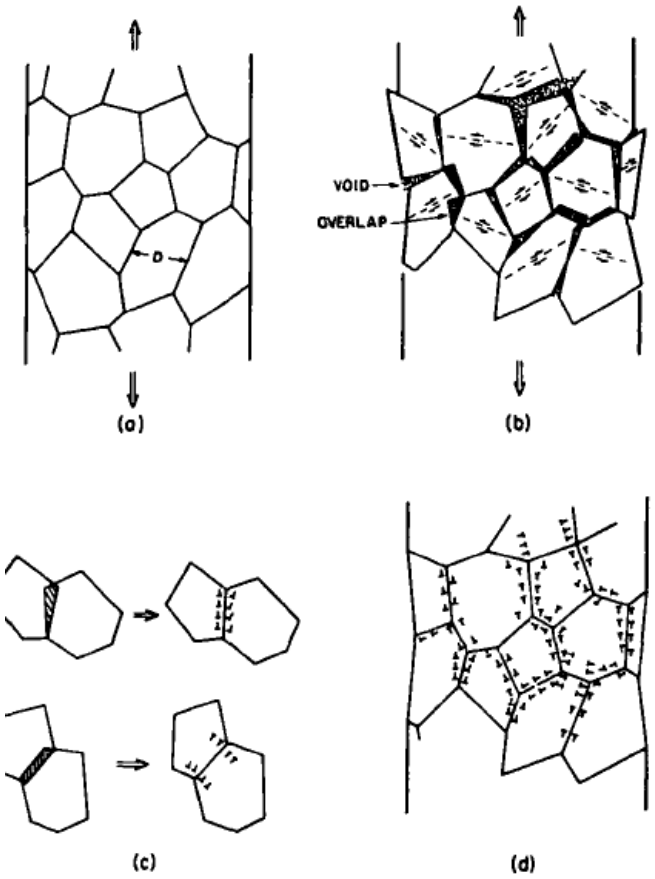



**Figure 2-5, Ashby's model of deformation of a polycrystal. (a) a polycrystal is deformed under tension, (b) voids and overlaps are created by treating constitute grains as isolated grains under tension, (c) overlaps can be corrected by inserting geometrically necessary dislocations, (d) the final GNDs configuration to satisfy compatibility condition[59].**

The TEM study in polycrystal copper deformed in tension by Essmann et al [66] found that slip occurred predominately in primary slip system in the grain interior and secondary slip and multislip appearing adjacent to grain boundaries. Furthermore X-ray diffraction results suggested high lattice rotation were found near grain boundaries [1]. Based on these observations, Ashby proposed that in polycrystalline materials constituent grains could be first treated as isolated units with no regard to their neighbouring grains for which they would undergo the same amount of deformation as the whole specimen according to Schmid's law. During this process, SSDs are formed and accumulated for work-hardening in a linear relationship as the imposed plastic strain. This single crystal assumption led to assembling failure as

voids and overlaps appear at grain boundaries (see Figure 2-5 (b)). To satisfy the compatibility condition, Ashby introduced GNDs near grain boundaries in which the overlaps were removed by adding GND arrays or prismatic interstitial loops (see Figure 2-5 (c)) and the gaps were filled by inserting prismatic vacancy loops which can be formed by reversing the directional signs of those constitutional dislocations of the interstitial loops shown in Figure 2-5 (c). It is important to note that any proposed GND configuration must satisfy the equilibrium condition by checking that the GND array generated internal stresses field did not exceed local shear stress anywhere to initiate new slip system or cross slip [1].

Since the displacement to fill or open a void or gap between grains is approximately DΥ/2 where Υ is the shear strain and D is the grains diameter, the number of GNDs added in each grain is ~DΥ/4b where b is Burgers' vector and the area of grains is ~ $D^2$. Thus, the GND density stored in a grain can be expressed as:

$$\rho^G \cong \frac{\gamma}{4bD}$$ Equation 2-5 [59]

Two main factors contribute to the work-hardening process in polycrystals; namely long range internal stresses generated from GND arrays for which its effect is limited to small strains due to the onset of cross slip; and short range internal stresses generated from the interaction between mobile dislocations and stored dislocations, which depend on dislocation types, arrangements and density. To simplify and generalise the contribution of short range stresses to work hardening, Ashby described the dislocation array solely by

one scalar parameter: its average density. When the density of GNDs exceeds SSDs, the behaviour of GNDs determines the work-hardening process. The flow stress can hence be calculated from Equation 2-6 similar to Nabarro, Basinski and Holt [73].

$$\tau = \tau_0 + CGb\sqrt{(\rho^G)} \qquad \text{Equation 2-6}$$

Where $\tau$ is the flow stress and $\tau_0$ is the other contributions to the flow stress (solution hardening), C is an empirical constant and normally has a range of ~0.3, G is the shear modulus and b is the Burgers vector length. By substituting Equation 2-5 into Equation 2-6, it was noted that the square of imposed strain was proportional to the flow stress and indicated a characteristic parabolic stress strain curve could be obtained.

Ashby coupled heterogeneous deformation (strain gradient) due to microstructure with plasticity theory and married classic continuum theory and dislocation mechanism. As materials tests has been moved to microscopic length scales [74, 75] where classic plasticity failed to explain observed size effects, the strain gradient in non-homogeneous deformation plays in an important role. Ashby's GND concepts motivated significant advances in the development of strain gradient plasticity theories [76-79]. However, the detailed GND strengthening mechanisms remain elusive and Ashby's GND model on work hardening in polycrystals has not yet been fully validated due to the limitation of experimental techniques to recover the presence and quantity of GNDs.

#### 2.1.2.4 Grain-grain interaction

Superposing on grain orientation effect, theoretical approach on bicrystals [80] revealed that neighbouring grains could have strong effects on the content GNDs in the host grains. In the theoretical approach proposed by Raabe [80], the intrinsic dependence (grain orientation) is investigated on the basis of the geometrical stability of grains with respect to small changes in starting orientation. For the intrinsic approach, the neighbouring grains' interactions are not included. It is formulated by measuring the divergence (vector calculus) to reorientation rate vector fields in orientation space. This scalar divergence function then quantifies stability of grains under homogeneous boundary conditions as a function of orientation and strain state. The grain-grain interaction effects were included later using a crystal plasticity finite element approach.

In their model, orientations (Brass and S) with positive divergence are acting as sources in reorientation rate vector field and determined as kinetically unstable such that high tendency for GNDs needs to be generated. Orientations (e.g. Goss and cube) with zero divergence characterize reorientation rate identity with surrounding orientations hence no tendency for grains to give rise to GNDs. Orientations with negative divergence (e.g. Copper) act as sinks in the reorientation rate vector field and thus kinetically stable and not prone to build up of GND density. This theory was verified using a crystal plasticity finite element method [80].

Their results suggested that centre grains with positive or close to zero divergence had a significant dependence of their tendency to form GND

networks on neighbouring grains. These modelling results had a good agreement with experimental results on bi-crystals. It is of great interest to examine the viability of this model in polycrystals. The summary of this theoretical approach is shown in Table 2-1. Some special grains with orientations such as Goss [001], Copper [111], Brass and $RZ_{fcc}$.

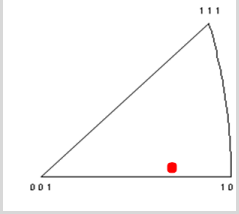
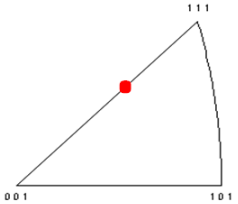
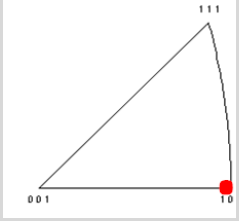
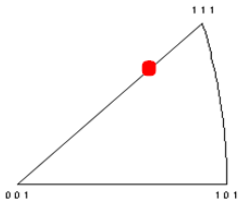
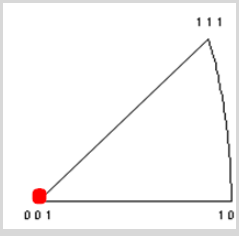
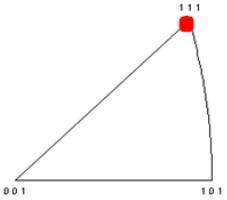
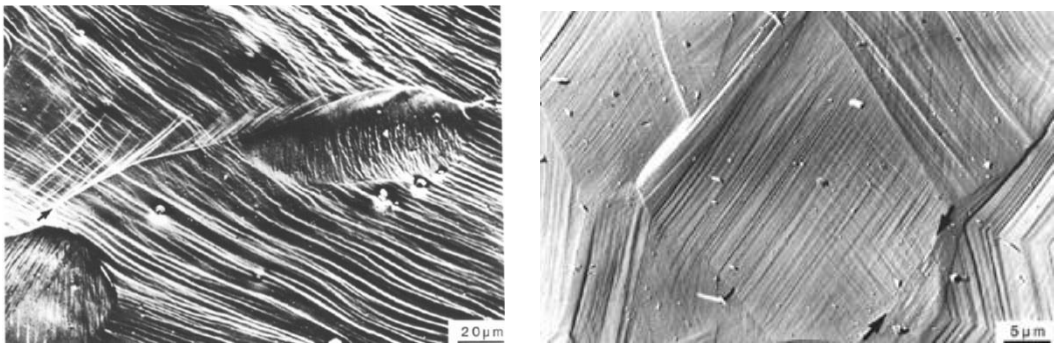
| Orientation | Euler angles [$\varphi_1$ $\Phi$ $\varphi_2$] | IPF | Divergence | GND density | Neighbouring grain effect |
|---|---|---|---|---|---|
| **$RZ_{fcc}$** | [32° 85° 85°] |  | Maximum | The Highest GND density | Strongly affected by neighbour grains |
| **Brass** | [35° 45° 0°] |  | Pronounced positive | High GND density | Not affected by neighbour grains |
| **45° rotated cube** | [45° 0° 0°] |  | Pronounced positive | High GND density | Strongly affected by neighbour grains |
| **S** | [60° 32° 65°] |  | Close to zero | High GND density but no GND boundaries formed. | Strongly affected by neighbour grains |
| **Goss** | [0° 45° 0°] |  | Close to zero | Low GND density | Strongly affected by neighbour grains |
| **Copper** | [90° 35° 45°] |  | Negative | Low GND density | Not affected by neighbour grains |

**Table 2-2, shows the transformation of Euler space to IPF aligned along RD and a summary of Raabe's theoretical approach [80] : the orientation and neighbouring grain dependence on GNDs development. The red dot in IPF indicates the position of individual specific orientation.**

## 2.2 Experimental observations

In the preceding section several critical strain accommodating and hardening theories have been presented. These dislocation based theories must be supported by experimental observations. In this section the author reviews the characteristic deformation structure observed using various techniques and their associated possible dislocation models.

### 2.2.1 Slip line observations




(a) (b)

**Figure 2-6, (a) 99.9% iron polycrystal with 0.26 mm average grain size strained to 0.15 in uniaxial tension. The micrograph was taken using light microscopy and the black arrow indicates grain boundaries[81]. (b) Surface replica of 70:30 brass polycrystal with averaged grain size of 0.02mm was strained 0.15 by cold rolling[82].**

Slip lines (as shown in Figure 2-6) were the first microscopic information observed on plastically deformed samples [2]. The earlier observations and investigations prior to the invention of scanning electron microscopy (SEM) were made by employing light microscopes and a technique to shadow surface replicas for TEM [82, 83]. They provided valuable information concerning the path of dislocations that intersect the free surface which could be further linked to the number of activated slip systems and the orientations of slip lines, the space between slip lines and the complicated line sets in the vicinity of grain boundaries (see Figure 2-6). Grains with various orientations showed clear preferential primary slip systems. The slip lines tended to be

more uniform toward the interior of grains and inhomogeneous deformation was commonly found near grain boundaries.

Grain boundaries, where different slip systems intersect, have been identified as the most important factor influencing the strength of polycrystals. Thus extensive systematic studies on crystal boundaries were conducted to investigate the significant role of grain boundary in dislocation mechanisms [84-86]. Many characteristic features were observed, for example at certain grain boundaries, slip was able to penetrate through to neighbouring grains whereas at some grain boundaries, dislocations piling up next to them or being absorbed by them[83]. It was believed grain boundaries acted as dislocation obstacles[81], sinks [87] and sources [88]. A number of interaction mechanisms between gliding dislocations and grain boundaries were extensively discussed by Hirth [89].

### 2.2.2 TEM observations

Transmission Electron Microscopes (TEM) offer high spatial resolution and dislocation contrast imaging and have been widely employed for the observation of dislocations and other defects such as grain boundaries, stacking faults, twinning[90]. In TEMs, a high energy electron beam is incident on an ultra-thin (typically 0.1μm-4μm thickness) specimen foil where electrons interact with specimen and pass through. An Image is formed and captured on a fluorescent screen by collecting transmitted electrons. Lattice distortions (dislocations) lead to strong contrast comparing to the regular lattice arrangements and thus can be revealed.

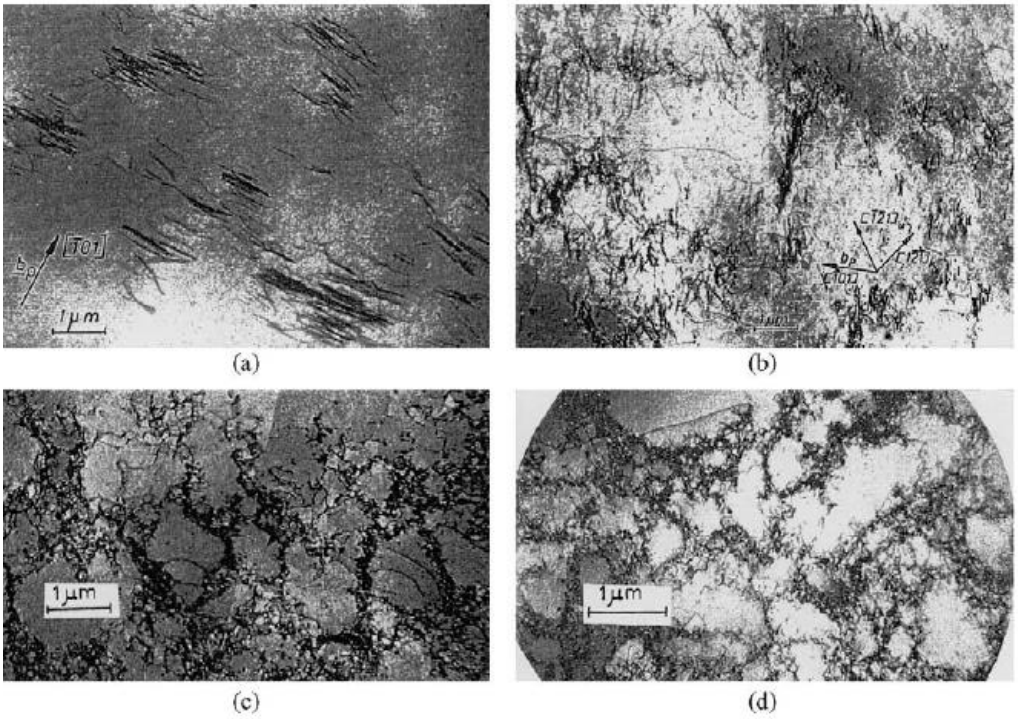



**Figure 2-7, Typical TEM micrograph dislocation observations. These TEM images were captured on deformed pure copper <100> single crystal with various imposed stress (a) 1.1 MPa; (b) 14 MPa; (c) 28 MPa; (d) 69MPa; [66]**

Figure 2-7[66] shows typical TEM micrographs at different stages of plastic deformation. In Figure 2-7 (a) a relatively small amount of stress is imposed which activated the primary slip system on specimen and a few essentially straight dislocation lines are revealed. As the stress increased in Figure 2-7 (b), the space between dislocations becomes smaller and thus the dislocation density increases. In addition the orientations of dislocation are changed from uniaxial to rather random ones, which suggest multislip systems have been activated with dislocations gliding on several independent slip systems. With larger stress imposed on specimen, tangled dislocations lines are formed in Figure 2-7 (c), (d) separated by regions of lower dislocations density. These tangled dislocations lines and less dense regions are typical features appearing in highly deformed crystals and are termed as 'dislocation cell wall' and 'dislocation cells' respectively [66]. As shown in Figure 2-7 (c),

(d), these cell patterns do further evolve with increasing plastic deformation in terms of cell geometrical shape changes e.g. cell size and wall thickness.

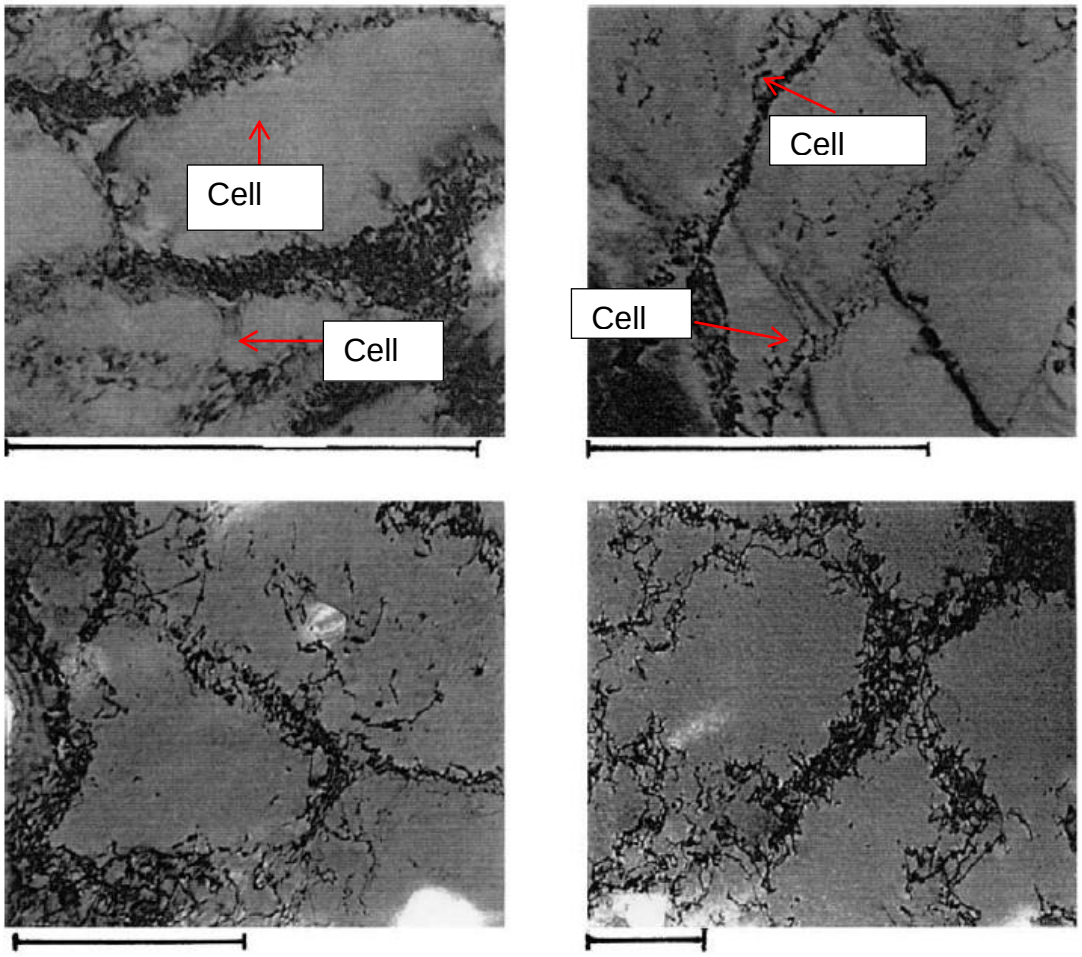



**Figure 2-8, TEM observations made on polycrystal copper deformed at the same strain rate at 200, 300, 400, 500 °C. Images are magnified with scale bar of 1 μm. Quantitatively measurement on the average dislocation space has been made [2, 91].**

Similar features are shown in deformed polycrystals. Kocks and et al carried out the TEM characterisation on polycrystal copper under the same strain rate at various temperatures (see Figure 2-8) [2]. The dislocation cell and dislocation spacing (dislocation density) are maintained at similar size although distinct detailed dislocation characters appear in each image. Staker and Holt [33] found a fixed relationship between dislocation cell size and density. Staker and Holt conducted a systematic TEM investigation on

this relationship and found that if $l$ is the mean spacing in slip plane (corresponding to square root of dislocation density) and $\lambda$ is the square root of mean cell size, their results suggested:

$$\lambda = 16l \qquad \text{Equation 2-7}$$

In highly deformed crystals, dislocation spacing measurement in TEM is rather less accurate as dislocations were tangled together. However, at highly strained level, the dislocation cells were arranged with clear structure thus based on Equation 2-7 by measuring the cell size, the dislocation slip spacing (i.e. mean free path) can be deduced.

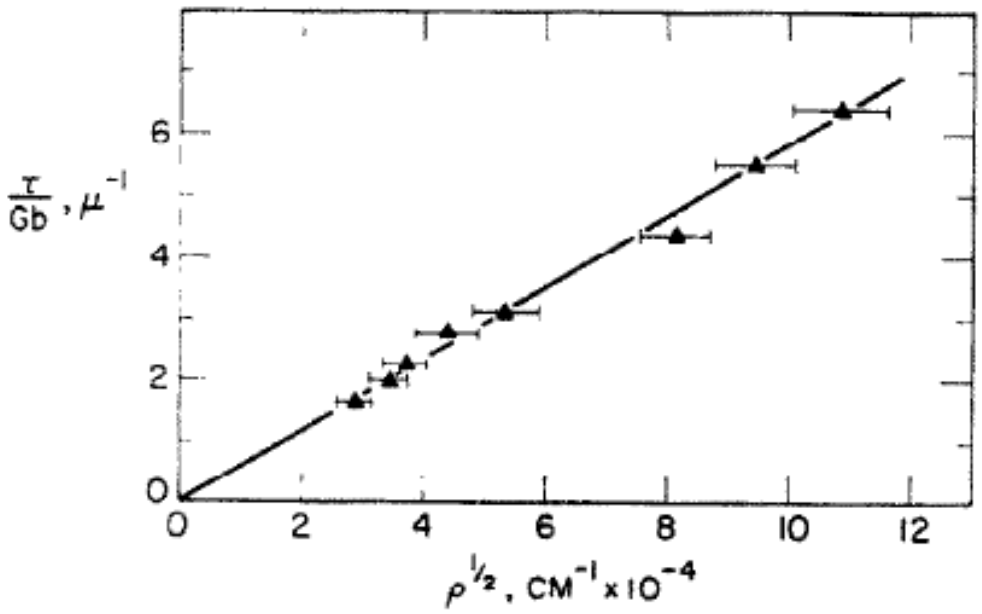



**Figure 2-9, shows the relation between the normalised flow stress and the square root of the dislocation density in uniaxial tensile deformed polycrystalline OFHC copper measured by TEM at room temperature[33]. The slop of the line from a least square fit is 0.57.**

Furthermore, the dislocation cell size and mean spacing between two dislocations evolved with further plastic deformation. One of the important

observations in the dislocation plasticity was the relationship between dislocation density $\rho$ and flow stress $\tau$ [3] as shown in Figure 2-9:

$$\tau = \alpha G b \sqrt{\rho} \qquad \text{Equation 2-8}$$

Where $\alpha$ is an empirical constant with a range of ~0.5 to 1 for copper at room temperature, $G$ is the shear modulus and $b$ is Burgers vector length.

This relationship implied that the in pure metal plastic flow stress was able to be determined directly from dislocation density without considering complicated dislocation mechanisms.

Although TEM is the most widely used technique in dislocation mechanism investigations, there are several limiting factors that need to be noted. In order to attain the thickness of electron transparency, TEM specimens must be polished in a very delicate way to between 0.1μm and 4μm thickness. This ultra-thin specimen limits TEM applicability as the preparation process is very time-consuming; also during sample preparation dislocations migrate toward free surface and thus their structure and density may be altered significantly from bulk materials due to image forces [90]. Furthermore, qualitative rather than quantitative TEM observations are often made which prohibits statistical dislocation studies in polycrystals where a large number of microstructure variables have to be considered [92].

### 2.2.3 Grain orientation dependence

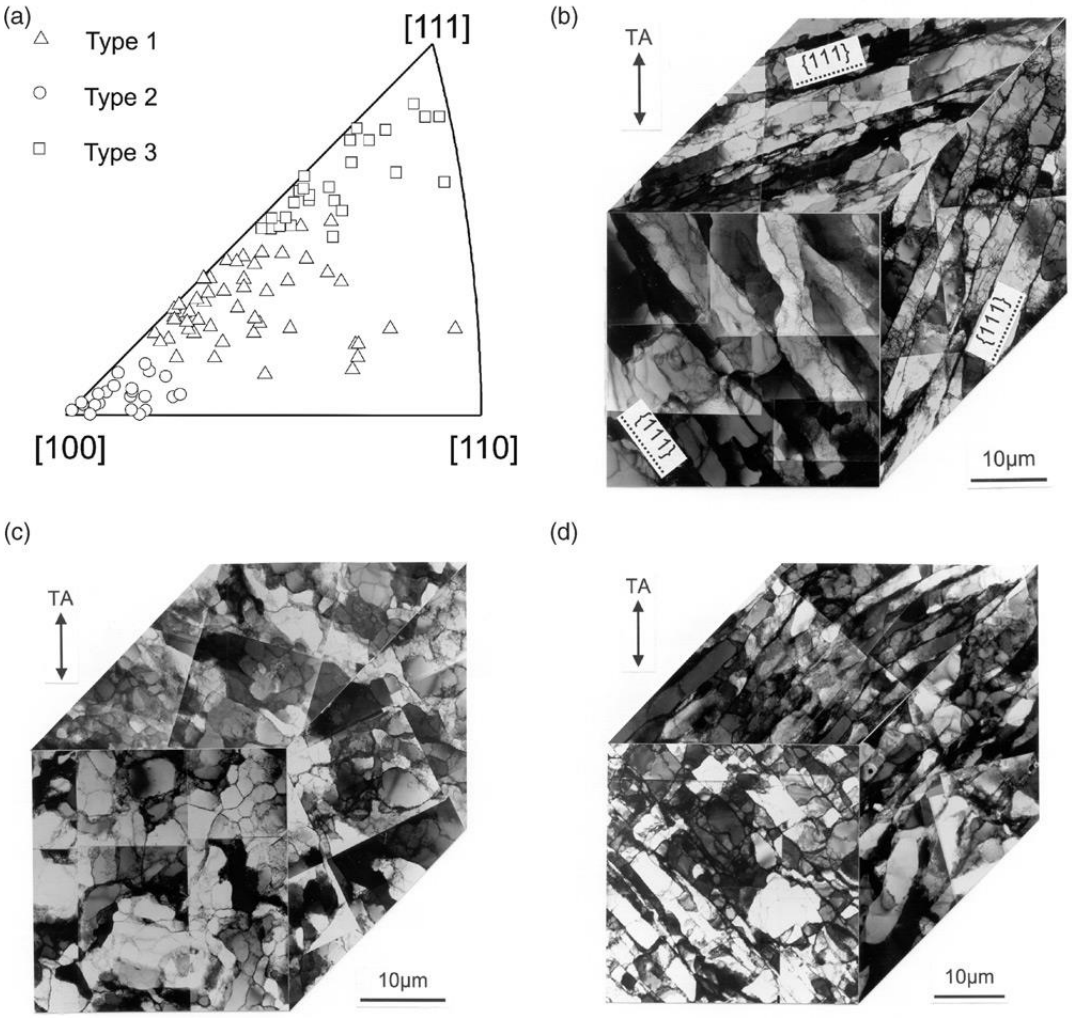



**Figure 2-10, three different types of dislocation structures developed in various grain orientations in a tensile strained (34%) pure Al sample. (a) the IPF show tensile axis (TA) orientations of 100 examined grains. Three type of distinct dislocation structures are indicated as triangle (b), circle (c) and square. (d), (b), (c) and (d) show characteristic dislocation structures for each type. [93]**

As shown in Figure 2-10, a systematic and quantitative TEM study [93] revealed that three distinct deformation microstructures arise. The first type is cell-block structure with cell-block boundaries aligned well with the slip planes. These cell block boundaries are approximately straight and parallel (Figure 2-10 (b)). This type of arrangement is normally found in the middle of Inverse Pole Figure (IPF) triangle where loading direction is aligned with RD. The second type of structure is the occurrence of subdivision in which each

domain is almost equiaxed in shape and contains a group of cells with similar orientation. Large misorientation appears near domain boundaries. This structure occurs within grains with [100] orientation (see Figure 2-10 (c)). The third type is similar to the first one but rather long range dislocation boundaries are formed (shear bands) which penetrate cross a number of grains irrespective of crystallographic slip planes. This type of structure is often found within grains whose orientations are somewhere near [111] corner in the IPF triangle (see Figure 2-10 (d)).

### 2.2.4 X-ray diffraction Topography

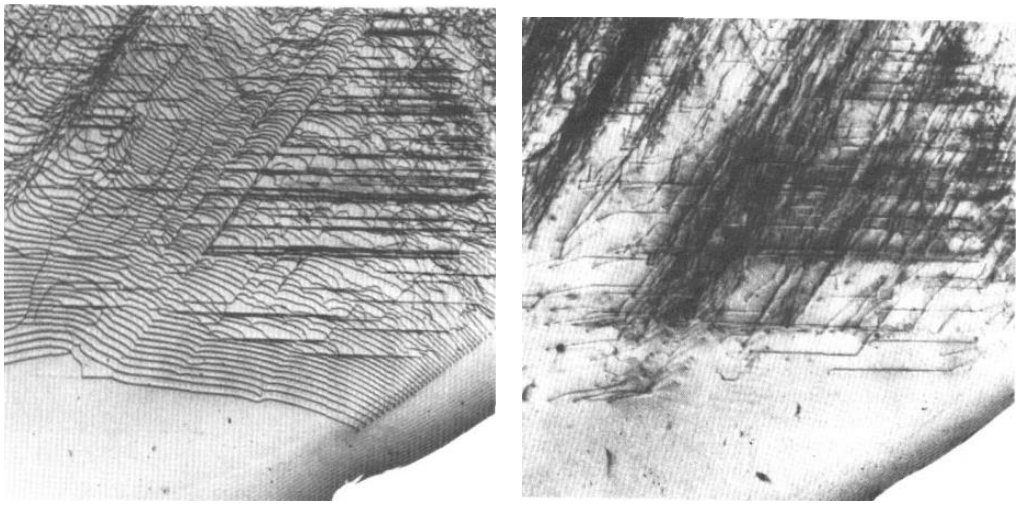


**Figure 2-11, X-ray diffraction topography of (11-1) slice of silicon 1mm thick and direction [-110] is horizontal. The image field width is 6.25 mm [94].**

X-ray diffraction technique is the second primary dislocation observation tool. Similar to electron diffraction, X-ray diffraction tomography is also able to observe dislocations (see Figure 2-11). It has the advantage of deeper sample surface penetration compared to electrons such that dislocation structure in bulk samples can be revealed. However, the spatial resolution is greatly reduced in classic x-ray diffraction which makes it is more suitable for single crystals' analysis and lower dislocation densities that generally are

found in deformed metals[95-97]. However, X-ray diffraction is undergoing a series of significant developments driven by availability of high brightness and high coherence synchrotron facilities. Larson et al [9] studied materials' deformation structure on mesoscopic length scale with sub-micrometre spatial resolution by using polychromatic synchrotron X-ray. Three-dimensional measurement of grain orientations, elastic strain tensors were made possible on polycrystal aluminium. Jakobsen et al [10] applied this developed X-ray diffraction technique to study in situ dynamic dislocation arrangements (dislocation cells) during progressive plastic deformation in pure copper. With the attained high angular resolution (~0.004°) Pantleon et al [11] extended this technique to direct dislocation structure observation in 3D in which encouraging results were reported such as dislocation cell structures and elastic strain within dislocation cells and grains at various stages of deformation in polycrystal copper. However, systematic investigations on strain hardening using this technique in polycrystals have not been reported. The possible reasons are the limited accessibility to synchrotron facilities and difficult analysis to separate data.

In addition to TEM and X-ray diffraction, there are other techniques also contributing to the characterization of the stored dislocations, such as etch pit and electron channelling microscopy. However, they are less widely used in dislocations studies [90] due to resolve overlapping etch pits with a high dislocation density and sample surface preparation for electron channelling microscopy.

### 2.2.5 EBSD and HR-EBSD plastic deformation study

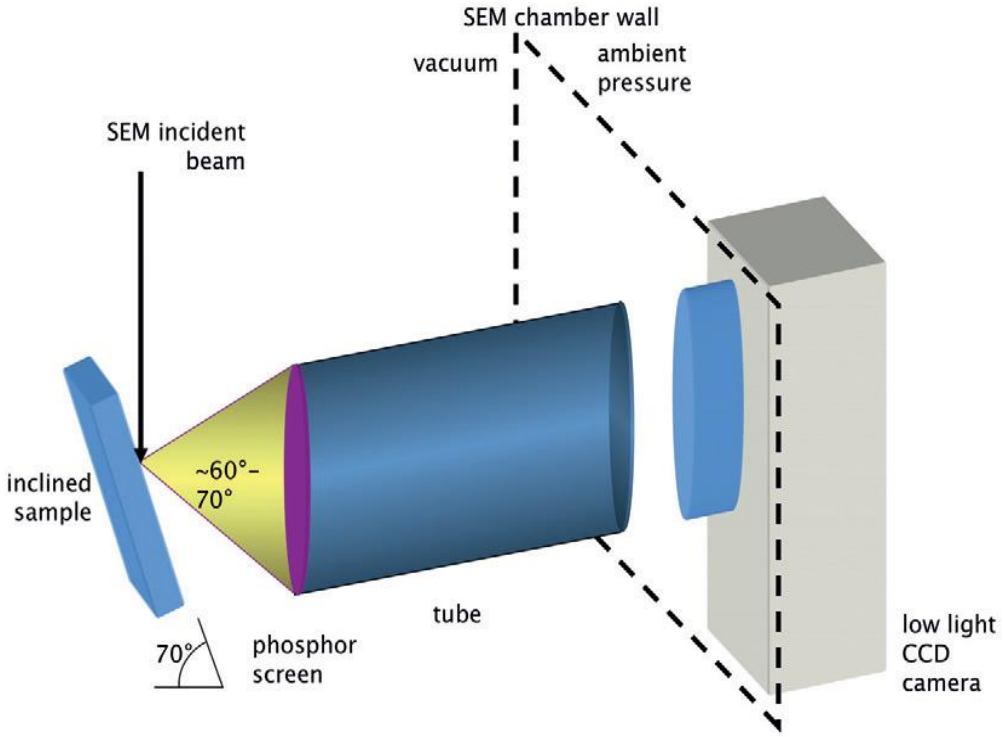



**Figure 2-12, schematic diagram to show the experimental set up of an EBSD system in a SEM chamber [98].**

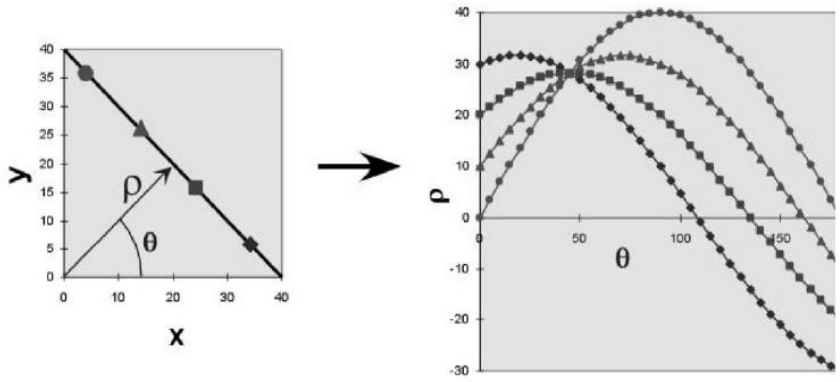
Both TEM and X-ray diffraction studies have not focussed on the role of grain-grain interaction in polycrystals presumably because of the morphology and orientations of the neighbouring grains which are either not available or not measured or reported. There has been a rapid development of the automatic Electron Backscatter Diffraction (EBSD) technique in the past few decades, which tends to successfully bridge the high special resolution possessed by TEM and high angular resolution attained by X-ray diffraction. With ~20nm attainable spatial resolution(depending on material) [99], ~0.005° [21] attainable angular resolution, relatively easy sample preparation and easy system operation, the EBSD technique is a very suitable method to revisit the longstanding and daunting challenge: strain hardening process in polycrystals.

These advantages enable the evolution of stored dislocation arrangements (structure) to be mapped at high resolution on the mesoscopic scale where the influence of overall microstructure on dislocation distribution can be clearly identified.

Fundamental theories and the history of EBSD have been comprehensively reviewed and highlighted by several authors [98,100-102]. The next section briefly presents how EBSD works and focuses on its development and application on plastic deformation characterisation.

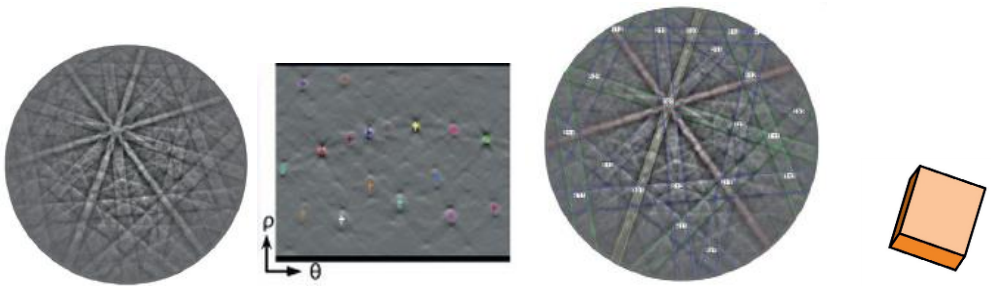
The main usage of commercially available EBSD is to automatically determine samples of crystallography within a conventional SEM. The schematic experimental set up is shown in Figure 2-12 in which a focused electron beam is emitted from SEM and incident on a 60°-70° pre-tilted surface of a bulk sample so as to maximise the back scatted electron signals. Electrons penetrate into the sample surface with interactive volume size of ~20nmx80nmx20nm to ~30nmx400nm x100nm, depending on the electron filament gun types (field emission gun or tungsten filament) [101], SEM settings and the nature of materials. Within the sample, electrons undergo elastic and inelastical interactions. At a high acceleration voltage, the inelastic scattered electrons travel in all directions and can be subsequently diffracted if they travel at the Bragg angle ($\Theta_B$) to a set of planes. Two sets of electrons will be able to do this at $\Theta_B$ and $-\Theta_B$. In three dimensional space, two cones, so called Kossel cones, will be formed and will be projected as two lines (a Kikuchi band) on a ~30mm to 40mm diameter scintillator. The

crystal is tilted so that more than one set of planes are diffracting. These Kikuchi bands formed from each plane intersect with others to form a Kikuchi pattern (EBSD pattern). Photons on the scintillator will be emitted and subsequently collected by a light sensitive charge coupled device (CCD) camera. An EBSD pattern (EBSP) image will be formed on the CCD comprising a large number of nearly straight bands termed Kikuchi bands (see Figure 2-14(a)).




(a) (b)

**Figure 2-13, illustrates how a line in spatial domain from the figure (a) is transformed into a point in the Hough domain (b).**




(a) (b) (c) (d)

**Figure 2-14 (a) captured EBSD pattern of copper with background correction, (b) Hough transform from spatial domain to Hough domain (lines are converted into peaks), (c) the pattern is indexed by looking up the reference crystallographic table, (d) schematic drawing of crystal's orientation [98].**

In order to detect the locations of Kikuchi bands more efficiently and accurately, the EBSP is transformed from spatial domain to Hough domain by Hough transform and hence detecting the location of the edges of band are converted into locating Hough peaks. In this method, an EBSD image is transformed into Hough space; sharp lines in the image space are represented as single points in the Hough space which can be expressed in Equation 2-9:

$$\rho = x\cos\theta + y\sin\theta \qquad \text{Equation 2-9}$$

Equation 2-9 can be rearranged as:

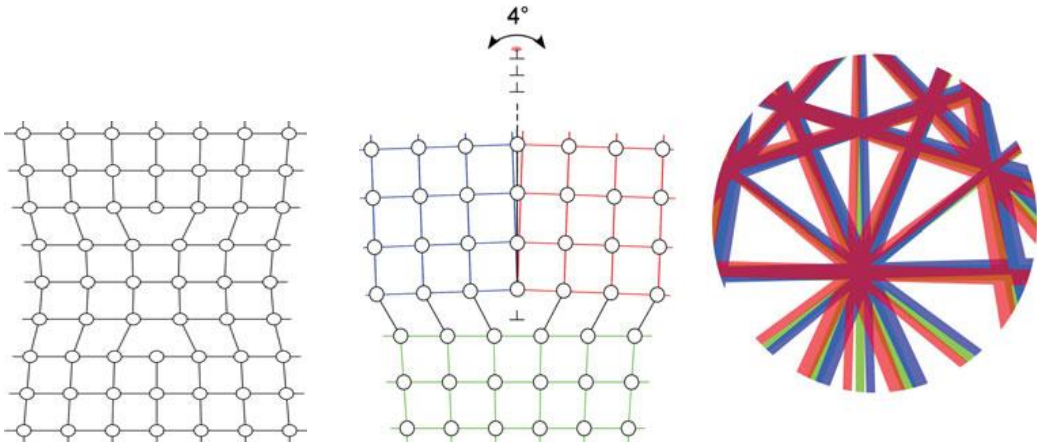
$$y = -\frac{1}{\tan\theta}x + \frac{\rho}{\sin\theta} \qquad \text{Equation 2-10}$$

Where (*x, y*) denote the pixel coordinate in the EBSD image as shown in Figure 2-13 (a) and the $\rho, \theta$ defines the axes of the Hough transform in which a given ($\rho, \theta$) corresponds to a line in the original image spaces as shown in Figure 2-13 (b). Diffraction lines in an EBSD pattern are now transformed into Hough peaks, which can be relatively easy to be detected. By comparing the measure Hough peak locations with an experimental database (see Figure 2-14 (c), (d)), the orientation can hence be determined. With precise control of the focused electron beam in a SEM, a grid of EBSD measurement with user specified map size can be obtained by shifting beam across x and y direction[98]. The pattern capture and indexing can be performed with a very high speed (100s of pattern per second) so detailed large EBSD maps

containing rich information about microstructure can be obtained within a relatively short period.

The nature of EBSP reflects the sample's lattice structure so it contains very rich information such as lattice type, lattice arrangement, lattice distortion. The crystallographic information observed from conventional EBSD systems is "geometrical", representing phase or orientation. Information such as lattice distortion e.g. stored deformation (both plastic and elastic) is more difficult to quantify in EBSPs. However, significant advances in extracting dislocation density and elastic lattice distortion have been made by various research teams around the world. Wright et al reviewed the recent development of strain analysis using EBSD, largely focussing on stored plastic strain [103]. The next section will summarise and highlight the progress that has been made on dislocation content measurement using EBSD technique.

It is important to emphasise that similar to other diffraction methods, EBSD does not directly measure plastic strain but instead lattice curvatures as a result of stored dislocation density in the material due to the deformation. From the measured dislocation density, plastic strain level might be estimated indirectly using Ashby's one parameter work hardening theory (Equation 2-6) or through an empirical approach using a series of calibration samples.




(a) (b) (c)

**Figure 2-15, schematic diagrams showing (a) the presence of an edge dislocation dipole in lattice; (b) the presence of lattice curvature caused by GND array in lattice; (c) the effect of GND on EBSPs.[103]**

In the previous section, Ashby classified the stored dislocations as two groups, namely SSDs with net Burgers' vector of zero and GNDs with nonzero Burgers' vector. Both the presence of GNDs and SSDs cause pattern blurring in EBSPs. In theory, we should be able to quantitatively analyse all stored dislocations by measuring the degradation level of EBSD pattern which is indicated by image quality maps. Various approaches have been proposed [104-110] to assess EBSD pattern quality; for example Wilkinson and Dingley in 1991 attempted to quantify plastic deformation by studying the variation of EBSPs' frequency distribution using Fast Fourier Transform (FFT). Unfortunately, none of these methods has been adopted widely within the EBSD community because EBSD image quality does not solely depend on dislocation content and also it is difficult to calibrate. There are various critical factors deteriorating image quality including the camera setting, beam interactive volume size, stability of electron beam and surface contamination. Sometimes these factors rather than the genuine stored dislocations play a

dominate role in image quality [103]. Practically EBSD is not yet suitable for quantitative measurement of all stored dislocations.

In addition to pattern degradation, stored GNDs also result in rotation gradient with in the crystals (lattice curvature) (see Figure 2-15(b), (c)). The changes of orientation across a grain can be readily and reliably measured using EBSD and is developing into a mature method for determining GND density. Several parameters of point-point orientation difference (misorientation) within a grain based on Hough peak detection in commercially available EBSD systems have been defined by different authors [111-118] and applied to quantitative analysis on a variety of plastic deformation problems. For instance Kamaya et al. applied it to stress corrosion cracking problem in stainless steel from nuclear power plants [117]. Direct EBSD observations of high misorientation were found on highly deformed samples and near crack regions [118]. General trends/characters such as high misorientation near grain boundaries and triple junctions were also commonly reported [117]. Furthermore some statistical studies were conducted to find the correlation between high misorientation regions and the associated microstructure [119]. However, the most fundamental mechanisms resulting in such phenomena still remain elusive because of lacking systematic statistical study.

One of the most significant advances in plastic deformation study using EBSD is the adoption of Nye's dislocation tensor [13] theory which enables the marriage between the measured lattice rotation gradient or misorientation and the estimated lower bound GND content [120]. The mathematical basis of this framework has been modified and optimised by several authors to allow the yielding of reasonable GND density estimations based on EBSD

measurement [14, 121-124]. This enables linking the observed scalar variable, lattice curvature (misorientation) with dislocation tensor which links to physical models. It leads to more advanced and detailed study on investigating the behaviour of GNDs in various plastic deformation modes in both single crystals and polycrystals [14, 22, 122, 123]. The detailed mathematical framework is reviewed in the methodology section (section 2.4).

The most established method for analysis of EBSD patterns is to measure orientation by determining band position through the position of peaks in the Hough transform [122]. Commercial EBSD systems have been available for two decades and Hough based analysis predominated EBSD studies on plastic deformation [108, 116, 122, 123, 125-127] as it could be directly obtained from commercially available EBSD systems. However, the attained angular resolution is relatively low (1°~0.5°) [128] which constrains its applications to samples at highly deformed states for which large lattice rotation are present. The poor angular resolution further limit accurate determination of the axes of misorientation between dislocation cells with relatively low misorientation [129]. Although some filters have been designed to nominally increase the angular resolution to <0.5° [130] by running a smoothing square array filter across EBSD maps, the nature of these filters lacks fundamental physical basis. Care must be taken in using these filters as artefacts can be generated that may easily be mistaken as real features [127].

With the aim to accurately recover the elastic strain and rotation stored in materials by examining the movements of features in EBSPs, Wilkinson et al have developed various related methods [104, 131, 132] including extending

the sample-detector distance to increase the angular resolution. Ultimately, in 2006 the highest angular resolution (~0.005°) was realised using image cross-correlation. A detailed description of this HR-EBSD analysis will be provided in the methodology section (section 2.3).

The HR-EBSD methodology was further polished by Britton and Wilkinson using robust iterative fitting analysis for recovering a larger proportion of the map where significant lattice rotation stored [133] and subsequently applying a remapping method to reduce the effect of artificial elastic strain induced by the presence of large rotation[134]. The HR-EBSD technique was applied extensively on relatively localised microstructure features such as GND distribution around Nano-indents [15, 135], selected grain boundaries [31, 136], carbides in single crystal[137] and crack tip [138]. Furthermore Littlewood and Britton et al studied the distribution of HR-EBSD obtained GND density in polycrystal titanium deformed by tensile [31, 139] and cyclic loading [140, 141] conditions. However the probing region containing approximately 10-40 grains was relatively small for statistically reliable analysis.

The aim of this project is to further extend HR-EBSD technique to address the long standing fundamental problem: work hardening process in polycrystal materials. The three main constituent components in this thesis are: quantitative study of GND evolution and accumulation in progressively deformed polycrystal copper with highest attained resolution, the GND density measurement sensitivity study: effect CCD camera binning and step size, statistical analysis of GND evolution and accumulation on representative maps with respecting to various microstructure variables.

## 2.3 High resolution EBSD

EBSD patterns consisting of backscattered electrons from a highly (~70°) tilted sample surface were formed on a circular phosphor screen and subsequently recorded by a peltier-cooled CCD camera with 1300 x 1030 pixels with intensities digitised to 12 bits, cropped to isolate the circular phosphor region. The background defects and noise are captured prior to an EBSD scan and subtracted from each recorded images. No artificial gain and black value are applied in the image acquisition process. However the camera binning level is adjusted appropriately to balance the measurement sensitivity and scanning region size within a time span constrained normally by instrument stability. Furthermore, two EBSD scan grid layouts are available namely the square grid mode and the hexagonal grid mode. Due to the geometrical simplicity, only the square scan grid layout is used by HR-EBSD.

Elastic strain and rigid body rotation within the sample body lead to lattice distortion and hence shifts in the position of EBSD pattern's zone axis (and other features). In cross-correlation based analysis, a reference pattern high quality within the central area of each grain is selected. By measuring the relative shifts between the reference pattern and the test patterns within a grain, the displacement gradient tensor which describes the difference in deformation state of specific probing point and the reference can be back calculated based on the movement of the measured features. The derivation process can be illustrated as following [142]:

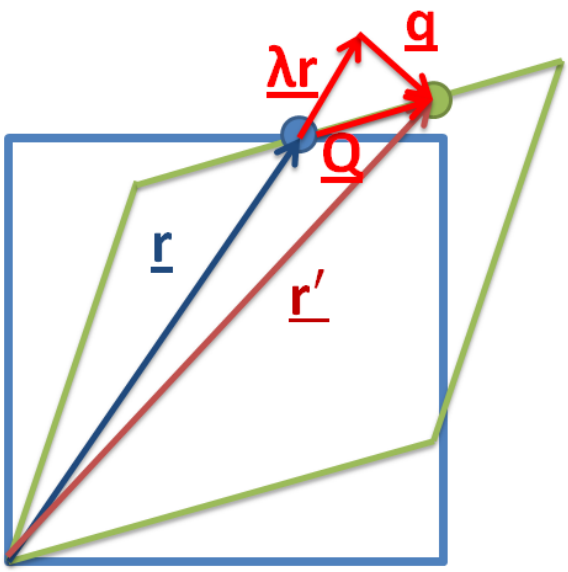



**Figure 2-16, schematically shows the deformed(green square) and undeformed 2D lattice structure(blue square) due to elastic strain and body rotation and resulting shifts on EBSD.**

As shown in Figure 2-16, considering a reference lattice (blue square) is deformed (red square) arbitrarily due to elastic strain and lattice rotation. The initial vector *r* is distorted to *r*' with a displacement vector ***Q*** which is manifest as projected zone axes shift in the EBSD pattern: ***q***. Therefore the vector relationship between **q**, **Q** and $\lambda\mathbf{r}$ can be expressed as:

$$\boldsymbol{q} = \boldsymbol{Q} - \lambda\mathbf{r}$$

**Equation 2-11**

Where $\lambda$ is unknown scalar.

As the **Q** can be also determined by:

$$\boldsymbol{Q} = \boldsymbol{r}' - \boldsymbol{r}$$

**Equation 2-12**

And **r**' can be transformed from **r** by displacement gradient tensor **A**, thus

$$\boldsymbol{r'} = \boldsymbol{Ar} \qquad \text{Equation 2-13}$$

Where A is defined by displacement **u**= ($u_1$, $u_2$, $u_3$) at position **x** = ($x_1$, $x_2$, $x_3$) and **I** is the identity matrix.

$$\boldsymbol{A - I} = \begin{pmatrix} \frac{\partial u_1}{\partial x_1} & \frac{\partial u_1}{\partial x_2} & \frac{\partial u_1}{\partial x_3} \\ \frac{\partial u_2}{\partial x_1} & \frac{\partial u_2}{\partial x_2} & \frac{\partial u_2}{\partial x_3} \\ \frac{\partial u_3}{\partial x_1} & \frac{\partial u_3}{\partial x_2} & \frac{\partial u_3}{\partial x_3} \end{pmatrix} \qquad \text{Equation 2-14}$$

Substituting Equation 2-12 and Equation 2-13 into Equation 2-11, it becomes

$$\boldsymbol{q} = \{\boldsymbol{A} - (\lambda + 1)\boldsymbol{I}\}\,\boldsymbol{r} \qquad \text{Equation 2-15}$$

In Equation 2-15, $\lambda$ is an unknown scalar which cannot be obtained from shifts measurement. However it can be eliminated by substituting one of three simultaneous equation from any of the other two to yield the following two simultaneous equations:

$$r_2 r_3 \left[\frac{\partial u_2}{\partial x_2} - \frac{\partial u_3}{\partial x_3}\right] + r_1 r_3 \frac{\partial u_2}{\partial x_1} + r_3^2 \frac{\partial u_2}{\partial x_3} - r_1 r_2 \frac{\partial u_3}{\partial x_1} - r_2^2 \frac{\partial u_3}{\partial x_2} = r_3 q_2 - r_2 q_3 \qquad \text{Equation 2-16}$$

$$r_1 r_3 \left[\frac{\partial u_1}{\partial x_1} - \frac{\partial u_3}{\partial x_3}\right] + r_2 r_3 \frac{\partial u_1}{\partial x_2} + r_3^2 \frac{\partial u_1}{\partial x_3} - r_1^2 \frac{\partial u_3}{\partial x_1} - r_2 r_1 \frac{\partial u_3}{\partial x_2} = r_3 q_1 - r_1 q_3 \quad \text{Equation 2-17}$$

In principle, four measurements of zone axes shifts $\boldsymbol{q}$ at widely spaced directions $\boldsymbol{r}$ in EBSD patterns are sufficient to directly calculate $\frac{\partial u_2}{\partial x_1}, \frac{\partial u_3}{\partial x_1}, \frac{\partial u_1}{\partial x_2}, \frac{\partial u_3}{\partial x_2}, \frac{\partial u_1}{\partial x_3}, \frac{\partial u_2}{\partial x_3}, \left[\frac{\partial u_1}{\partial x_1} - \frac{\partial u_3}{\partial x_3}\right], \left[\frac{\partial u_2}{\partial x_2} - \frac{\partial u_3}{\partial x_3}\right]$. The terms $\frac{\partial u_1}{\partial x_1}, \frac{\partial u_2}{\partial x_2}, \frac{\partial u_3}{\partial x_3}$ cannot be obtained directly because they result in hydrostatic dilation or contraction which does not cause any movements on the EBSD patterns. However we can apply Hooke's law and write the stress $\boldsymbol{\sigma_{33}}$ along the sample normal in terms of strain and elastic constants. Since the EBSD measurement is very close to free surface (10-20nm), it is not unreasonable to assume normal stress $\boldsymbol{\sigma_{33}}$ is close to zero at the surface. This assumption allows the three unknown terms to be determined.

The displacement gradient tensor can be further split into symmetrical and asymmetric parts which correspond to elastic strain $\boldsymbol{e_{ij}}$ and rotation $\boldsymbol{w_{ij}}$, where

$$\boldsymbol{e_{ij}} = \frac{1}{2}\left(\frac{\partial u_i}{\partial x_j} + \frac{\partial u_j}{\partial x_i}\right) \quad \text{Equation 2-18}$$

$$w_{ij} = \frac{1}{2}\left(\frac{\partial u_i}{\partial x_j} - \frac{\partial u_j}{\partial x_i}\right)$$ Equation 2-19

In practice, in order to obtain more statistically reliable results, a robust iterative method[133] is used to find the best fit solutions from at least twenty measured shifts between the reference pattern and testing patterns within each grain. Twenty plus subregions were widely spread across EBSD patterns. These subregions are subsequently transformed in to Fourier (or frequency) domain using Fast Fourier Transform (FFT). This process provides two primary benefits namely higher computational efficient and ability to apply high pass and low pass frequency filters to improve image quality. The shift of each subregion at the same location on the reference pattern and the test one is determined using the two-dimensional cross-correlation function and sub-pixel precision through upsampling.

Two parameters namely the peak height (PH) and mean angular error (MAE) are introduced to assess the quality of pattern shifts measurement. Peak height examines the similarity of features between two subregions at the same positions on the reference and test EBSD patterns. PH are normalised to bring the peak height for the reference pattern to unity. The PH of an EBSP is determined by obtaining the geometrical mean of PH for all subregions. A number of factors affect the peak height value such as the severe plastic deformation, surface contamination, electron beam stability and etc. The MAE is a measurement of the inconsistency between measured shifts from all subregions and the best fit solution obtained from the robust fitting method. In general threshold values of (PH>0.25 and MAE<0.08 rads)

are applied in cross-correlation shifts measurement to ensure reliable results are determined. A systemic study on how to select appropriate values of these two parameters based on experimental and simulated ESBD patterns were carried out by Britton and et al [133].

By performing cross-correlation on all constituent grains, the associated elastic strain and rotation at each EBSD probing point are recovered and ready for estimating GND content.

It is worth to noting that the obtained elastic strain is only relative rather than absolute elastic strain as the strain levels present in the selected reference patterns are unknown. However, as the magnitude of elastic strain is considerably smaller than lattice rotation as seen in our analysis, it can be neglected in determination of GND content. Hence the newly developed remapping method is not used in GND density analysis.

## 2.4 Analysis for GND content

The analysis for GND content adopted in our methodology is based in Wilkinson and Randman 2010 paper on GND distribution near nanoindents [15].

The GND density is deduced from Nye's dislocation tensor components that are initially derived from the displacement vector field.

Physical continuity is required in the displacement field, and thus integration of it over any closed loops, should result in a closure:

$$\oint_c \boldsymbol{du} = 0 \qquad \text{Equation 2-20}$$

Since $\boldsymbol{A}$ is the displacement gradient tensor and $\boldsymbol{A} = \frac{du}{dx}$ and thus $du = \boldsymbol{A}dx$.

This results in Equation 2-21:

$$\oint_c \boldsymbol{A}\, dx = 0 \qquad \text{Equation 2-21}$$

According to Stoke's theorem, the integration around C can be replaced by integration over any surface patch S bounded by C. Furthermore the displacement gradient tensor can be split into an elastic part and a plastic part. Therefore the Equation 2-21 can be rewritten as:

$$\oiint_s curl(\boldsymbol{A})ds = \oiint_s curl(\boldsymbol{A}^e + \boldsymbol{A}^p)ds = 0 \quad \text{Equation 2-22}$$

From Equation 2-22 we can see that over any closed loop C bounding any surface patch S, the curl of elastic displacement gradient tensor must equal to the negative curl of plastic displacement gradient tensor:

$$curl(\boldsymbol{A}^e) = -curl(\boldsymbol{A}^p) \quad \text{Equation 2-23}$$

Within a Burgers circuit, the net Burgers vector B is defined as:

$$B = -\oint_c \boldsymbol{A}^p dx = -\oiint_S curl(\boldsymbol{A}^p)ds \quad \text{Equation 2-24}$$

And Nye's dislocation tensor $\boldsymbol{\alpha}$ is defined as[13]:

$$\boldsymbol{B} = \oiint_s \boldsymbol{\alpha} ds \quad \text{Equation 2-25}$$

Therefore:

$$\boldsymbol{\alpha} = -curl(\boldsymbol{A}^p) = curl(\boldsymbol{A}^e) \quad \text{Equation 2-26}$$

The term $\boldsymbol{A}^e$ in Equation 2-26 can be explicitly expressed in terms of individual components of the elastic strain gradient and rotation gradient [55], thus

$$\boldsymbol{\alpha} = \begin{pmatrix} \frac{\partial w_{12}}{\partial x_3} - \frac{\partial w_{13}}{\partial x_2} & \frac{\partial w_{13}}{\partial x_1} & \frac{\partial w_{21}}{\partial x_1} \\ \frac{\partial w_{32}}{\partial x_2} & \frac{\partial w_{23}}{\partial x_1} - \frac{\partial w_{21}}{\partial x_3} & \frac{\partial w_{21}}{\partial x_2} \\ \frac{\partial w_{32}}{\partial x_3} & \frac{\partial w_{13}}{\partial x_3} & \frac{\partial w_{31}}{\partial x_2} - \frac{\partial w_{32}}{\partial x_1} \end{pmatrix} + \begin{pmatrix} \frac{\partial \epsilon_{12}}{\partial x_3} - \frac{\partial \epsilon_{31}}{\partial x_2} & \frac{\partial \epsilon_{13}}{\partial x_1} - \frac{\partial \epsilon_{11}}{\partial x_3} & \frac{\partial \epsilon_{11}}{\partial x_2} - \frac{\partial \epsilon_{12}}{\partial x_1} \\ \frac{\partial \epsilon_{22}}{\partial x_3} - \frac{\partial \epsilon_{23}}{\partial x_2} & \frac{\partial \epsilon_{23}}{\partial x_1} - \frac{\partial \epsilon_{21}}{\partial x_3} & \frac{\partial \epsilon_{21}}{\partial x_2} - \frac{\partial \epsilon_{22}}{\partial x_1} \\ \frac{\partial \epsilon_{32}}{\partial x_3} - \frac{\partial \epsilon_{33}}{\partial x_2} & \frac{\partial \epsilon_{33}}{\partial x_1} - \frac{\partial \epsilon_{31}}{\partial x_3} & \frac{\partial \epsilon_{31}}{\partial x_2} - \frac{\partial \epsilon_{32}}{\partial x_1} \end{pmatrix}$$

Equation 2-27

As the HR-EBSD measurement only determines the gradients of the elastic strain and rotation in two dimensions (i.e. within the surface plane), any gradient with respect to the third direction $x_3$ is not accessible as highlighted(red) in

$$\boldsymbol{\alpha} = \begin{pmatrix} \frac{\partial w_{12}}{\partial x_3} - \frac{\partial w_{13}}{\partial x_2} & \frac{\partial w_{13}}{\partial x_1} & \frac{\partial w_{21}}{\partial x_1} \\ \frac{\partial w_{32}}{\partial x_2} & \frac{\partial w_{23}}{\partial x_1} - \frac{\partial w_{21}}{\partial x_3} & \frac{\partial w_{21}}{\partial x_2} \\ \frac{\partial w_{32}}{\partial x_3} & \frac{\partial w_{13}}{\partial x_3} & \frac{\partial w_{31}}{\partial x_2} - \frac{\partial w_{32}}{\partial x_1} \end{pmatrix} + \begin{pmatrix} \frac{\partial \epsilon_{12}}{\partial x_3} - \frac{\partial \epsilon_{31}}{\partial x_2} & \frac{\partial \epsilon_{13}}{\partial x_1} - \frac{\partial \epsilon_{11}}{\partial x_3} & \frac{\partial \epsilon_{11}}{\partial x_2} - \frac{\partial \epsilon_{12}}{\partial x_1} \\ \frac{\partial \epsilon_{22}}{\partial x_3} - \frac{\partial \epsilon_{23}}{\partial x_2} & \frac{\partial \epsilon_{23}}{\partial x_1} - \frac{\partial \epsilon_{21}}{\partial x_3} & \frac{\partial \epsilon_{21}}{\partial x_2} - \frac{\partial \epsilon_{22}}{\partial x_1} \\ \frac{\partial \epsilon_{32}}{\partial x_3} - \frac{\partial \epsilon_{33}}{\partial x_2} & \frac{\partial \epsilon_{33}}{\partial x_1} - \frac{\partial \epsilon_{31}}{\partial x_3} & \frac{\partial \epsilon_{31}}{\partial x_2} - \frac{\partial \epsilon_{32}}{\partial x_1} \end{pmatrix}$$

Equation 2-28

The inaccessible third dimension limits the number of directly determined Nye's tensor components to three of nine. However, based on our observation on our direct experimental results, it was found that the elastic

strain contribution is insignificant comparing to rotation. It thus is reasonable to neglect the elastic strain part in Nye's tensor, which yields:

$$\boldsymbol{\alpha} = \begin{pmatrix} \frac{\partial w_{12}}{\partial x_3} - \frac{\partial w_{13}}{\partial x_2} & \frac{\partial w_{13}}{\partial x_1} & \frac{\partial w_{21}}{\partial x_1} \\ \frac{\partial w_{32}}{\partial x_2} & \frac{\partial w_{23}}{\partial x_1} - \frac{\partial w_{21}}{\partial x_3} & \frac{\partial w_{21}}{\partial x_2} \\ \frac{\partial w_{32}}{\partial x_3} & \frac{\partial w_{13}}{\partial x_3} & \frac{\partial w_{31}}{\partial x_2} - \frac{\partial w_{32}}{\partial x_1} \end{pmatrix} \quad \text{Equation 2-29}$$

Ignoring the elastic strain part allows five of nine Nye's tensor components to be obtained directly. In addition, as Pantleon pointed out that the difference between $\boldsymbol{\alpha_{11} - \alpha_{22}}$can also be obtained and used as a further constraint to improve the accuracy of estimated lower bound GND content. Several groups have attempted to access full Nye's tensor by using 3D EBSD measurement in which EBSD maps was generated and combined on series of focus ion beam (FIB) sectioned surface layers [143, 144] or using the measured 2D strain field to further deduce the full Nye's tensor [145] . However, in the 3D FIB+SEM technique is time consuming and difficulty arises when aligning all 2D maps from the sectioned surface layers into a 3D data set. The alignment (translational and angular) between layers is considerably lower resolution than within each layer and alignment procedures are less reliable for deformed sample that is of the interest here. The additional information is thus of poor quality and may generate significant artefacts.

The Nye's tensor relates to dislocation density $\rho_s$ of different types of dislocations through:

$$\boldsymbol{\alpha}_{ij} = \sum_{s=1}^{s_{max}} \rho_s \boldsymbol{b}_i^s \boldsymbol{l}_j^s$$

Equation 2-30

Where $\boldsymbol{b}^s$ and $\boldsymbol{l}^s$ are the Burgers vector and unit line direction of the sth dislocation type respectively. The Equation 2-30 can be written out more explicitly in terms of individual components of rotation gradient, Burgers vector, line direction and dislocation density as shown in Equation 2-31.

$$\begin{pmatrix} \alpha_{12} \\ \alpha_{13} \\ \alpha_{21} \\ \alpha_{23} \\ \alpha_{33} \\ \alpha_{11} - \alpha_{22} \end{pmatrix} = \begin{pmatrix} \frac{\partial w_{13}}{\partial x_1} \\ \frac{\partial w_{21}}{\partial x_1} \\ \frac{\partial w_{32}}{\partial x_2} \\ \frac{\partial w_{21}}{\partial x_2} \\ \frac{\partial w_{31}}{\partial x_2} - \frac{\partial w_{32}}{\partial x_1} \\ -\frac{\partial w_{13}}{\partial x_2} - \frac{\partial w_{23}}{\partial x_1} \end{pmatrix} = \begin{pmatrix} \sum_s b_1^s l_2^s \rho_s \\ \sum_s b_1^s l_3^s \rho_s \\ \sum_s b_2^s l_1^s \rho_s \\ \sum_s b_2^s l_3^s \rho_s \\ \sum_s b_3^s l_3^s \rho_s \\ \sum_s b_1^s l_1^s \rho_s - b_2^s l_2^s \rho_s \end{pmatrix}$$

Equation 2-31

In Equation 2-31, the $\alpha_{ij}$ terms are generally represented by a vector $\boldsymbol{\Lambda}$ and the $\boldsymbol{A}$ is used to denote the various terms in the tensor products of the

Burgers vector ***b*** and line direction ***l*** of the sth dislocation types. Therefore, the Equation 2-31 can be simply expressed as:

$$\Lambda = A\rho$$

Equation 2-32

It is noted that in Equation 2-32 on the left hand side there are 6 measureable rotation gradients available, whereas on the right hand side in case of FCC crystals if we only consider pure edge and pure screw dislocations with positive and negative signs, there are potentially 36 slip systems to store dislocations: a set of 12 pure screw dislocations whose Burgers vectors and line directions lie in the <110> directions, and 24 pure edge dislocations whose Burgers vectors lie in <110> directions with line directions along <112> as explored by Arsenlis and Parks[120]. We can unambiguously determine all Nye's tensor components if the magnitudes of dislocations on individual possible slip systems are known. Conversely if we measure Nye's tensor components and try to find the distribution of dislocation on each slip systems. Similar to identification of five slip systems in Taylor's theory, this becomes an over determined problem. Thus there is no unique solution and a set of possible combinations of slip systems can satisfy measured curvature.

There are various methods available to solve this over determined problem. Generally these methods minimise a critical parameter in the problem to generate the most reasonable combination. In this work the more physical based $L^1$ optimisation scheme with line energy minimisation is used in which the solution with the least sum of dislocation line energy will be found. The $L^2$ optimisation scheme is also employed by various authors for example Field and et al [123] which minimises the sum of squares of dislocation density and

is mathematically simpler (it can be solved using a matrix invesion), the $L^2$ optimisation scheme lacks of physical relevance [15].

In our $L^1$ optimisation scheme all dislocations have the same Burgers vector but the energy associated with edge and screw dislocations are different according to Equation 2-33. This $L^1$ optimisation scheme is implemented in Matlab (http://www.mathworks.co.uk ) using the 'linprog' command [146].

$$\frac{E_{edge}}{E_{screw}} = \frac{1}{1-v} \qquad \text{Equation 2-33}$$

Where $v$ is the Poisson's ratio with a value of 1/3 for typical metals, and $E$ is the associated energy for edge and screw dislocations.

Finally, it should be noted that the cross-correlation displacement gradient measurements and GND density measurements were made in a newly developed programme rather than the commercially available software: CrossCourt3 (http://www.blgproductions.co.uk/) due to the difficulty of handling a large number of grains.

# Chapter 3. GND Density Measurement Sensitivity: Effects of Detector Binning and Step Size

HR-EBSD is an off-line image processing method and it requires high quality full resolution EBSPs to be captured during EBSD scans when the aim is to extract the highest sensitivity, GND density and elastic strain data [24-29, 136]. Typically the highest bit depth patterns combined with minimum gain and contrast stretching and 1x1 camera binning on a 1K x1K pixel camera is employed. Acquiring patterns of this quality requires long (~1 second) exposure time which can result in experiments with relatively small maps being collected. For example, at 1 second exposure time, 12 hour allows collection of 43,200 data points, so that a little over 100x100μm area can be mapped with a 0.5μm step size. The amount of probed data is sufficient to study GND density distributions around specific microstructure features such as selected grain boundaries [147], carbides in single crystal [28], nano-indentation [25] and crack tip [148]. However, larger datasets would be attractive in providing better representative sampling of the inhomogeneity of deformation in polycrystalline materials.

Larger maps could be obtained if either larger step sizes were employed or a shorter exposure time was used. Altering the step size clearly has implications for the division of dislocation density into GND and SSD contributions but also affects the measurement noise on the lattice curvatures. Shorter exposure times can readily be achieved by binning the output from

the CCD. This chapter presents systematic investigations of the effects on GND density measurement of the step size and binning.

## 3.1 Binning size effect

Binning in a charge-coupled device (CCD) is a process to combine charges contained in adjacent pixels into a single pixel (super-pixel) during readout process. Figure 3-1 illustrates the process of 2x2 binning. Two potential benefits of binning include of the increase in frame rate and/or the improvement in signal to noise ratio (SNR) at the expense of reduction in spatial resolution on the images. The slowest step in image acquisition is the exposure time which effectively is a process to collect sufficient charge (signal) to form an image. Low exposure time can be applied to achieve high frame rates, if highly binned low-resolution images are acceptable.

In addition, there is a higher SNR due to a decrease in the contribution from read out noise as it is added to super-pixels which contains accumulated charge from multi pixels [33]. In our case, SNR does not increase remarkably with binning size since the exposure time is reduced. In other words, though the read out noise is reduced by binning process, the signals collected on each pixel are reduced as well. Thus the overall SNR does not change significantly.

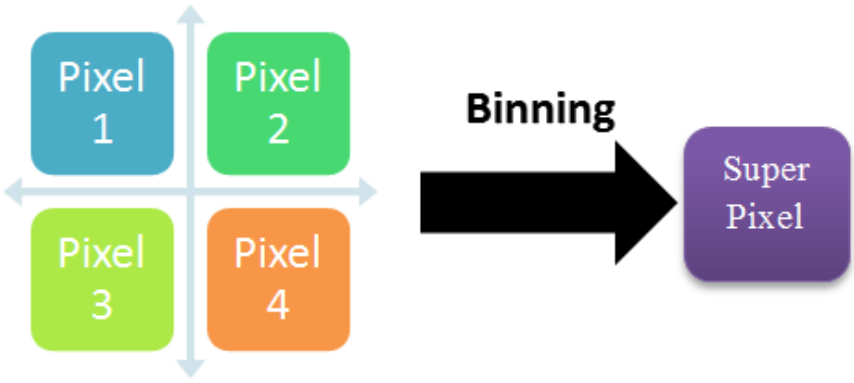



**Figure 3-1, Schematic diagram shows the CCD 2x2 binning process. The charge collected from pxiel 1 to 4 are summed into the single pixel (super-pixel) during readout process prior to digitaliztion. The accumulated charge in the super-pixel equals to $\sum_1^4 charge\ in\ pixel$**

### 3.1.1 Baseline measurement on Si

To assess the precision of GND measurement with different levels of binning, a study of scatter in pattern shift and displacement gradient components was undertaken. In order to induce a uniform shift between patterns, the electron beam was deflected 50nm from point to point to form 60 x60 points arrays on a single crystalline silicon sample. The single crystal of silicon was oriented such that the [001] direction pointed out the plane and the two perpendicular <110> directions pointed along the X and Y axes. Four 60x60 arrays of EBSD patterns were captured with different binning levels of 1x1, 2x2, 4x4 and 8x8. All EBSD measurements were conducted on a JEOL JSM6500F operating at 20kV accelerating voltage and ~10nA probe current. A 12 bit 1300 x 1030 pixels CCD camera was used to record EBSD patterns with minimum brightness or contrast augmentations available with OIM v5.3 (TSL-EDAX, Utah). The exposure time was 1.040 seconds for the unbinned detector and was successively reduced by a factor of ~4; to 0.260 seconds, 0.065 seconds and 0.018 seconds as the level of hardware binning was increased.

To ensure obtaining reliable shifts measurements, a minimum number of twenty regions of interests (ROIs) should be used in cross correlation analysis Wilkinson et al [21]. To further improve the robust measurement of lattice rotation, more ROI may be used. However beyond thirty ROIs only subtle further improvement in sensitivity will be observed and as the computational time is proportional to the number of subsets employed in cross-correlation analysis there will be a significant cost involved. Thirty ROIs give good balance between the sensitivity of shifts measurement and computational expense. Thirty ROIs were distributed across the patterns with one at the centre and remainder in a circle around the bounds of the circular phosphor. Within each grain, a pattern with the highest image quality was used as the reference point. The sizes of ROIs were changed (256x256; 128x128; 64x64; 32x32) according to the pattern sizes (916x916; 455x455; 226x226; 111x111). High pass and low pass filters were applied on each ROI and adjusted visually as the ROIs were made smaller. Shifts between the reference pattern and each test one were measured in horizontal (x) and vertical directions (y) respectively. As the distance between any two adjacent data points in the map is constant, the relative shifts between a data point and its subsequence point were determined to evaluate the shift measurement sensitivity. The corresponding mean values and the standard deviation values were determined in each binning test. The mean value of the relative shifts was 50nm (step size) while the standard deviation increases as the camera binning level rises up. The average values of standard deviation from the shifts in x and y directions were obtained and plotted as a function of

binning size as shown in Figure 3-2. In addition, the corresponding angular resolution at each binning level was also calculated according to Equation 3-1.

$$Angular\ resolution = \frac{Shift\ sensitivity}{Pattern\ size} \qquad \text{Equation 3-1}$$

Where shift sensitivity is obtained from the standard deviation of pattern shifts in pixel, pattern size is defined as $Z^*$ (detector distance as fraction of the pattern width) times the width of EBD patterns in pixels.

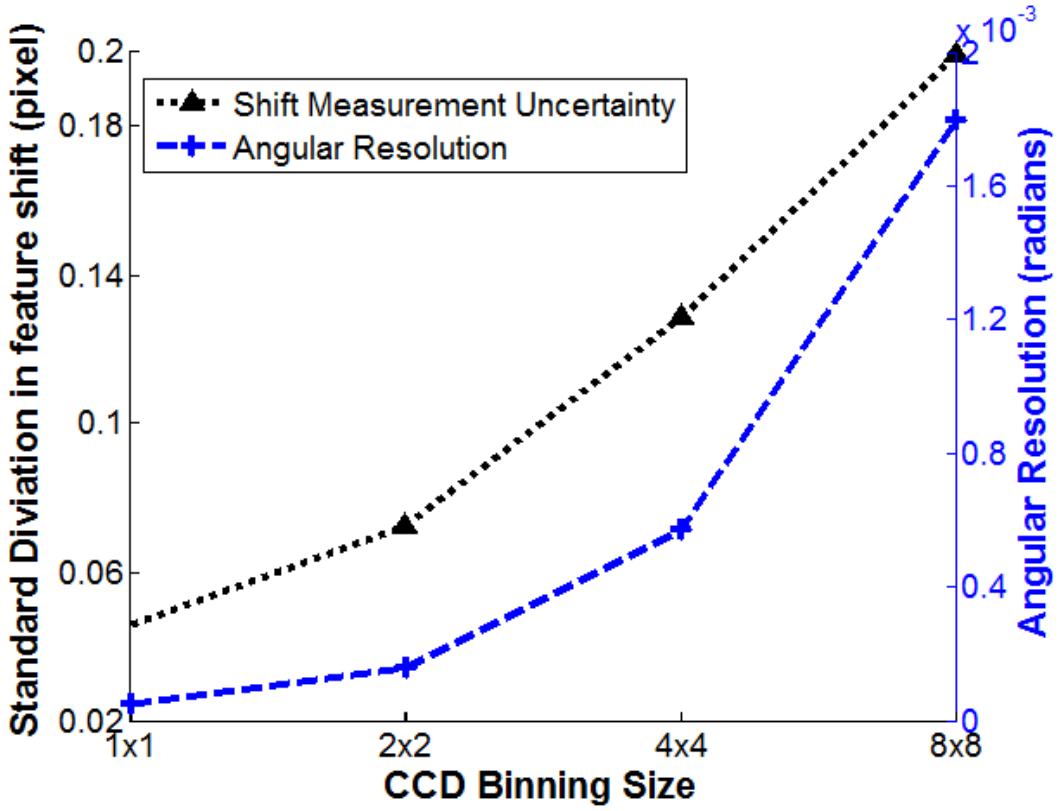



**Figure 3-2, Effect of CCD Binning size on the scatter (precision) of shifts measurements and angular resolution**

It is clear that the increase in binning size leads to an increase in standard deviation in feature shift. When the full CCD resolution (1x1 binning) was used, the best quality EBSPs was collected and largest ROIs were used which allows the highest sensitivity in shift measurement 0.046 pixels to be

obtained. This shift sensitivity corresponds to an angular uncertainty of $5x10^{-5}$ radians. This is in good agreement with the sensitivity ($7x10^{-5}$ radians) claimed by Wilkinson [22]. As binning size increases, smaller size EBSPs were captured, smaller ROIs were utilised which all result in higher scatter values in shift measurements and angular resolution.

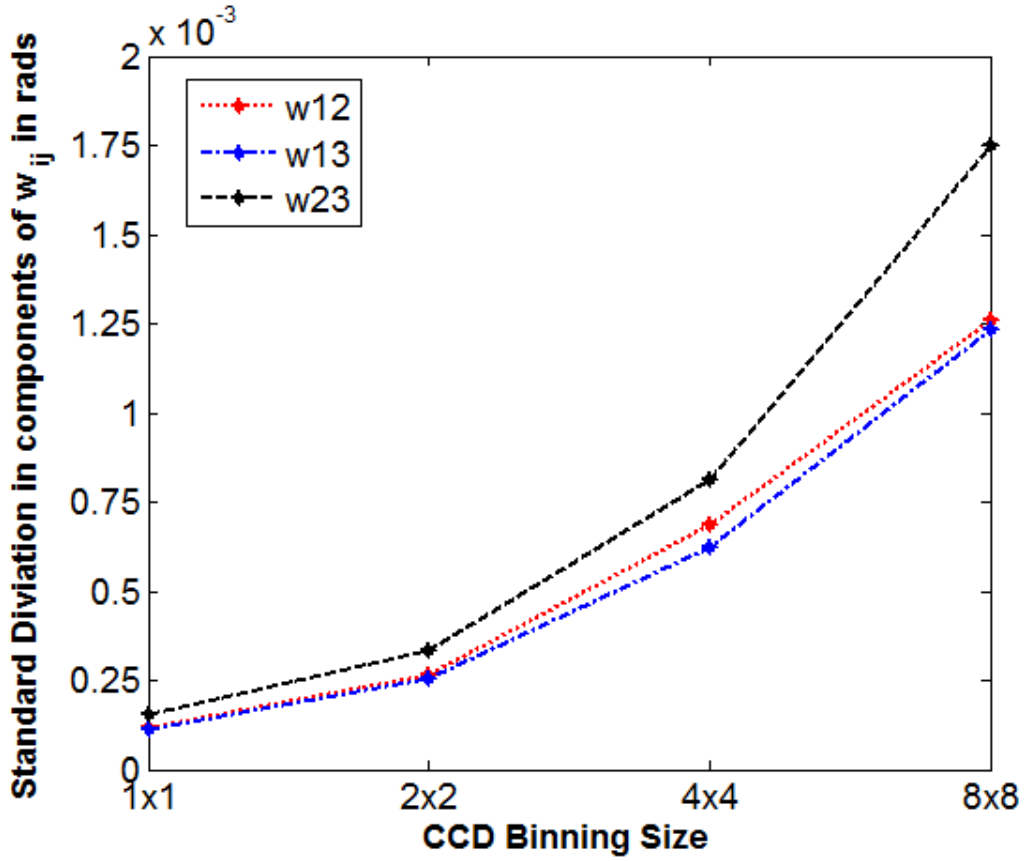



**Figure 3-3, Standard deviation measured rotation and elastic strain components by cross-correlation method with variable software/hardware binning.**

The single crystal Si contains virtually no residual strain and no lattice rotation so that, the values of strain and rotation components determined by cross-correlation analysis are solely due to measurement noise. The standard deviations of three rotation components were extracted and are shown as a function of binning level in Figure 3-3. The average of standard deviations from all nine strain and rotation components was determined to be $1.5x10^{-4}$ at

1x1 binning which is in accord with the value claimed by Wilkinson, Meaden and Dingley [21]. The average scatter values increases as much as ten times as the binning level increases from 1x1 to 8x8. It is noted that the standard deviation value in the extreme case of 8x8 binning we trade ~12 times less precision for a factor ~55 times faster acquisition speed.

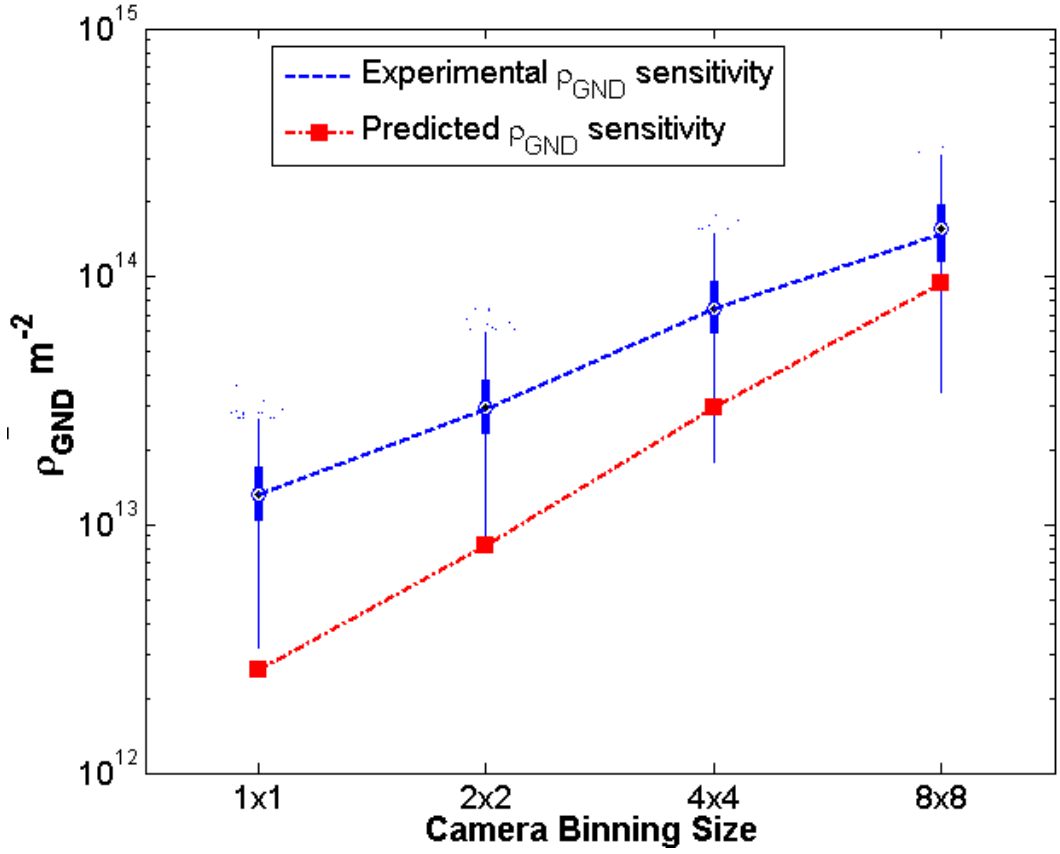



**Figure 3-4, shows the GND density variations in silicon as a function of camera binning size. Blue line is a box plot of the experimentally measured dislocation density on the silicon sample using 50nm step size and 0.3839nm burger's vector length. At each binning level, median points are joined by the blue dashed line and positions of lower quartile and upper quartile are shown as the lower and upper edges of the boxes. Whiskers show the ranges of data between 5% and 95% while the outliers are shown as individual points scattered around whiskers. The red line is corresponding to the predicted lower bound GND density sensitivity as calculated using Equation 3-1. The GND values plotted above were determined as their arithmetic mean.**

The lattice rotation measurements on Si were then analysed using our L1 minimum line energy GND analysis routine to establish the noise level on GND density measurements. A plot showing the lower bound GND density distribution as a function of CCD camera binning size is shown in Figure 3-4.

The arithmetic mean of GND density noise floor increases approximately linearly on log scale with binning level, as shown by the blue dashed line in Figure 3-4. At the full unbinned resolution of the camera noise on the measured rotations leads to a GND density of $1.4 \times 10^{13}$ $m^{-2}$ in accord with Randman & Wilkinson's findings [27]. A relatively high GND density ($1.6 \times 10^{14} m^{-2}$) arises purely from noise when 8x8 binning is utilised. In practice, recovered GND density data is only considered to be reliable when the GND density is above this noise floor. In other words, if 8x8 binning is chosen, the sample must be highly deformed and therefore contain a high dislocation density for this analysis method to be worthwhile. Experimentally determined GND density shifts up by a factor of 11.5 (~1.06 at log scale) from 1x1 binning to 8x8 binning. This indicates that if the angular resolution becomes worse, the noise floor consistently increases. It is also found that the predicted lower bound GND density sensitivity which is obtained from Equation 3-2 is smaller than experimental determined GND resolution especially at 1x1 binning.

$$\rho_{min}^{gnd} = \frac{\textbf{Angular resolution(in radians)}}{\textbf{Step size} \times \textbf{Burger's vector length}} \qquad \text{Equation 3-2}$$

Where the angular resolution values are determined in previous shift measurement, step size of 50nm is used and the burger's vector length is 0.3839nm for Si.

The difference between the experimentally determined noise floor and that predicted from Equation 3-2 becomes smaller with larger binning size. It suggests that the relationship between angular resolution and GND density is

not linear and a further factor may need to be introduced in Equation 3-2. Equation 3-2 arises from the simple analysis of rotations about a single axis being generated by a single type of GND. However in practice, GND density is determined from misorientations about three rotation axes rather than one, and each misorientation is not measured independently, and hence it is not unreasonable to suggest that the uncertainty in GND density determination should be somewhat higher than predicted from Equation 3-2. In addition, when applying linear minimisation method (L1 in our case) to determine the GND density with minimum energy, it is difficult to determine the errors may be induced in this analysis step as well. However, as shown in Figure 3-4, even in the worst case (1x1 binning), the difference between measured GND density noise floor and predicted from Equation 3-2 is only three times (~0.5 at $\log_{10}$ scale).

### 3.1.2 Analysis of deformed Cu polycrystal

The effect of binning on the GND noise floor using a near perfect Si crystal has been studied in the preceding session. How critical this is for analysing dislocation substructure in deformed copper sample is to be examined. An oxygen-free high conductivity (OFHC) polycrystalline copper sample deformed to 10% tensile strain was analysed. The specimen was polished with 50nm colloidal silica slurry to a mirror finish and followed by an electro-polishing (85% phosphoric acid, 1.2 volt for 2 minutes) to remove any polishing defects. Finally, JEOL cross-sectional polisher was used for which Argon atoms were incident on sample surface at 3keV for 15 minutes to remove any residual surface contamination. A 113μm x 113μm EBSD map was captured (as shown in Figure 3-5)) using OIM DC v5.3 (TSL-EDAX)

EBSD system in a JEOL 6500F with accelerating voltage of 20kV and ~10nA probing current. The space between neighbour points was 0.5μm and all EBSPs were recorded along the scan. The highest quality images were acquired using 12 bits, ~1k x 1k resolution with 1 second exposure per pattern.

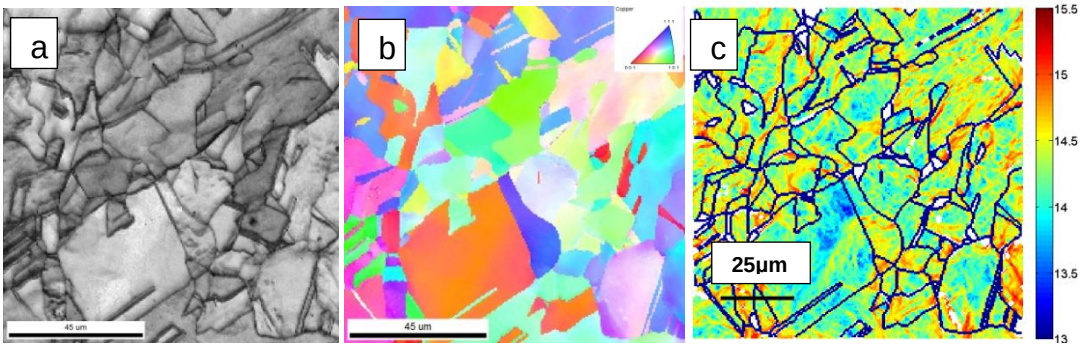



**Figure 3-5, a. Image quality figure of polycrystalline copper deformed in 10% tension where bright area has relatively high quality and dark region corresponds to relatively low quality; b. Orientation map of sampled region from copper polycrystal with the colours corresponding to the surface crystal plane normal directions; c. GND density map generated using 0.5μm step size and the colour scale is at log 10 scale of dislocations per $m^2$. The loading direction is along the vertical direction of the map.**

As super pixels are formed by summing charges from adjacent pixels (Figure 3-1) and the exposure time varies with binning levels, the total amount of received signals in the super pixels should remain constant. A reduction in the pattern size was performed in Matlab to emulate binning by extracting every one pixel from a square of 4, 16, 64 and 256 pixels. The simulation process on 2x2 binning is shown in Figure 3-6 as an example in which the signal stored in one pixel of four was extracted to form a super pixel. Using this fractional binning will lose many features and lead to a worse pattern than those obtained with hardware binning as fractional binning extracts only single pixel from a square array of 2x2, 4x4 ….. However, using averaging method will improve the SNR significantly as the exposure time does not reduce and so the pattern will be clearer than those obtained with hardware

binning. In practice, the experimental EBSD pattern should be somewhere between these two extremes and closer to fractional one. Furthermore, the error limits are wished to be explored and therefore the worst case will improve our confidence in our experimental results. These patterns were analysed using cross-correlation with similar settings as used for the Si previously.

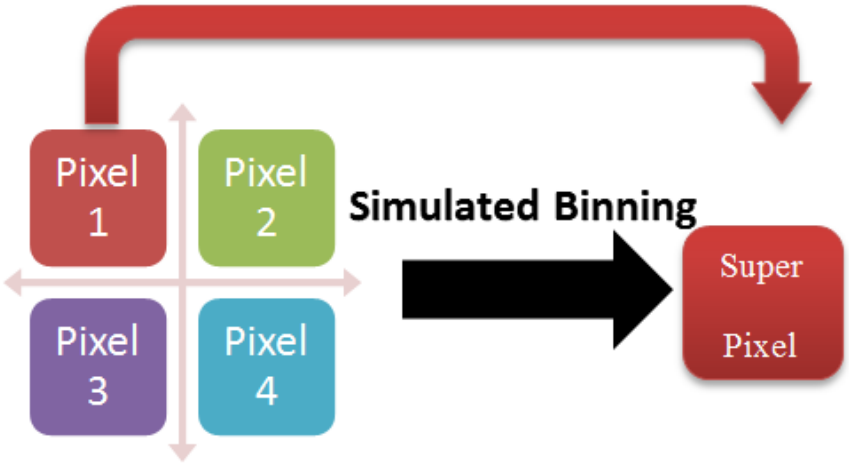



**Figure 3-6,** ***schematic diagram shows of simulation of binning to reduce the image size. One pixel in group of four in the 1x1 binning image is extracted to reduce the image size.***

In Figure 3-8, examples of EBSP at each binning level are shown together with the overall correlation PH maps, MAE maps and GND density maps. In general as the binning increases, values of PH decrease and MAE increase, especially near grain boundaries indicating a reduction in the quality of the data. The acceptable solving rate at binning levels of 1x1, 2x2, 4x4, 8x8 and 16x16 are 78.0%, 76.9%, 73.0%, 70.1% and 3.1%. We can see that even at 4x4 and 8x8 binning, there is only a small fraction of points which fall below the MAE and PH thresholds of MAE<0.008 radians and PH>0.2 which were kept the same at each binning level. Little variation in GND density maps is observed at 2x2 and 4x4 binning as can be seen in Figure 3-8. Even at 8x8

binning, the relative high (hot) and low (cold) GND density spots remain at the same locations, although the average GND density is elevated slightly. At 16x16 binning, GND density analysis failed significantly. No reliable results can be obtained because the majority of points in the map fell below the MAE threshold. The variation of the median values of GND density as a function of binning level is shown in Figure 3-7 which confirms that the general GND density distributions stay relatively constant as the degree of pattern binning is increased from 1x1 to 8x8, before the analysis fails dramatically at 16x16 binning.

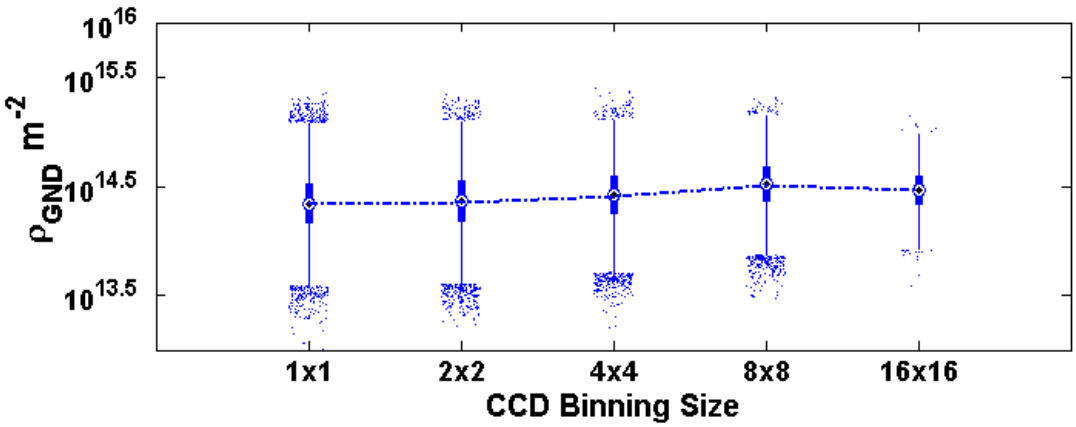



**Figure 3-7, Box and whisker plots shows the distributions of GND density in tensile 10% strain copper as a function of CCD binning size. At each binning level, middle points were determined as the median value of that GND dataset, box shows the quartile range(25% to 75%) of GND distribution; whiskers indicate where the 5% and 95% lines are and scatter points at the two end of whikers are outliers beyone the range of 5%-95% of the dataset.**

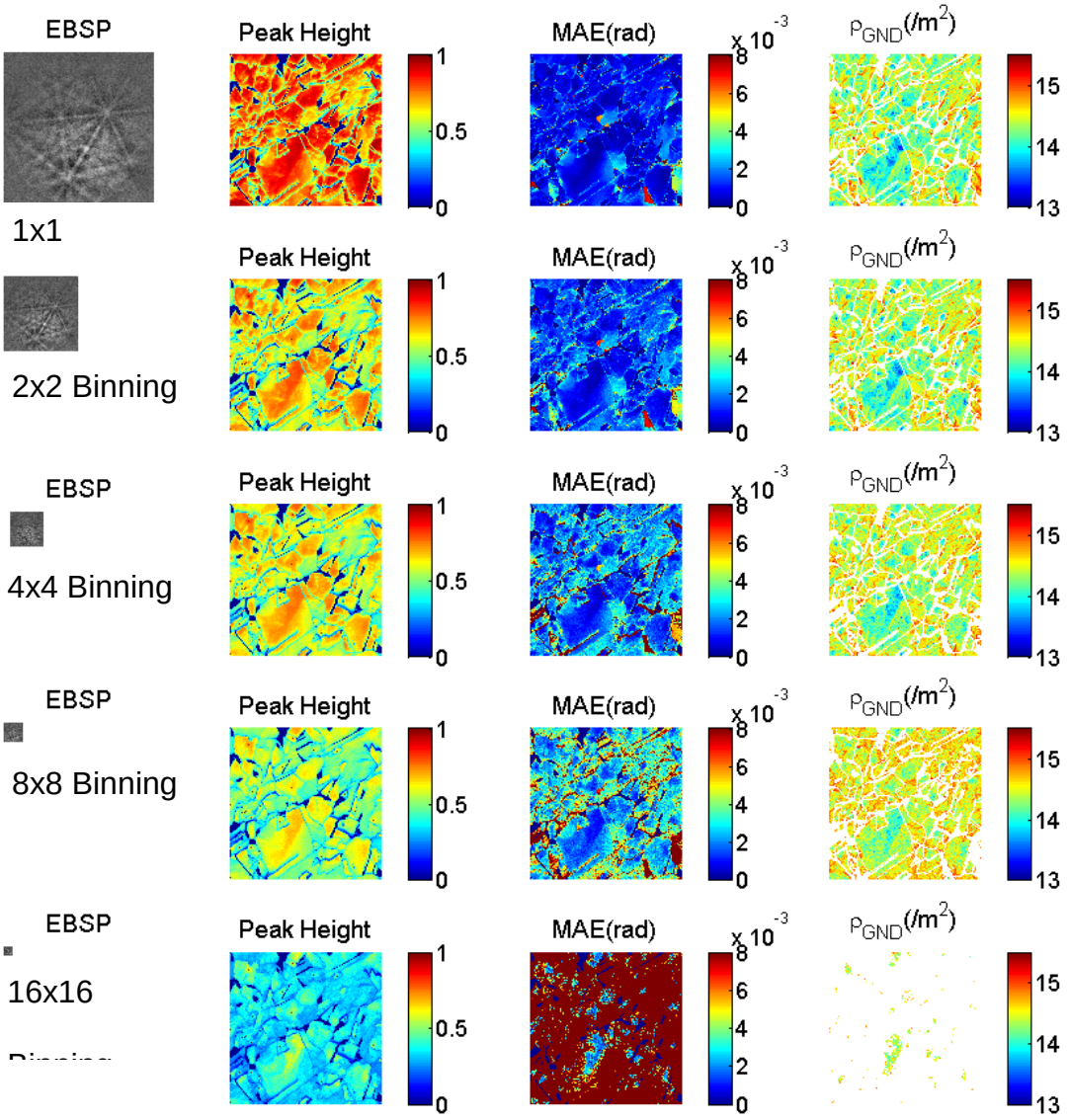



**Figure 3-8, Comparison EBSPs, Peak Height, Mean angular error and GND density as a function of binning size. The EBSPs showing above are taken from the point at row 0 column 140 in the EBSD map. White (transparent) regions in GND density maps corresponds the eliminated points below MAE or PH thresholds.**

## 3.2 Step size effect

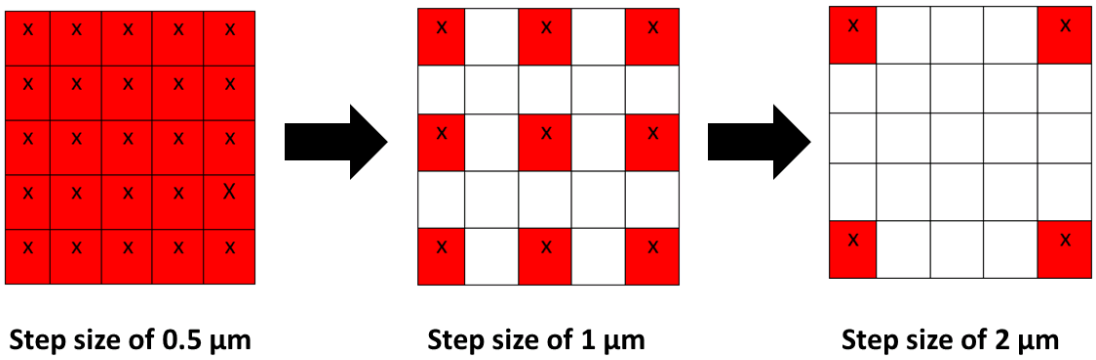



**Figure 3-9, Schematic diagram shows the increase in step size from 0.5µm to 1µm and 2µm on a lattice rotation map. Alternative rows and columns are used into cross-correlation analysis to calculate GND density.**

Separation of dislocations between those which are geometrically necessary and those which are statistically stored depends on the Burger's circuit size (step size in EBSD), with a smaller step size leading to a more desirable result that a greater fraction of the total dislocation density is geometrically necessary. From Nye's analysis, GNDs depend on the net Burger's vector within a Burger's circuit which gives rise to a lattice curvature. In our analysis, we reverse this analysis by measuring the curvature between measurement points and recover a lower bound GND density using the Nye's tensor. Therefore, dislocations with opposite directions such as dipole and multipoles will not result in curvature between measurement pointes and therefore will not be measured as 'geometrically necessary' and they are called Statistically Stored Dislocations (SSDs) which are not measureable using EBSD technique. If smaller Burger's circuit is used (i.e. decreasing the step size), such that the measurement points now separate these dipoles and multiples then more dislocation will be resolved as GNDs. Ultimately, if the Burger's circuit size is smaller than the dislocation dipole size, all dislocations can be

measured as GNDs. However, Equation 3-2 shows that the measurement noise will be amplified increasingly as the step size decreases and furthermore in a fixed extent of microscope time an assessment must be restricted to a smaller area of the sample at the smaller step size. Balancing the conflicting drivers on the steps size imposed by a desire to increase the fraction of dislocation density represented by measureable GNDs and reduce the contribution from noise and map a significant area of sample is complex and would be aided by a systematic study of the effects of step size.

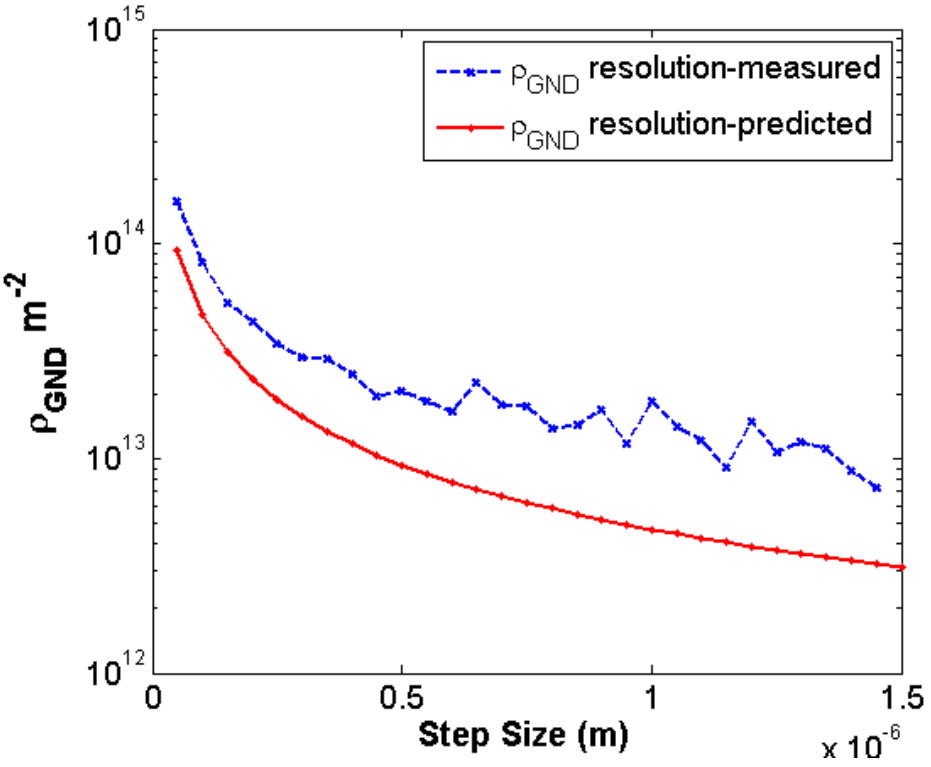



Figure 3-10, GND density variation as a function of step size using the 8x8 binning Silicon map

### 3.2.1 Baseline measurement on Si

To study the noise contribution when step size is reduced, the single crystal silicon map was used as before. It is noted that the 50nm step size is close to likely physical spatial resolution of EBSD in a field emission scanning electron microscope due to the limit of electron interaction volume [99]. The

step size to 1.5μm in increments of 50nm is artificially increased and the GND analysis is performed by removing the alternate rows and columns of the rotation tensor components as illustrated in Figure 3-9. The results of GND density variation as a function of step size is shown in Figure 3-10. The predicted curve was generated from Equation 3-2 in which the angular resolution is determined as 0.0018 radians (see Figure 3-2), the Silicon Burger's vector length is 0.384nm and the step size is increased from 50nm to 1.5μm at increment of 50nm. If angular resolution and Burger's vector length are fixed, the GND density decreased as expected with the increase in step size according to Equation 3-2 and fluctuations appearing near the tail may be caused by sampling issues as the population is reduced from the initial 3600 points to 4 points. This plot demonstrates that at small step sizes, instead of picking out individual dislocations from a dipole pair, the analysis would instead be dominated by noise. Very few dislocations are expected in this unstrained silicon sample as it was made to semiconductor grade. Therefore the recovered GND density arises solely due to measurement noise. Equation 3-2 notes that as the step size decreased the associated noise level increases. This was confirmed by the close agreement of the predicted GND density curve with the measured GND density due to the presence of noise (see Figure 3-10).

Analysis of GND noise maps as shown in Figure 3-11 could result in misinterpretation of the fluctuations as features within the sample which are not really present and so care must be taken in interpreting GND density distributions close to the noise floor. It is also noted that the noise floor is reduced significantly as the step size increases.

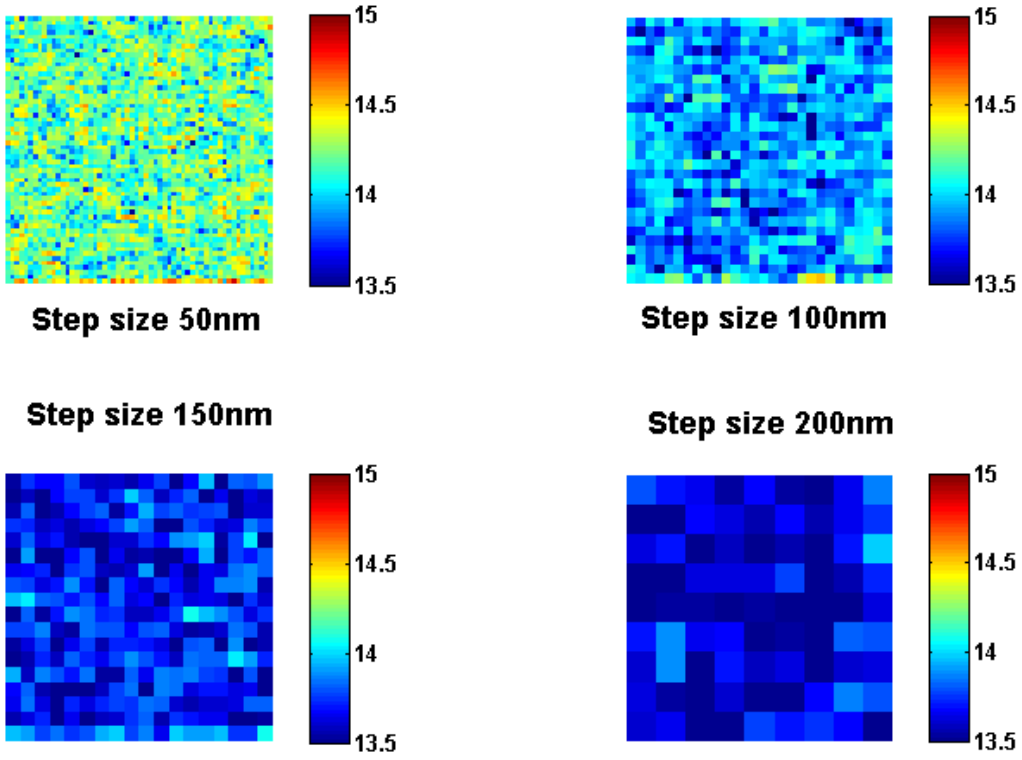



**Figure 3-11, 60μm x 60μm GND density maps with 8x8 binning using step size of 50nm, 100nm, 150nm and 200nm.**

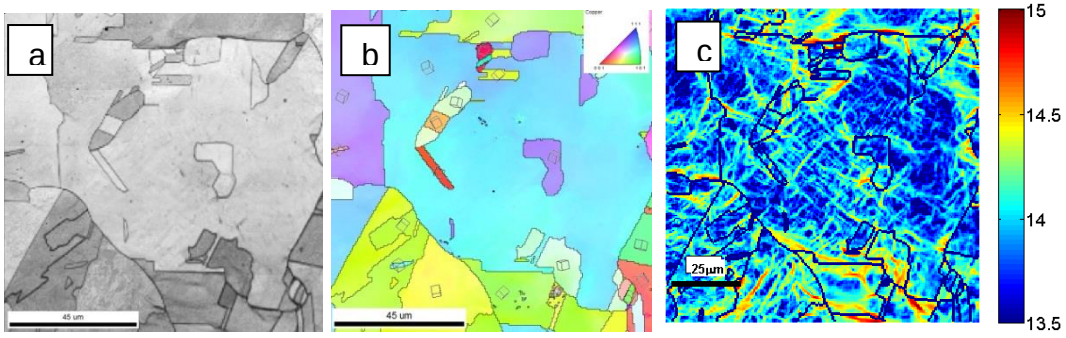



**Figure 3-12, a. Image quality figure of polycrystalline copper deformed in 2% tension where bright area has relatively high quality and dark region corresponds to relatively low quality; b. Orientation map of sampled region from copper polycrystal with the colours corresponding to the surface crystal plane normal directions; c. GND density map generated using 0.5μm step size and the colour scale is at log $_{10}$ scale. The loading direction is along the vertical direction of the map.**

### 3.2.2 Analysis of deformed Cu polycrystal

In practice, the separation of dislocation into GNDs and SSDs is a balance between noise resolution and the structure of dislocation networks found in real materials. We have also examined the effect of step size on GND mapping in a copper sample deformed to 2% plastic strain in tension which

shows clear dislocation cell structure [149]. The OIM image quality map, orientation map and the GND density map obtained using cross-correlation based analysis on patterns obtained with no camera binning are shown in Figure 3-12. The step size was artificially changed from 0.5µm to 10µm at an increment of 0.5µm as before, by removing the alternate rows and columns from rotation tensor components maps.

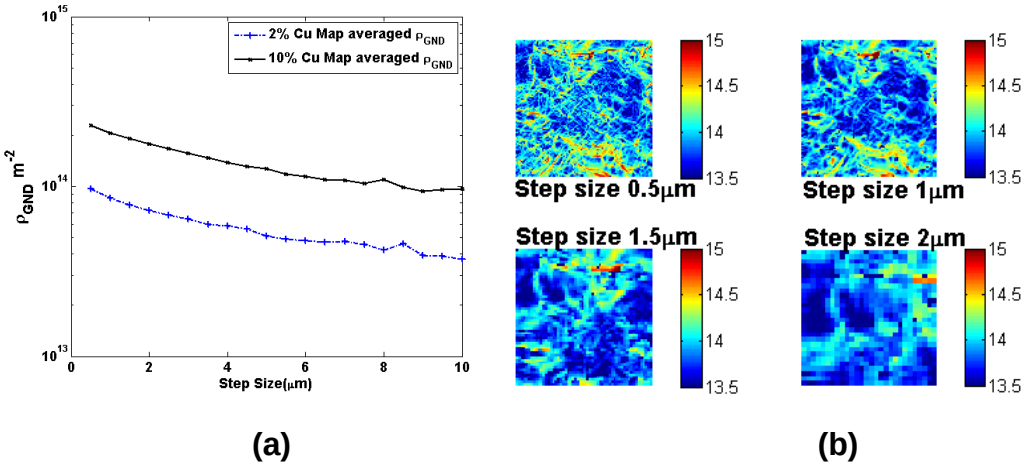



**Figure 3-13, (a) GND density of 2% (see Figure 3-12) and 10% (see Figure 3-5) tensile strained polycrystalline copper varies as a function of step size. The initial step size used to capture EBSD map is 0.5µm. (b) GND density maps of 2% tensile strained copper sample with 0.5µm, 1µm, 1.5µm, 2µm step size used respectively.**

Variation of GND density as a function of step size is shown in Figure 3-13**(a)** in which the geometric mean of GND density is reduced from ~$10^{14}$ to ~$10^{13.5}$ $m^{-2}$. As the highest angular resolution has been used for this case (1x1 binned EBSP), the noise level for 0.5µm step size is estimated as 5.3 x $10^{11}$ $m^{-2}$ This value is significantly lower (190 times) than measured GND density value, thus we conclude that the obtained decrease in GND density with larger step size is a consequence of a change in separation between SSDs and GNDs due to the change in Burgers circuit size rather than from noise contribution.

In Figure 3-13(b), GND density maps are used to assess the GND density distribution with various step sizes. The dislocation cell structure is most apparent using 0.5μm step size. As step size is increased, it is more difficult to resolve the cell structure; however the 'hot' and 'cold' spots are still visible even using 1.5μm step size. When step size is increased to 2μm, the apparent GND based dislocation structure is changed significantly from the initial one.

Determining the appropriate step size for GND density analysis is difficult. Appropriate step size of the EBSD measurement enables resolution of dislocation structure. For example, if dislocation cells are formed in materials, the EBSD step size should be the same size (or smaller) as the dislocation cell diameter to enable an appropriate measurement of dislocation density. Using small step size allows us to obtain more detail on dislocation structure and may provide more information about the mechanisms involved. However, if the step size is too small, the measured GND density will be dominated by noise.

In practice, small step size will also constrain EBSD map size due to pattern capture and cross correlation processing times and therefore limit the statistical analysis. Yet using a large step size will reduce the noise level and enable scanning of larger regions but will result in many GNDs being counted as SSDs and therefore discrimination of key structures, such as dislocation cell walls, will be less clear. A compromise must be made in step size selection process as the appropriate step size depends on several factors such as the original dislocation density stored in samples, angular resolution, and the required size of EBSD maps.

When one adjusts these variables, the most important issue is that the measured GND density must be above noise floor. Here the higher sensitivity of the HR-EBSD method compared with Hough-transform based technique is a significant advantage and it is therefore more suitable for GND density distribution studies.

For the Hough based analysis, this necessitates low spatial resolution studies and often an underestimation of the underlying GND density distribution and limited spatial information. Recently, Field et al [144] conducted a study of step size effects on GND densities obtained from Hough-transform analysis of EBSD data. In their study of a single crystal Cu sample deformed to 10% compression in an initially single slip orientation, they used the 20-30μm dislocation cell size observed in their EBSD data as the criterion for step size selection. They concluded that GND density was determined as 15-30% of total dislocation density by comparing it with literature values for overall dislocation density obtained from TEM measurements. Adopting a similar approach, we estimate the cell size as 1μm - 2μm from the inspection of Figure 12**c**, which is in a good agreement with the same TEM data cited by Field et al (1.4μm at 25°C for 10% strain copper) [150]. At a 1.5μm step size, the mean GND density as determined in our EBSD measurements is $1.9 \times 10^{14}$ $m^{-2}$ which is very similar to the TEM measurement ($1.2 \times 10^{14} m^{-2)}$ [150].

## 3.3 Conclusion

1. Using a near prefect Si single crystal the angular resolution of EBSD analysis using the cross correlation method and the GND density measurement noise floor was assessed as a function of CCD camera binning level. We found that the measured lower bound GND density noise floor broadly agrees with the predicted GND density noise floor proposed by Wilkinson and Randman [27].
2. Again using a Si single crystal the relationship between GND density sensitivity and step size was studied. Results suggest an inverse proportional relationship. A relatively high angular resolution must be possessed if small step size is chosen to study dislocation structure as otherwise the high noise may dominate.
3. For an OFHC Cu polycrystal deformed to a moderate strain of 10% the GND density distributions were sufficiently high for there to be little degradation of the GND density map as binning was increased from 1x1 to 8x8. However, for more severe 16x16 binning data quality thresholds were often not meet so that an unacceptable fall in the solve rate was generated.
4. GND density maps of deformed Cu showed a clear loss of features as the step size was increased from 0.5μm to 2μm and above. This length range goes from below to above the dislocation cell size of ~1.5μm in the material. The arithmetic mean of GND density on a $\log_{10}$ scale drops relatively steadily as the step size is increased as an increasingly larger fraction of dislocations become SSDs.

# Chapter 4. Quantitative Analyses on GND Density Distributions and Evolution (I)

In order to assess deformation in large areas, in Chapter 3. , it has found that even cross correlation of highly binned patterns (e.g. 8x8) enables an adequate angular resolution (~0.1°) to reliably recover the stored GND densities in copper strained to 10% under tension. In comparison, there is no a similar study of Hough based approach, which has a reduced angular misorientation resolution (1-0.5°) and therefore an increased noise floor [151].

This chapter presents a systematic study of GND density of five samples deformed in tension to 0%, 6%, 10%, 22.5% and 40% plastic strain. In order to capture information concerning dislocation storage with respect to microstructure we have exploited the fact that 4x4 binned patterns provide adequate information for cross-correlation-based-EBSD measurements of stored dislocation content [152]. In Chapter 3. it was found that using step size of 0.5 μm and 4x4 binning level provides an excellent combination of spatial and angular resolution (~0.03°) and the associated GND density noise floor was estimated as ~$5.6 \times 10^{12}$ $m^{-2}$. 0.5 μm step size allows detailed dislocation structure to be revealed in copper where the dislocation cell size is ~1.5 μm [33] and 4x4 binning level enables statistically representative maps to be recovered with a reasonable collection time. This chapter presents a statistical study of GND density distribution, variation and accumulation with respect to plastic tensile deformation level and microstructure features in polycrystalline copper.

## 4.1 Experimental method

An oxygen free high conductivity pure (99.95%) polycrystalline copper foil (2.0mm thickness) with half hard temper was supplied by Goodfellow. Standard 'dog-bone' shape tensile testing specimens with gauge section of 25 mm x 6 mm x 1.5 mm were milled out according to the ASM standard [153]. Specimens were ground using a series of silicon carbide papers and then polished with 3μm diamond suspension. Chemical-mechanical polishing was carried out on a neoprene 'chem' cloth for 20 minutes using 1:1 diluted colloidal silica. A high quality finish was obtained by electropolishing the samples in an 85% $H_3PO_4$ solution with 1.2 voltages current running through for 10 minutes (using an AA battery). The polished samples were annealed in a vacuumed furnace for 15 minutes at 550°C (half the melting point) to reduce residual stress and cold work induced dislocation density prior to mechanical testing.

A series of tensile tests were conducted at a strain rate of $2 \times 10^{-6}$ $s^{-1}$. Four specimens were deformed in tension to average strains of 6%, 10%, 22.5% and 40% respectively (measured using Digital Image Correlation). EBSD analysis was conducted on a JEOL JSM-6500F with accelerating voltage at 20 kV and a probe current of ~17 nA. Areas of 500 μm x 500 μm were mapped on a square array with step size of 0.5μm. At each measurement point background subtracted EBSD pattern was recorded at 12 bit depth with a Digiview II using 4x4 hardware binning with OIM v5.3. No artificial addition of gain and black level were applied.

For each of these maps approximately one million patterns were saved to disk. This caused problems, as when more than ~300K individual files were stored into a single folder using NTFS storage of files became prohibitively slow, reducing the capture time from initial 16 patterns per second to ~2 patterns per second. This was likely caused by a problem with Microsoft Windows which stores and updates an index file for each new file added to the folder. We tackled this problem by designing a novel program using Matlab (http://www.mathworks.co.uk/) which simultaneously grabs images from the folder and stores them in one large HDF5 file (Hierarchical Data Format, http://www.hdfgroup.org). This format is designed for large dataset management and fast accessing speed. All EBSD patterns were saved in a HDF5 file at a frame rate of ~14 frames per second and subsequent access to the images within the HDF5 file was significantly faster (a similar speed up using a single file has been noted elsewhere [154]). ~12 months were spent on the HDF Matlab programming due to the difficulties of understanding the details of HDF command structures, optimising its performance and making it compatible with the HR-EBSD programme.

Each EBSD map contained 1 million points with 225 x225 pixel EBSPs and roughly 1,500 grains. They were collected in approximately twelve hours and were analysed subsequently by cross-correlation software in ~30 hours using a high performance computer that has six cores Intel(R) Core(TM) i7-3930k CPU @3.20GHz and 32 GB memory with thirty 64x64 pixel regions of interest (ROI) and only a ‘first pass’ of cross-correlation (i.e. no remapping was used [134], as for GND analysis in deformed metals as the strain gradients are significantly smaller than the lattice rotations and are therefore ignored).

Grains were demarked using OIM A v5.3 in which a grain boundary misorientation of 7 degrees and minimum grain size of 5 points were applied. Reference points were selected by searching for a point of high image quality (IQ) towards the grain interior.

For cross correlation, high and low band pass filters were applied to each ROI in the Fourier domain to remove the low frequency background intensity variation and high frequency noise. For each grain, pattern shifts were determined by measuring the thirty ROIs movement between the test patterns within each grain and the grain's reference pattern. These shifts were linked to lattice rotation by first determining eight of nine components of the displacement gradient tensor and then separating the anti-symmetric part [133]. (The ninth component is linked to hydrostatic dilation and contraction which does not results in any zone axes shifts, nor any lattice rotation.) In order to attain more statistical reliable measurement, robust fitting is used to find the best fit solution for more than four ROIs [133].Threshold values of PH>0.25 and MAE<0.01 rads were used.

# 4.2 Results

## 4.2.1GND density maps

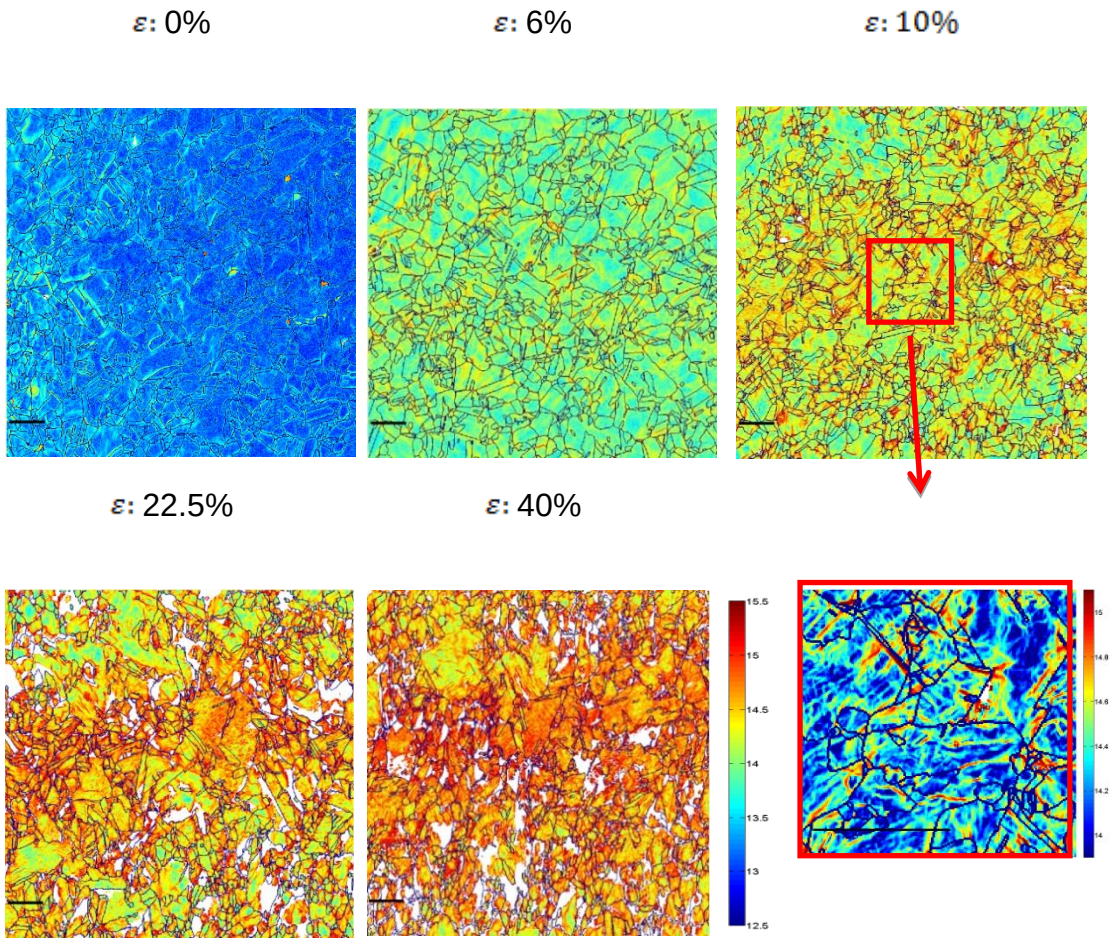



**Figure 4-1, 500 μm x 500 μm HR-EBSD recovered lower bound GND content maps of polycrystalline copper at tensile strain levels of 0%, 6%, 10%, 22.5% and 40% respectively. An enlarged 110 μm x 110 μm map is shown at right bottom corner with optimised colour bar. The scale bar is 50 μm and the used step size is 0.5 μm. The colour bar shows GND density in $\log_{10}$ scale of lines $m^{-2}$ and grain boundaries are indicated as the dark blue lines in the maps. White regions correspond to the rejected points by cross-correlation quality analysis with PH>0.2 and MAE< 0.01 rads.**

Figure 4-1 shows the 500 μm x 500 μm HR-EBSD derived lower bound estimates of stored GND density maps at progressively larger tensile strain. Approximately 1500 grains are included in each map such that statistically representative datasets are collected. Increasing plastic deformation results in an increase in the average stored GND content from ~$1x10^{13}$ to ~$1x10^{15}$. Furthermore, the evolution of dislocation patterning can be observed with the

formation of continuous sub-grain boundaries containing high dislocation content and the progressive accumulation of GND ‘hot’ and ‘cold’ spots. Such regions result in local increases in dislocation content as well as continued development of the dislocation patterning. It is clear that there are many long ‘string-like’ features of where dislocations continue from one grain boundary to another in a linear feature. Furthermore there are regions, typically near the grain interiors, which do not systematically seem to accumulate dislocations as fast as others.

It is worth noting that as the material deforms, the quality of the resultant diffraction patterns decreases due to the increasing presence of dislocations and strain gradients within the interaction volume. This result in a decreased number of points recovered for increasing strain through cross correlation due to the use of thresholds used to screen poor quality data. Provided that thresholds are not selected to be too strict then even with the decreased in solved points the evolution of dislocation patterning is evident. Filters of PH>0.2 and MAE< 0.01 rads result in a resolution of GND content from almost 100% in 0% and 6% deformed copper down to 83.2% and 78.9% in 22.5% and 40% strained maps. It is likely that the unresolved regions contain very high GND contents or the formation of new small grains.

The insert shown in Figure 4-1, has been selected to be similar in size to maps used in our previous studies [155], and to indicate the amount of information with both high spatial and dislocation content resolution contained within each of these maps. Colourmaps for this insert have been optimised to highlight the development of the dislocation structure and highlight both hot and cold spots. Dislocation cells are clearly evident at a lengthscale

commerserate with those observed previously in copper using TEM [33]. Furthermore, significant GNDs accumulations appear near some grain boundaries and triple junctions.

In the following sections detailed quantiative measurements of dislocation storage are made and linked to strain state and microstructural features which were determined from the datasets presented as maps in Figure 1.

### 4.2.2 Evolution of GND distribution with increasing strain

This section focusses on the overall evolution of the GND distributions without considering the location where dislocations are stored (ie volume averaged behavior).

Evolution of the GND density distribution can be observed in the histograms presented in Figure 4-2 (a). The general distribution of dislocations for all strain states has a very similar shape. However, the average dislocation content clearly increases with increasing plastic strain. Despite an increase in the mean the distribution for increasing strain, the shape of the $\log_{10}\rho_{gnd}$ histograms is similar at each imposed strain level. Histograms plotted on a linear GND density axis appear highly skew with a pronounced tail to the high density side of the peak.

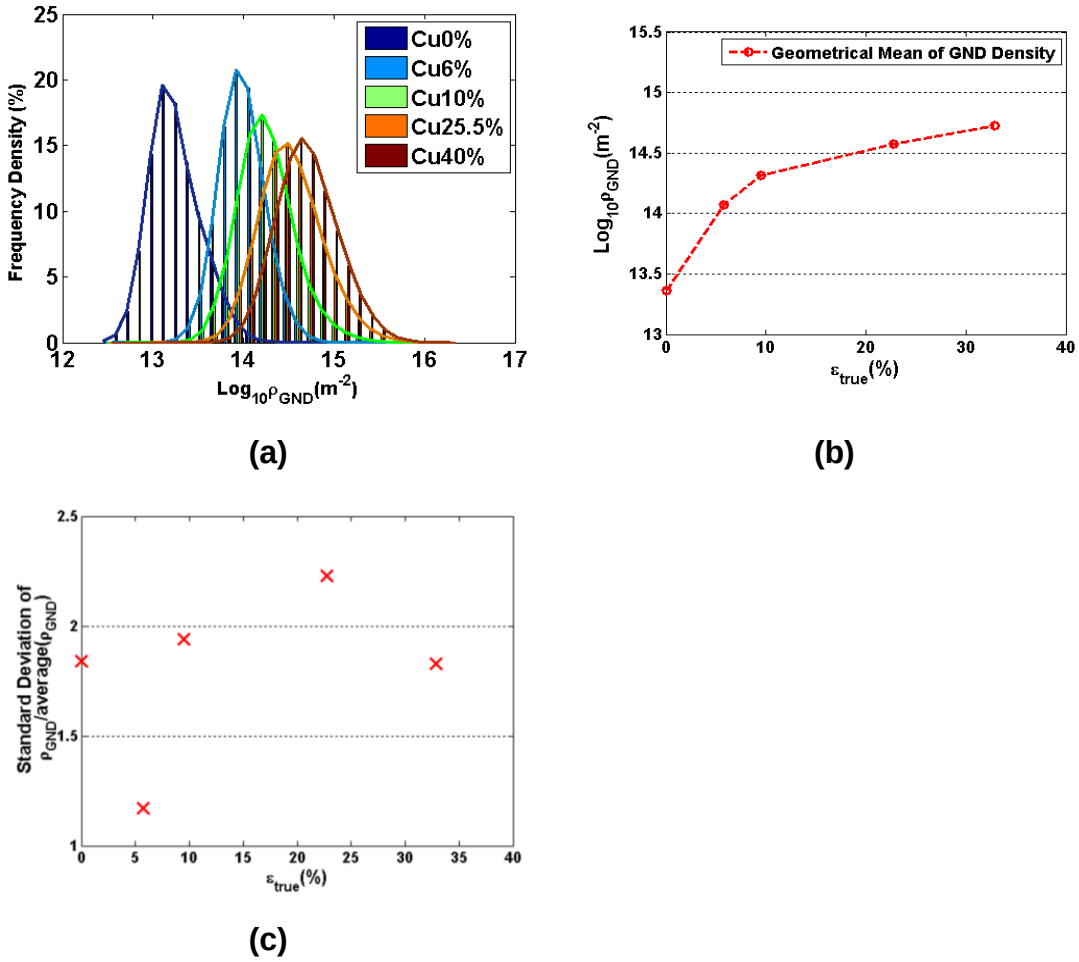



**Figure 4-2 shows the evolution of GND density distribution for increasing strains of 0%, 6%, 10%, 25.5% and 40% for copper samples: (a) histograms within a bin width of 0.127 in $\log_{10}$ scale; (b) shows the relation of the imposed true strain and the geometrical mean (red dash line) of map-overall GND density; (c) shows the standard deviation of the log of the normalised GND density distributions at the different strain levels.**

The functional form of the probability distributions have been assessed by first normalising the geometric mean value of the distribution to one and then fitting to various functions suggested in the literature [156]. In practice, the normalised distributions were binned between 0 and 5 with a bin width of 0.1. The fit of these normalised distributions to a Rayleigh function (equation 3) and a log-normal function (equation 4) were found to be reasonable (figure 3a & b). However, the probability plots in which data adhering to the functional form would appear as a straight line (figure 3c & d) show that the log-normal description is better. The Rayleigh distribution tends to fit well for the central region of the histogram but there are too few measured points with very high

and very low densities of stored dislocations with the departure at high densities being very marked (figure 3d). The fit for the log-normal function is generally good across the range of densities though the measured distribution falls slightly below the log-normal function at higher densities. Furthermore the gradients of the log-normal probability plots are similar for the datasets at different imposed strain levels indicating that the widths of the normalised distributions are similar (figure 3c).

Rayleigh Probability Distribution: $$y = f(x,b) = \frac{x}{b^2} e^{\left(\frac{-x^2}{2b^2}\right)}$$ Equation 4-1

Where $b$ is $\frac{1}{\sqrt{\pi/2}}$ for combining effects of rotations about two perpendicular axes.

Log-normal Probability Distribution: $$y = f(x,\mu,\sigma) = \frac{1}{x\sigma\sqrt{2\pi}} e^{\frac{-(ln[x]-ln[\mu])^2}{2\sigma^2}}$$ Equation 4-2

Where $\mu$ is the geometric mean (here normalised to unity –so that $ln\ \mu$ is 0) while $\sigma$ is the standard deviation of the associated distribution of $\log_e \rho_{gnd}$ distribution.

Assuming a log-normal form for the GND density distributions it is then sensible to report the geometric mean GND density which Figure 2 (b) shows as a function of imposed strain. In the annealed sample (0% strain) the average dislocation density was determined as 2.3 x $10^{13}$ $m^{-2}$. As the copper was strained, the stored dislocation content rapidly increased and then the rate of increase slowed for further deformation and seems to be saturating

toward a plateau having reached $5.3 \times 10^{14}$ $m^{-2}$ at 40% strain. Figure 2 (c) shows that when normalised by division by the geometric mean the width of the GND density distributions remains relatively constant across the entire range of strains studied. This is emphasised by the reasonably good agreement between the log-normal distribution and the experimental data at all imposed strains that is shown in figures 3 (a) and (b).

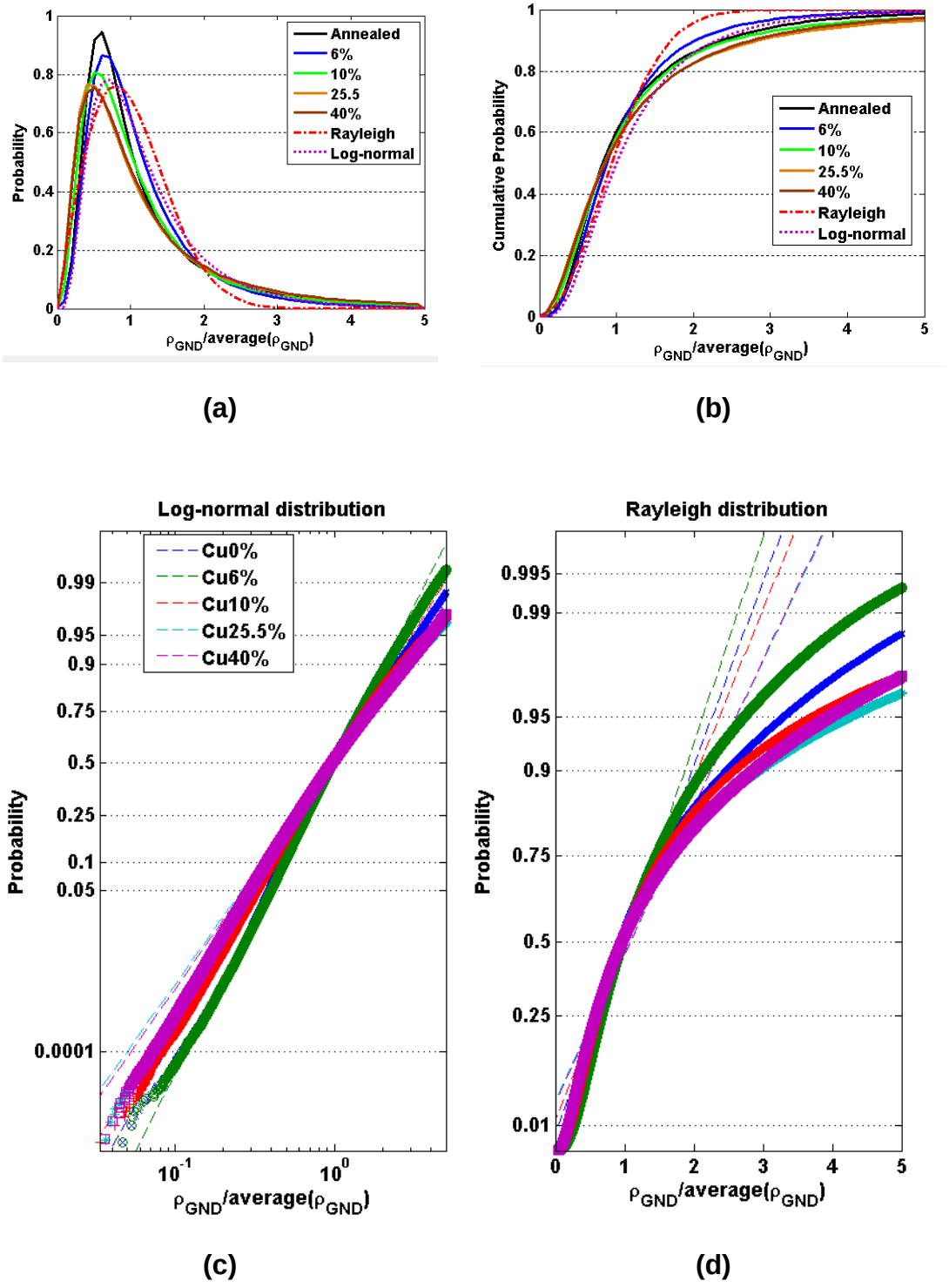



**Figure 4-3, normalised ($\frac{\rho_{gnd}}{average(\rho_{gnd})}$) GND density probability distribution and cumulative probability distribution of annealed, 6% and 10% strained samples are plotted in (a) and (b) respectively. The bin width used is 0.1 and average GND density values were determined using geometrical mean method. The probability for each bin was calculated by. Rayleigh and log-normal probability distribution functions were fitted in both (a) and (b). Probability plots comparing the normalised GND density distribution from 0%, 6%, 10% strained maps to the lognormal distribution and Rayleigh distribution are shown in (c) and (d).**

### 4.2.3 Relation between flow stress and average GND density

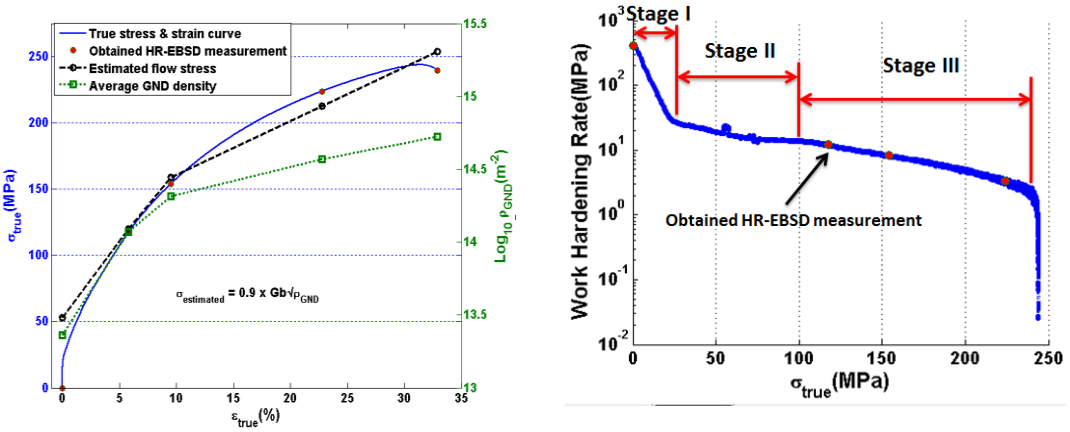
The true stress-strain curve measured using DIC technique at room temperature (blue solid line in Figure 4-4(a)) shows a characteristic parabolic relationship for polycrystal copper. Overlaid on this curve are the four strain levels for which samples were mapped for the EBSD maps shown in Figure 1, at nominal 6%, 10%, 22.5% and 40% tensile strain. Examining the work hardening curve (see Figure 4-4 (b)), 6%-22.5% samples are in stage III and 40% has been taken from a strain where necking has begun.

On Figure 4-4 (a), a second axis has been introduced which repeats the $\log_{10}(\rho_{GND})$ line shown in Figure 4-2(b) and a comparison of the forms of the $\varepsilon_{true}$ vs $\log_{10}(\rho_{GND})$ and $\sigma_{true}$ curves indicate that they are similar. Therefore Ashby hardening model which links dislocation content with flow stress has been used (Equation 4-3) to estimate the flow stress from GND related hardening and the result has been plotted on Figure 4-4 (a) as the black dashed line. A very good agreement is observed between the predicted flow stress-strain curve and the measured one.

$$\tau = \tau^0 + CG|\boldsymbol{b}|\sqrt{\rho_{GND}} \qquad \text{Equation 4-3}$$

Where $\tau^0$ consists of contributions from both frictional stress and long range internal stresses, it is assumed to be zero in our analysis (note that we have measured the presence of some GNDs, above the noise floor, for the 0% strain case). $C$ is a constant with a fitted value of 0.9 in this case. $G$ is the

elastic shear modulus with magnitude of 48GPa for pure copper and $b$ is the Burgers vector in copper with magnitude of 0.2553 nm.




**(a)** **(b)**

**Figure 4-4, (a) shows the true stress and true strain curve (measured with DIC) of polycrystalline copper. The embedded red dot points indicate the obtained EBSD and HR-EBSD measurements. The green line and right hand side green axis reveals the geometrical mean values of GND densities over each GND density map. The estimated flow stress is calculated according to Equation 4-3, (b) shows a plot of work hardening rate ($\frac{d\sigma_{true}}{d\varepsilon_{true}}$) as a function of $\sigma_{true}$.**

### 4.2.4GND density distribution with respect to grain boundaries

Qualitative assessment of the maps in Figure 4-1 indicates that GNDs accumulate near grain boundaries. Preliminary results on relatively smaller maps (110 μm x 110 μm) of annealed and deformed sample have already been reported by the authors [157] where the limited number of grains present prohibited proper statistical analysis. In this subsection, statistical analysis of relation between GND content and the Euclidean distance (defined within this thesis using Pythagoras' theorem to calculate the distance) to the nearest grain boundaries at various plastic deformation levels is presented.

Grain boundaries are identified as regions with >7° between neighbouring points using the Hough based EBSD measurements. From such 'skeleton' grain boundary maps, the Euclidian distance between each point and its nearest grain boundary (in the surface plane) is measured and recorded. This process is illustrated in Figure 4-5 and was repeated for every map recorded in this study.

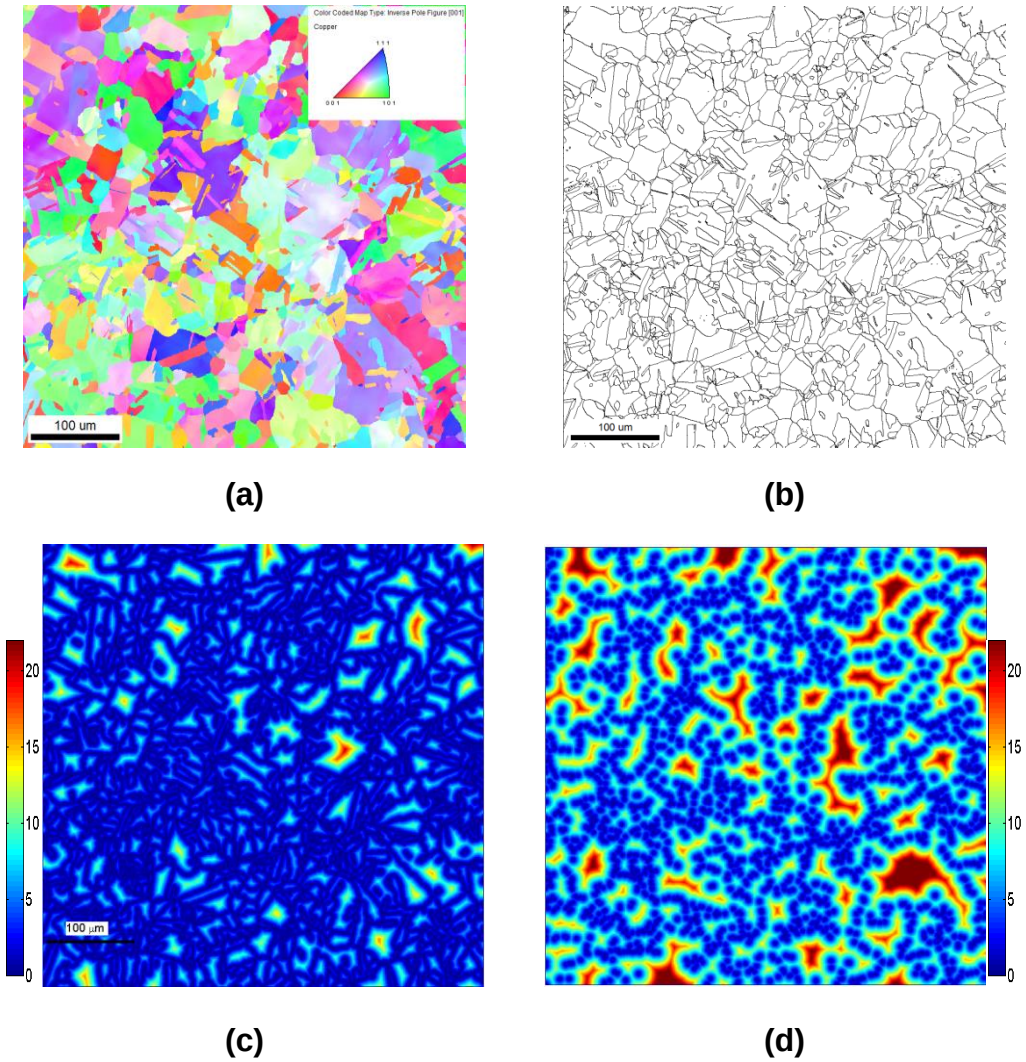



**Figure 4-5, (a) EBSD generated crystal orientation map for 6% strained copper sample with respect to the surface normal (no artificial post process was applied); (b) Grain boundary skeleton map generated from neighbouring points >7° apart; (c) Calculated minimum distance to grain boundaries map in which the Euclidean distance to the nearest grain boundary for each probed point were determined by calculating the distances of a point $(x, y)$ with respect to points along all grain boundaries (GBs) $(x_{GB}, y_{GB})$ ($D_{min} = min\sqrt{((x - x_{GB})^2 + (y - y_{GB})^2}$) and the minimum distance for each point was obtained. The colour bar indicates the distance to grain boundaries with unit of µm; (d)~6000 triple junction were identified and the Euclidean distance to the nearest triple junction for each probed point were determined by calculating the distances of a point $(x, y)$ with respect to points along all triple junctions (TJs) $(x_{TJ}, y_{TJ})$**

($D_{min} = min\sqrt{((x - x_{TJ})^2 + (y - y_{TJ})^2}$) and the minimum distance for each point was obtained. The colour bar indicates the distance to triple junction with a unit of μm.

Statistical analysis on the correlation between the distance to the nearest grain boundary and GND density is presented in Figure 4-6. All probed points are binned in both GND density (x-axis) and minimum distance to the grain boundary (y-axis). The intensity indicates the count in each bin. Furthermore, 10%, 50% and 90% centile values for the distance distribution at each GND density range were calculated and are plotted as green, red and blue dot lines respectively. Constructing such plot provides a complete picture of the correlation between GND density and distance and enables examination of distribution of GND density 'hot' spots and 'cold' spots as a function of minimum distance to grain boundaries.

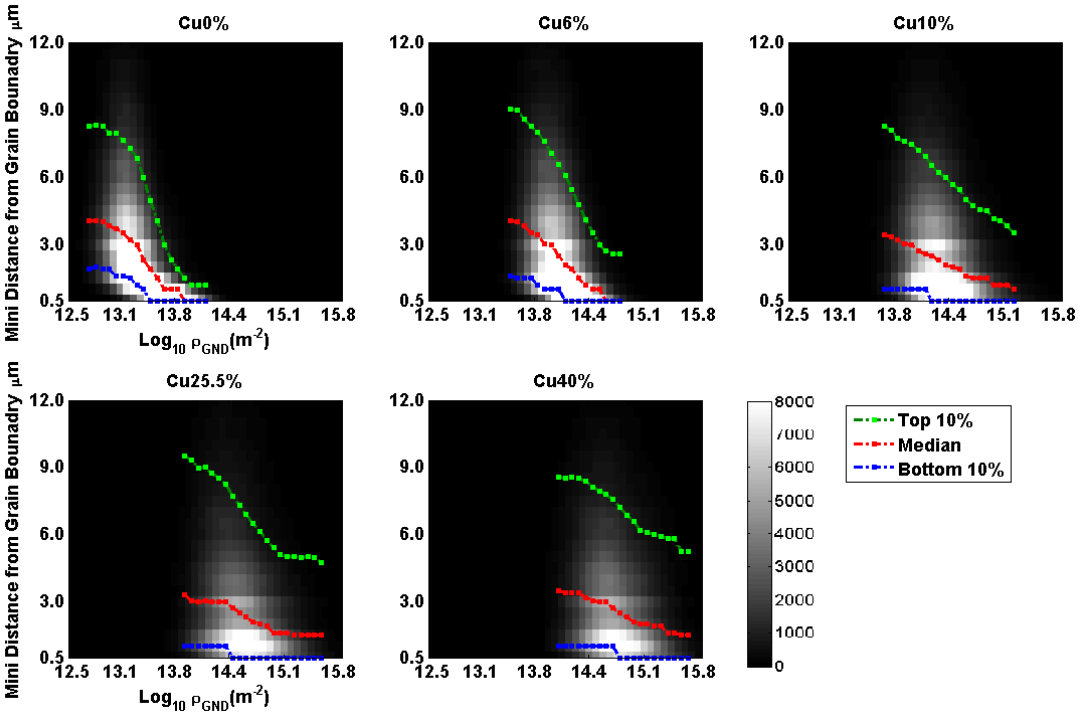



Figure 4-6: statistical evaluation of GND density with respect to distance from a (surface) grain boundary. GND density datasets were binned in both x and y axes with 40 bins and bin width of 0.095 in $\log_{10}$ scale for x axis and bin width of 0.5 μm for y axis. The x axis and y axis are adjusted accordingly to show the overall changes. Cross-correlation unresolved points, points on grain boundaries and grains on the edges of EBSD maps are not included in analysis.

For each map relatively high dislocation densities are closely linked to the grain boundary regions and relatively low dislocation density points spread in a significantly wider range. For increasing strain, the GND density distribution with respect to Euclidean distance to grain interfaces evolves in a distinct manner. The relatively high GND density points ("hot spots") initially scatter in a short distance range to grain interfaces (0-1 μm in annealed copper) and over half are directly adjacent to grain boundaries. This distribution is altered as the deformation level elevates. The distance range for the points with high dislocation density increases progressively to 3.0 μm in 6%, 4.0 μm in 10% and 5.0 μm in 25.5% and eventually reaches a plateau at 6.0 μm. Furthermore the median line also increases gradually from 0.5 μm in annealed sample to 1.5 μm in 40% sample. In contrast, some cold spots are moving closer to grain boundaries with the increasing in plastic strain state.

### 4.2.5GND density distribution with respect to triple junctions

With the obtained large HR-EBSD GND maps, in this subsection we present quantitative analysis on the correlation of GND density and triple junctions.

The GND content as a function of the distance to the nearest triple point has been analysed in Figure 4-7, using a similar approach to that used for grain boundaries in the previous section. It is clear that triple junctions are preferential GNDs accumulation sites for all strain states. It is notable that this general trend does not vary significantly between undeformed (0%) and deformed sample (6%, 10%, 22.5% and 40%), although as noted previously,

the average GND density increases with increasing deformation. Despite small fluctuation, hot spots points are constrained in a constant distance range from 0.5 μm to 11 μm and cold spots spread within a constant distance range from 3 μm to 16 μm. It is also observed that the cold spots do not migrate into any distance closer than 3 μm to a triple junction.

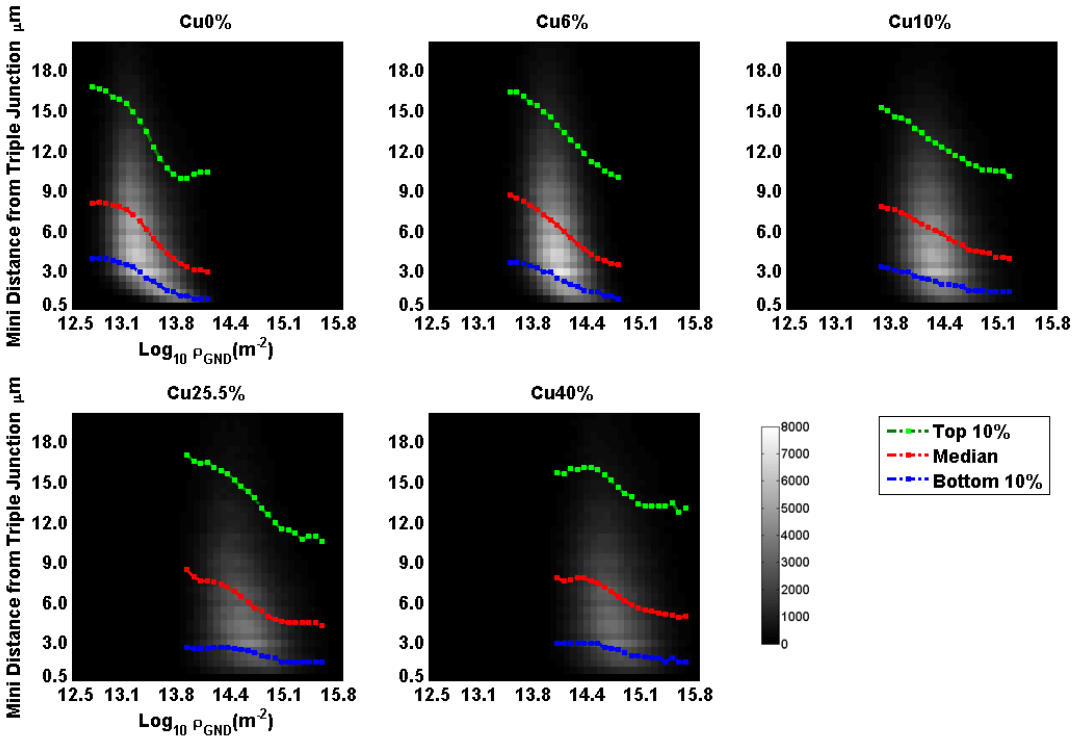



**Figure 4-7, quantitative analysis of Euclidean distance to the nearest triple junctions as a function GND density in 0%, 6%, 10%, 22.5% and 40% strained samples. ~6000 triple junctions were identified. The total of ~0.9 million estimated GND density points (exclude unresolved points, grains on maps' edges) were binned by GND density into 40 bins with a bin width of 0.045 in log10 scale, and binned by minimum distance to grain boundaries into 40 bins with a bin width of 0.5 μm. Grey colour scale represents the counts in each bin. The three lines are plots of 5%, 50%, 95% values respectively for each bin in x axis. Minimum number of 3000 courts in x axis bins is required to be plotted.**

### 4.2.6Grain averaged GND density with respect to grain size

In the previous subsections, we studied that the relation between GND density and minimum distance to grain boundaries without paying specific attention to any grain size effect. In this subsection we explore the grain size effect on the GND density in annealed and deformed samples.

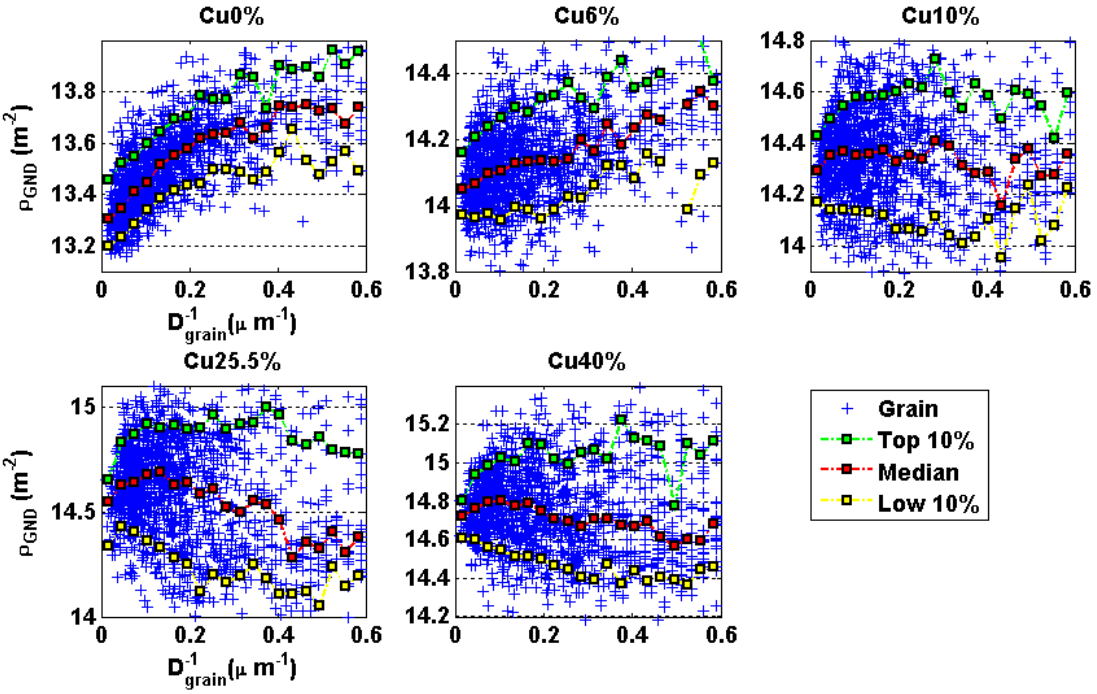



**Figure 4-8, GND density as a function of inverse grain diameters in the annealed, 6% 10%, 22.5% and 40% strained samples. Grain shapes were assumed to be circular, the grain radius was determined by counting the total area of composed pixels (50 μm x 50 μm) and hence $(D) = 2 \times \sqrt{Area/\pi}$. Grains along the edges of EBSD maps were excluded from analysis. For each map, the dataset with range of 0 - 0.6 μm was grouped into 15 bins and data in each bin was sorted in descent order. The points at 10%, 50% and 90% of total points in each bin were identified and plotted as green, red and yellow dot lines which are used to describe the distribution and trends of datasets. The minimum 20 grains must contain within a bin in order to reliably find 10%, 50% and 90% points.**

We start by examining the GND content present at the start of the tensile test due to structures present as a result of prior rolling and annealing treatments. Figure 4-8 Cu 0% plots the grain averaged GND density as a function of the

inverse of the grain diameter, and reveals a strong and approximately linear correlation between the two parameters with higher GND densities tending to be present in the smaller grains. The fluctuation between 0.3 and 0.5 $\mu m^{-1}$ is likely caused by relatively small sampled population. In this undeformed sample, the GND density tends to concentrates near grain boundaries as seen in Figure 4-6 Cu 0%. The presence of a near grain boundary region with raised GND density would result in small grains tending to have higher average GND density than large grains. Indeed a one over grain diameter variation of grain averaged GND density would result from the ratio of grain boundary area and grain volume.

In the early stages of deformation (0-6% strain) Figure 4-8 Cu 6% reveals that the inverse relationship between grain averaged GND density and grain size is preserved. However, as the strain level is increased to 10% and beyond, this relationship is no longer observed and there is no strong correlation between grain averaged GND density and grain size.

## 4.3 Discussion

HR-EBSD with suitable spatial and angular resolution provides a new means to quantitatively study dislocation evolution in plastically deformed polycrystals. The following aspects were investigated statistically from the large dislocation density maps shown in Figure 4-1: the overall GND density and it evolution with strain, the functional form of the overall GND density distribution, the local changes in GND density near grain boundaries and triple junctions, and the influence of grain size on grain averaged GND density.

There is a good agreement in Figure 4-4(a) between the measured true stress and predictions from Ashby hardening theory calculation. The best fit value of 0.9 for the parameter C in equation 5 implies that GND density as measured with a 0.5 μm step size is a large fraction of the total dislocation density. Here the step size has been set to somewhat below the size of the expected dislocation cell size. An inappropriately large step size will of course reduce the GND density [152]. Ashby's GND model [1] indicates that the strain gradients and therefore GND density should be increasing with the imposed strain. Although we do find a reasonable linear fit between the average GND density and imposed strain in support of Ashby's model the GND densities are much higher than predicted. The higher GND densities are, of course, because Ashby's model is formulated on the basis strain gradients over lengths spanning entire grains while our data is based on a substantially smaller length scale of 0.5 μm and so a larger fraction of the total dislocation density are considered GNDs.

Furthermore comparing with the TEM results [33] in which the total dislocation density (GNDs and SSDs) was measured and a similar equation (Equation 2-8) was used to verify the relationship between the total dislocation density and flow stress, it seems that the obtained GND density can represent the total dislocation density in polycrystal copper samples and can be used as a single parameter to indicate the level of deformation.

We found that the overall GND density distribution was well described by a log-normal function at each strain level. This is consistent with the work of Kamaya et al [125] which showed log-normal distributions for intra-granular misorientations measured by EBSD in deformed stainless steel. Similar skew distributions have been found in TEM measurements of cell to cell misorientations in deformed metals [158]. As the measured misorientation angles effectively can be linked to dislocation density, a comparison can be made between these prior TEM and EBSD measurements and the GND densities presented here. Similar distributions were established theoretically by Pantleon and Hansen [156] who showed that normal distributions of rotations about two orthogonal axes from two independent sets of dislocations generate a Rayleigh distribution. Of course here we have more than two dislocation types and their [156] corresponding rotation axes are not orthogonal and nor are the populations of the different GND types independent. Pantleon and Hanson [156] noted some departures from a Rayleigh distribution but did not present fits to log-normal distributions preferring instead to suggest the use of superposition of multiple Rayleigh functions. Although the fit of our data to a Rayleigh distribution was reasonable it was also very evident that the log-normal distribution was a

considerably better fit. Following Hughes et al [158] we also see that a simple scaling rule can be used to reduce the data at different strain levels to a single master curve (figure 3a), although we differ from Hughes et al in finding that a log-normal distribution is a good descriptor of the data.

Dislocation density variations in deformed metals are known to be highly heterogeneous. In polycrystals Ashby's theory [1] proposed that the abrupt changes in slip system geometry at grain boundaries lead to the accumulation of high GND densities as dislocations were required to satisfy compatibility conditions and prevent formation of voids of grain overlap. The statistical analysis presented in Figure 4-6 demonstrates that the grain boundary regions are the most likely places to find high GND densities within the polycrystals in good agreement with Ashby's theory. In the grain interiors (i.e. high Euclidian distances) the GND densities tended to be somewhat lower.

For the annealed sample the relatively low GND density points are shown to be distributed over almost the entire range of Euclidian distances. This broad spread in position of lower density features does not change markedly as the plastic strain level is increased even though the GND density is itself increasing in these regions. Only at the very lowest GND density (i.e. 10% line) is there evidence of a small decrease in distance from the grain boundaries.

The transition from lower GND density in the grain interiors to higher densities near the grain boundaries is most marked for the annealed sample in which the high GND density regions are mostly restricted to a narrow band close to the grain boundaries. When the deformation is increased to 6% strain the

high GND densities still tend to located close to the grain boundaries but the range of likely positions extends further from the grain boundaries. This trend is continued over the higher deformation levels for which the high GND density regions extend to greater distances from the grain boundaries. The transition from higher densities near the boundaries to lower densities in the grain interiors becomes more diffuse as the imposed deformation is increased. Overall the tendency is for higher GND density regions to first form near the grain boundaries and then to widen into the grain interior as deformation proceeds. Kamaya [159] has seen a similar localisation of larger KAM values near grain boundaries with similar distributions obtained for annealed and deformed samples.

The role of triple junctions as preferential sites for GND density accumulation has been previously indicated by increased micro-hardness levels [160], increased misorientations in Hough-based EBSD line scans [161] and increased dislocation density observed in TEM [162]. Consequently triple junctions have been often observed as preferential nucleation sites for dynamic recrystallization [163]. Some preliminary correlation analysis between GND density and triple junctions has been conducted by the present authors [155]. The larger data sets generated here for randomly selected regions of the samples allows for more quantitative unbiased analysis.

The observed relatively large distribution range for hot spots indicates triple junctions are not the sole sites for GND accumulation. Other factors such as grain boundaries must be taken into account as well. However, unlike the tendency for GND density accumulation near grain boundaries which was shown to reduce at large deformation level (>6%), for triple junctions the trend

continues over the entire range of imposed deformation levels. This is supported by the observation that relatively low GND density points do not appear anywhere nearer than 3 μm to triple junctions. In other words, the vicinity areas of triple junctions are occupied by high GND density at all imposed macroscopic strain levels.

As the dislocation density is higher close to the grain boundaries it follows that the GND density should be higher on average for the smaller grains. Figure 4-8 shows that this is the case at the lower deformation levels, though the trend is not apparent for imposed plastic strains of 10% or higher. Littlewood et al have shown a similar trend that the grain averaged GND density was higher for smaller grains in Ti-6Al-4V samples deformed to moderate strain in tension or fatigue [141, 164]. In the current study a relatively well defined shell of high GND density was found close to the grain boundaries at low strain levels. As the grain area on the two dimensional section varies as $D^2$ (D is the grain diameter) while the area of the high GND density near grain boundary region varies as D this leads to the average GND density varying as $D^{-1}$. Of course the 3 dimensional case also leads to a $D^{-1}$ dependence for the dislocation density as was suggested by Li in one of the early explanations of the Hall-Petch effect [165]. Li proposed that dislocations were generated by the formation of grain boundary ledges requiring the punching out of dislocation into the grains. If the ledge density on the grain boundaries is taken as constant then the $D^{-1}$ dependence of grain averaged dislocation density results. Coupling the grain size dependence with a Ashby model (equation 5) results in the yield stress varying as $D^{-½}$ in accord with the Hall-Petch relationship. The data in figures 8 and 9 suggests that such a

model could be supported for low strains but not for higher strains (10% tension and above). The boundary ledge densities quoted in the literature are in the range 0.02 to 0.2 $b^{-1}$ [165, 166] which corresponds to expected dislocation densities in the range 0.6 to 6 $x10^{13}$ $m^{-2}$. The average GND density measured in the annealed sample was $2.5x10^{13}$ $m^{-2}$ which is towards the middle of the expected range.

## 4.4 Conclusions

Using HR-EBSD, lower bound GND density maps for large areas (500 x 500 $\mu m^2$) containing many (1500+) grains have been generated. This has been undertaken by using fast pattern capture with 4x4 pattern binning. At this binning level, it is likely that the GND measurement has a noise floor of ~$5.6x10^{12}$ $m^{-2}$ which is significantly less than the average GND density observed within these maps. This analysis has been repeated for 0%, 6%, 10%, 22.5% and 40% strain levels. Data presented in map form in Figure 4-1 has been statistically analysed with respect to bulk observations, including the observation of Ashby-like hardening, as well as microstructural correlations.

The following conclusions may be drawn:

1. The average GND density increases with increasing plastic deformation. The predicted flow stress using Ashby's theory is in a good agreement with experimental measurement.
2. The general GND density distributions can be more accurately described by a log-normal probability distribution function rather than a Rayleigh distribution function. There is a small divergence of measured GND density distribution from log-normal function at high density. Dividing by the geometric mean GND density to normalise the distributions reduces the data at all imposed strain levels to a single master curve.
3. High GND density is generally found close to grain boundaries while the relatively low GND density regions are more spread from the grain

boundaries into the interior of grains. This observation is most marked for the annealed and low strain samples, while at higher strains the higher GND density points spread over a greater distance from the boundaries.

4. Triple junctions are identified as key microstructural features at which high GND densities accumulate so as to accommodate the inhomogeneous plastic deformation. This trend persists to higher strain levels.
5. Grain size analysis proved that at low and moderate deformation levels, grain averaged GND density is inversely proportional to grain size due to grain boundary hardening effect. This observation combined with a Ashby hardening model supports the Hall-Petch relation. At higher deformation levels the $D^{-1}$ dependency of the GND density is removed.

# Chapter 5. Quantitative Analyses on GND Density Distribution and Evolution (II)

This chapter presents texture development in the tensile deformed polycrystalline copper samples and extends quantitative assessment of HR-EBSD recovered dislocation distributions. This focuses on the evolution of dislocation patterning with respect to Taylor factor, Schmid factor, grain boundary disorientation and grain boundary inclination to the loading axis.

The evolution of GND density has been studied using HR-EBSD with different levels of plastic strain. In Chapter 4. it was found that in annealed sample dislocations accumulated primarily adjacent to grain boundaries. This tendency became less marked with increasing plastic strain. As shown in Figure 4-1, different grain boundaries showed distinct characters to interact with dislocations. In this chapter, two critical grain boundary properties are identified namely the grain boundary inclination angles with regard to loading axis and grain boundary disorientation angles between two neighbouring grains. The dislocation- grain boundary analysis is furthered to study if these grain boundary characters influence dislocations behaviours.

In microplasticity theories, due to the anisotropic nature of crystals, various sets of dislocation slip systems are activated during plastic deformation depending on their orientations. In Schmid theory, this orientation dependence was described by a Schmid factor [46] where by it is assumed that the same external stress is imposed on each grain. The Schmid factor resolves the externally applied stress onto each slip system and the

maximum value for a particular slip system indicates yield, assuming single crystal-like deformation.

Various authors using TEM, X-ray diffraction line broadening and microhardness techniques have observed distinctive characters of dislocation structure [41, 42], stored energy [43] and mechanical properties [44] in deformed polycrystals as a function lattice orientation. Merriman and Field have recently reported a dependence of GND density estimated from conventional Hough-based EBSD upon orientation of the crystalline [45]. In their investigation, four commercial purity aluminium (AL1050) samples containing ~300 grains were compressed at room temperature in a channel die to 5% 10% 15% and 20% strain. The range of measured misorientation angle was 0.5° to 5° and 2 μm step size was used to scan 570 μm x 1707 μm maps. Their results indicated that Taylor factor gave a good prediction on grain average dislocation density and that {011} grains have the highest dislocation content, although insufficient numbers of grains were sampled in this study.

The second and third aims of this chapter were to investigate further the correlation reported by Merriman and Field with more representative maps (contain ~1500 grains versus ~300 grains). HR-EBSD maps are reported with higher angular resolution (0.003° versus 0.5°) and better spatial resolution (0.5μm versus 2 μm); to compare Taylor factor to Schmid factor with dislocation density evolution.

# 5.1 Analytical method

## 5.1.1 Taylor factor

In OIM analysis software, Taylor factors for the determined orientation were calculated by inputting the family of possible slip systems ({111}, <1-10>) for FCC crystals and the deformation gradient (or displacement tensor) for case like uniaxial tension in rolling direction is: $\begin{pmatrix} 1 & 0 & 0 \\ 0 & -0.5 & 0 \\ 0 & 0 & -0.5 \end{pmatrix}$. In OIM software Rolling Direction (RD), Transverse Direction (TD) and Normal Directions (ND) are defined in Figure 5-1.

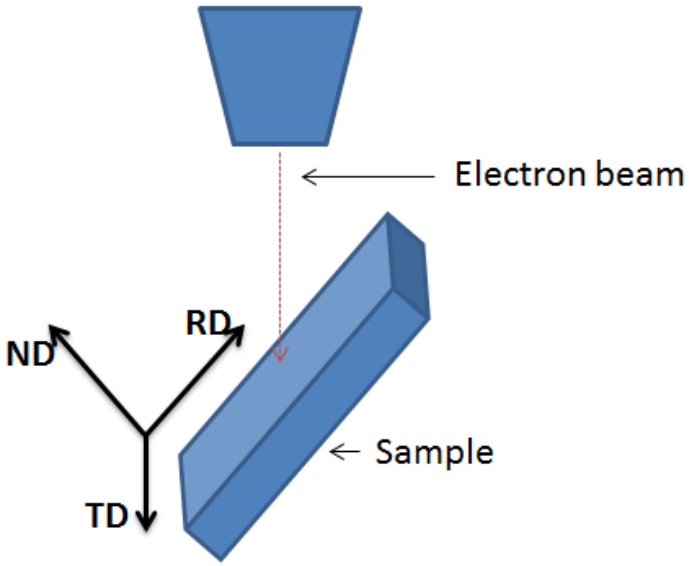



**Figure 5-1, showing the three principle reference axes in OIM analysis software.**

In order to satisfy the assumptions that the uniform strain in every individual crystal with arbitrary shape change, Taylor's analysis finds the set of slip systems with the least amount of energy expenditure (plastic work). However, as in case of FCC crystal, there are 24 possible slip systems which render the problem underdetermined. To find a physical based answer, an optimisation

scheme was employed to minimise the plastic work. Bishop and Hill further refined Taylor's theory by calculating the available appropriate stress states to realise simultaneous activation for sets of slip systems. Using the principle of virtual, Bishop and Hill obtained following expression:

$$\delta W = \sum_s \gamma^{(s)} \tau_c^{(s)} = \tau_c \sum_s \gamma^{(s)} = \sigma\varepsilon \quad (\gamma^{(s)} \geq 0)$$

Equation 5-1

Where $\delta W$ indicates the minimum plastic work for slip $\gamma^{(s)}$ on one or more sets of five slip systems $s$ and $\tau_c$ denotes the critical resolved shear stress on slip system and is assumed to be the same for all slip systems. $\varepsilon$ is the infinitesimal uniaxial strain and $\sigma$ is the uniaxial stress.

The Taylor factor $M$ is defined as

$$M = \sum_s \frac{\gamma^s}{\varepsilon} = \frac{\sigma}{\tau_c} \quad (\gamma^{(s)} \geq 0)$$

Equation 5-2

$M$ is related to crystal orientation as well as the imposed deformation gradient.

Large Taylor factor value indicates relatively large amount of energy is required for more slip to take place. We can thus denote high Taylor factor grains as 'hard' grains. For grains with lower value of Taylor factors,

less/more efficient slip occurs to achieve required strain level. We denote these grains as ‘soft’ grains.

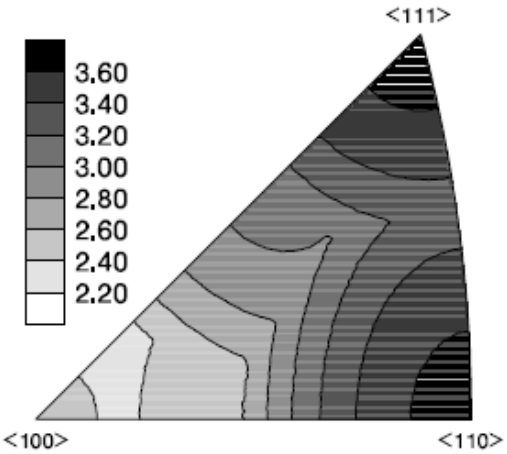



Figure 5-2, the calculated Taylor factor as a function of the orientation for copper [167]

The calculated Taylor factor as a function of the orientation is shown in a unit stereographic triangle in Figure 5-3.

### 5.1.2 Schmid factor

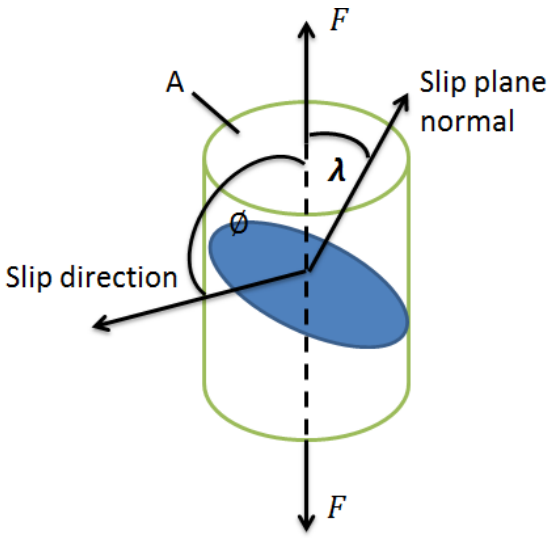



Figure 5-4, schematic diagram showing the geometrical relationship between tensile loading direction, slip plane and slip direction in crystalline materials.

Differing to Taylor's model, in the Schmid model it is assumed that uniform stress is imposed on each individual grain. Plastic strain is solely accomplished by primary slip system. For a given stress state, all slip systems were generally orientated differently from the loading axis. This resulted in various magnitudes of resolved shear stress $\gamma_{rss}$ for each slip system. A particular slip system is activated when $\gamma_{rss}$ exceeds critical resolved shear stress ($\gamma_{crss}$ ) of the material. For an imposed tensile stress $\sigma_{RD}$ along RN, as shown in Figure 5-4 the geometrical relation between $\gamma_{crss}$ and $\sigma_{RD}$ can be expressed as

$$\gamma_{crss} = \frac{F_{slip}}{A_{slip}} = \frac{F\cos\lambda}{A/\cos\varphi} = \sigma_{RD}\cos\varphi\cos\lambda \qquad \text{Equation 5-3}$$

The geometrical factor $\cos\varphi\cos\gamma$ is defined as Schmid factor.

In OIM analysis software, similar to Taylor factors the Schmid factors are calculated by first converting stress tensor to a set of principle stresses. For uniaxial tension on RD the stress states are[1 0 0,0 0 0,0 0 0]. It should be noted that in the Schmid model the stress states are considerably simplified as only a single principal stress $\sigma_{RD}$ is taken into account. The angle $\lambda$ and $\emptyset$ between loading direction, slip plane and direction for all 24 possible slip systems (FCC <110> {111}) can be determined within the crystal lattice whose orientations have already measured by OIM. Among all 24 possible

slip systems, the maximum value was selected as the Schmid factor for that particular orientation. Unlike Taylor's model in which at least five independent slip systems are simultaneously active, Schmid analysis only considers the easiness to initiate the first slip system. Grains with small Schmid factors indicate that relatively large stress is required to activate the primary slip system. They can be hence denoted as 'hard' grains. Therefore grains with high Schmid factors mean relatively low normal stress required to initiate primary slip system and can be denoted as 'soft' grains.

### 5.1.3 Grain boundary inclination angle with regard to loading axis

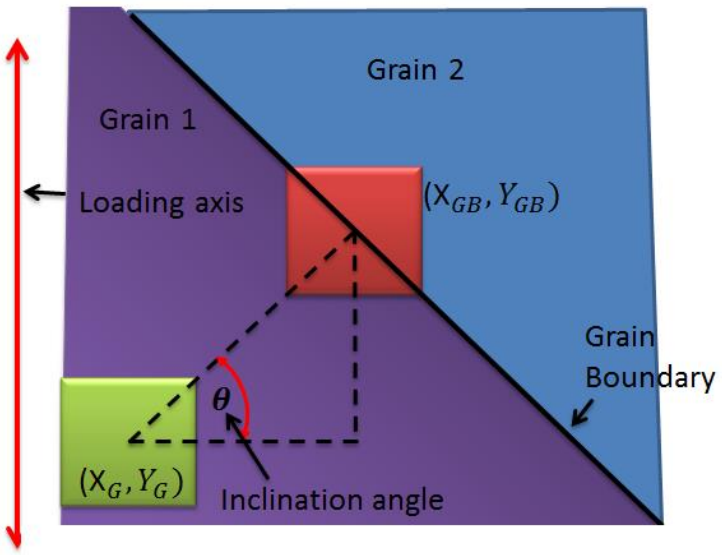



**Figure 5-5, a schematic diagram illustrating the associated grain boundary inclination angle of a point ($X_G$, $Y_G$) in a grain to the nearest grain boundary point ($X_{GB}$,$Y_{GB}$).**

It is of interest to study the different dislocation response when grains are loaded in parallel (inclination angle 0 degree) and series (inclination angle 90 degrees). The grain boundary inclination angles to external loading axis are determined in an author designed Matlab code. It should be noted that the inclination angle in this project is a 2D morphological parameter between

grain boundary lines and loading axis (see Figure 5-5) rather than the 3D grain boundary parameter commonly used for characterising the inclination between two grains.

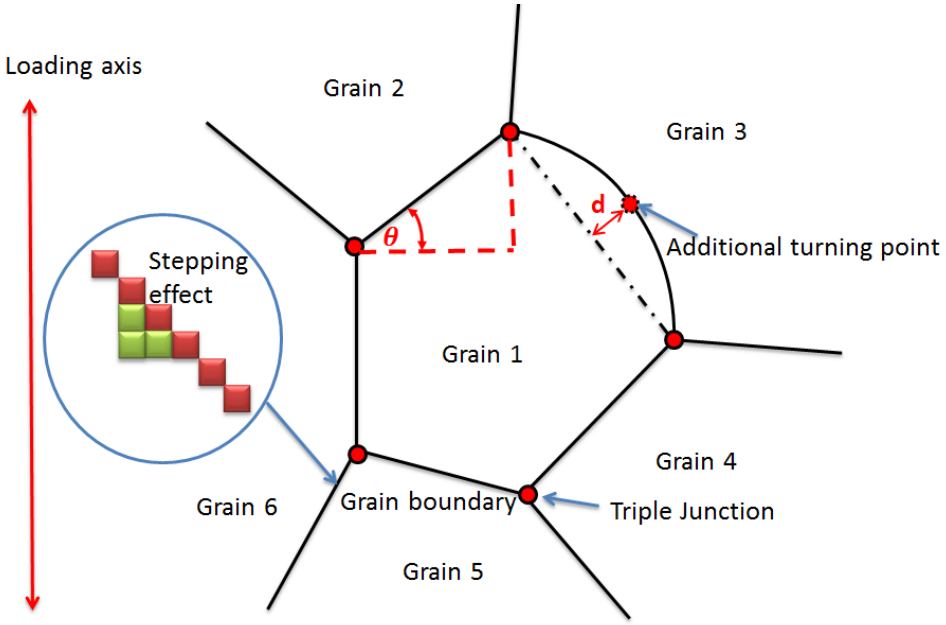


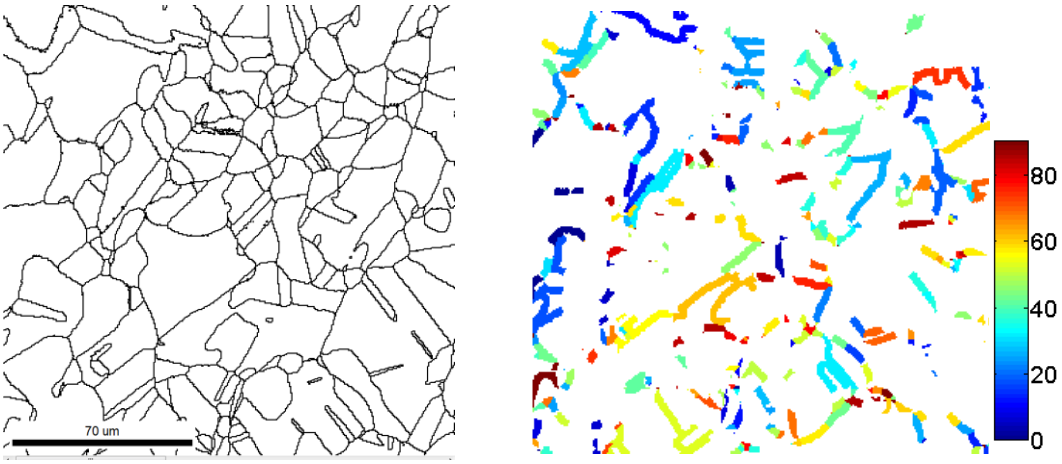

**Figure 5-6, a diagram illustrating analytical method to determine grain boundary inclination angles.**

Digital image aliasing effect due to the fact that grain boundary lines are sampled on square pixels. This severely prohibits calculation of accurate inclination angle for points near grain boundary as illustrated in the blue circle zone in Figure 5-6. The inclination angles for points next to grain boundaries can only be determined as 0 degree, 45 degrees and 90 degrees.

To tackle this problem, grain boundaries were divided into a number of line segments by triple junctions (see Figure 5-6). The inclination angle $\theta$ was thus calculated for each segment by finding its gradient as shown between grain 1 and grain 2. The obtained inclination angle was assigned to constituted grain boundary points. However, in practice grain boundaries are

rarely straight lines between two triple junctions. Curved boundaries as shown between grain 1 and grain 3 in Figure 5-6 are more commonly observed. To further improve the accuracy, a distance $d$ from the middle point of each line segment to its nearest grain boundary was calculated. To balance the accurate description and the complex grain morphology $d$ was chosen to be 1 μm. Thus if this distance was larger than 1 μm, this grain boundary point would have become an additional turning or joining point. This refinement was run three iterations to ensure relatively accurate inclination angles were obtained. An example of determined inclination angle using this approach is shown in Figure 5-7. Note that this grain boundary reconstruction approach is available in OIM software, but for hexagonal gridded maps only [168].

It should be noted that in practice for polycrystalline copper the morphology of copper grains is rather complex (see Figure 5-10) especially in the presence of the convex and concave boundaries such that not all of the points on grain boundaries were able to be included for further analysis.



**(a)** **(b)**

**Figure 5-7, (a) grain boundary skeleton map of the annealed sample. (b) The determined grain boundary inclination angles for each grain boundary.**

### 5.1.4 Grain boundary disorientation angle

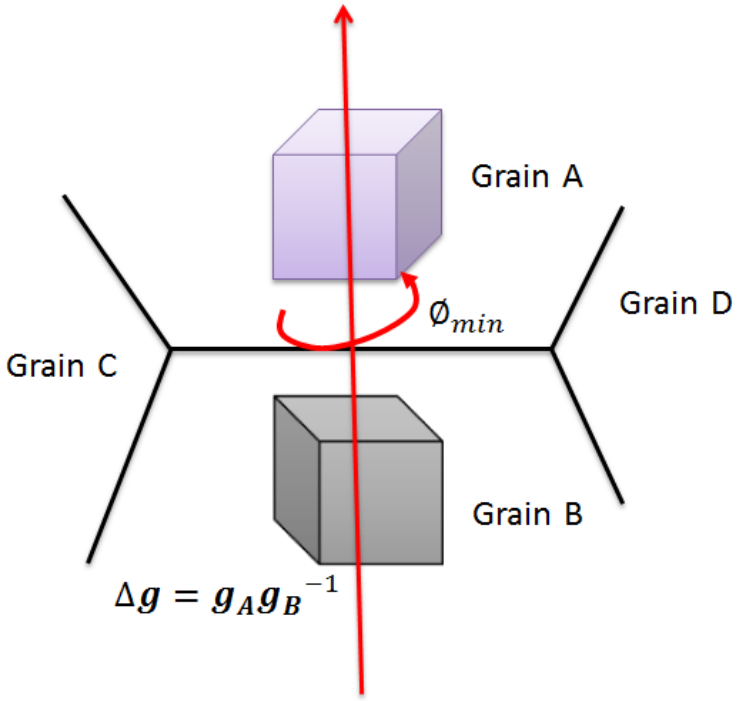



**Figure 5-8, schematic diagram to show disorientation between two grains.**

As seen in Figure 5-8, the disorientation between two connected grains is defined as the smallest physically possible rotation required to rotate one set of grain axes into coincidence with the neighbouring grain (based on a fixed reference frame) [169]. As any crystal orientation may be described by three sequential rotations through Euler angles [170, 171] in a fixed reference frame, if we specify the reference axes using the RD, TD and ND in OIM analysis software, the alignments of crystal axes with reference axes can be accomplished by performing following three rotations:

$$\text{Rotation } 1 = \boldsymbol{g_1} = \varphi_1 \qquad along\ RD\ axis$$

Equation 5-4

$$\text{Rotation } 2 = \boldsymbol{g_2} = \emptyset \qquad along\ TD\ axis$$

Equation 5-5

$$\text{Rotation } 1 = \boldsymbol{g_1} = \varphi_2 \qquad along\ ND\ axis$$

Equation 5-6

These three rotations can be expressed in matrix form

$$\boldsymbol{g_1} = \begin{bmatrix} \cos\varphi_1 & \sin\varphi_1 & 0 \\ -\sin\varphi_1 & \cos\varphi_1 & 0 \\ 0 & 0 & 1 \end{bmatrix}$$

Equation 5-7

$$\boldsymbol{g_2} = \begin{bmatrix} 1 & 0 & 0 \\ 0 & \cos\emptyset & \sin\emptyset \\ 0 & -\sin\emptyset & \cos\emptyset \end{bmatrix}$$

Equation 5-8

$$\boldsymbol{g_3} = \begin{bmatrix} \cos\varphi_2 & \sin\varphi_2 & 0 \\ -\sin\varphi_2 & \cos\varphi_2 & 0 \\ 0 & 0 & 1 \end{bmatrix}$$

Equation 5-9

The grain orientation matrix $\boldsymbol{g}$ can be obtained by rotation matrix multiplication:

$$\boldsymbol{g} = \boldsymbol{g_3 g_2 g_1} \qquad \text{Equation 5-10}$$

By substituting Equation 5-7, Equation 5-8 and Equation 5-9 into Equation 5-10, the full orientation matrix $\boldsymbol{g}$ can be expressed as:

$$\boldsymbol{g} = \begin{bmatrix} \cos\varphi_1 \cos\varphi_2 - \sin\varphi_1 \sin\varphi_2 \cos\emptyset & \sin\varphi_1 \sin\emptyset \\ -\cos\varphi_1 \sin\varphi_2 - \sin\varphi_1 \cos\varphi_2 \cos\emptyset & \cos\varphi_2 \sin\emptyset \\ \sin\varphi_1 \sin\emptyset & \cos\emptyset \end{bmatrix} \qquad \text{Equation 5-11}$$

$$\begin{bmatrix} \sin\varphi_1 \cos\varphi_2 + \cos\varphi_1 \sin\varphi_2 \cos\emptyset & \sin\varphi_2 \sin\emptyset \\ -\sin\varphi_1 \sin\varphi_2 + \cos\varphi_1 \cos\varphi_2 \cos\emptyset & \cos\varphi_2 \sin\emptyset \\ -\cos\varphi_1 \sin\emptyset & \cos\emptyset \end{bmatrix}$$

As illustrated in Figure 5-8, the net rotation (misorientation) between two connected grains can be defined as

$$\Delta\boldsymbol{g} = \boldsymbol{g_A g_B}^{-1} \qquad \text{Equation 5-12}$$

For the cubic system there are 24 symmetries which mean that misorientation can be described in 24 equivalent ways. The symmetry related solutions are generated by pre-multiply original orientation with each symmetry matrix $\boldsymbol{T_i}$.

$$\Delta \boldsymbol{g}' = \boldsymbol{T_i} \Delta \boldsymbol{g} \qquad \text{Equation 5-13}$$

Where i = 1, 2, 3 … 24. The 24 $\boldsymbol{T_i}$ matrixes are listed in Table 5-1.

| | | | |
|---|---|---|---|
| $\begin{matrix}1&0&0\\0&1&0\\0&0&1\end{matrix}$ | $\begin{matrix}0&0&\bar{1}\\0&\bar{1}&0\\\bar{1}&0&0\end{matrix}$ | $\begin{matrix}0&0&\bar{1}\\0&1&0\\1&0&0\end{matrix}$ | $\begin{matrix}\bar{1}&0&0\\0&1&0\\0&0&\bar{1}\end{matrix}$ |
| $\begin{matrix}1&0&0\\0&\bar{1}&0\\0&0&\bar{1}\end{matrix}$ | $\begin{matrix}1&0&0\\0&0&1\\0&\bar{1}&0\end{matrix}$ | $\begin{matrix}0&\bar{1}&0\\1&0&0\\0&0&1\end{matrix}$ | $\begin{matrix}\bar{1}&0&0\\0&\bar{1}&0\\0&0&1\end{matrix}$ |
| $\begin{matrix}0&1&0\\0&0&1\\1&0&0\end{matrix}$ | $\begin{matrix}0&0&\bar{\bar{1}}\\\bar{1}&0&0\\0&1&0\end{matrix}$ | $\begin{matrix}0&\bar{1}&0\\0&0&1\\\bar{1}&0&0\end{matrix}$ | $\begin{matrix}0&1&0\\0&0&\bar{1}\\\bar{1}&0&0\end{matrix}$ |
| $\begin{matrix}0&\bar{1}&0\\0&0&\bar{1}\\1&0&0\end{matrix}$ | $\begin{matrix}0&1&0\\1&0&0\\0&0&\bar{1}\end{matrix}$ | $\begin{matrix}\bar{1}&0&0\\0&0&1\\0&1&0\end{matrix}$ | $\begin{matrix}0&0&1\\0&\bar{1}&0\\1&0&0\end{matrix}$ |
| $\begin{matrix}0&0&1\\0&1&0\\\bar{1}&0&0\end{matrix}$ | $\begin{matrix}0&1&0\\\bar{1}&0&0\\0&0&1\end{matrix}$ | $\begin{matrix}0&0&\bar{1}\\1&0&0\\0&\bar{1}&0\end{matrix}$ | $\begin{matrix}0&0&1\\\bar{1}&0&0\\0&\bar{1}&0\end{matrix}$ |
| $\begin{matrix}1&0&0\\0&0&\bar{1}\\0&1&0\end{matrix}$ | $\begin{matrix}0&0&1\\1&0&0\\0&1&0\end{matrix}$ | $\begin{matrix}0&0&1\\\bar{1}&0&0\\0&\bar{1}&0\end{matrix}$ | $\begin{matrix}\bar{1}&0&0\\0&0&\bar{1}\\0&\bar{1}&0\end{matrix}$ |

**Table 5-1, 24 symmetries for the cubic system [171]**

The disorientation is defined as the minimum rotation angle of misorientation between two grains which can be determined from $\Delta \boldsymbol{g}'$ matrix by:

$$cos\ \emptyset_{min} = (\Delta g_{11}{}' + \Delta g_{22}{}' + \Delta g_{33}{}' - 1)/2 \qquad \text{Equation 5-14}$$

As OIM analysis software is unable to export any grain boundary data collected by square grid scanning mode, a Matlab code was created by the

author to evaluate disorientation angles. The axis of misorientation is ignored here due to the difficulty of representing it as a scalar.

# 5.2Results

## 5.2.1 Texture

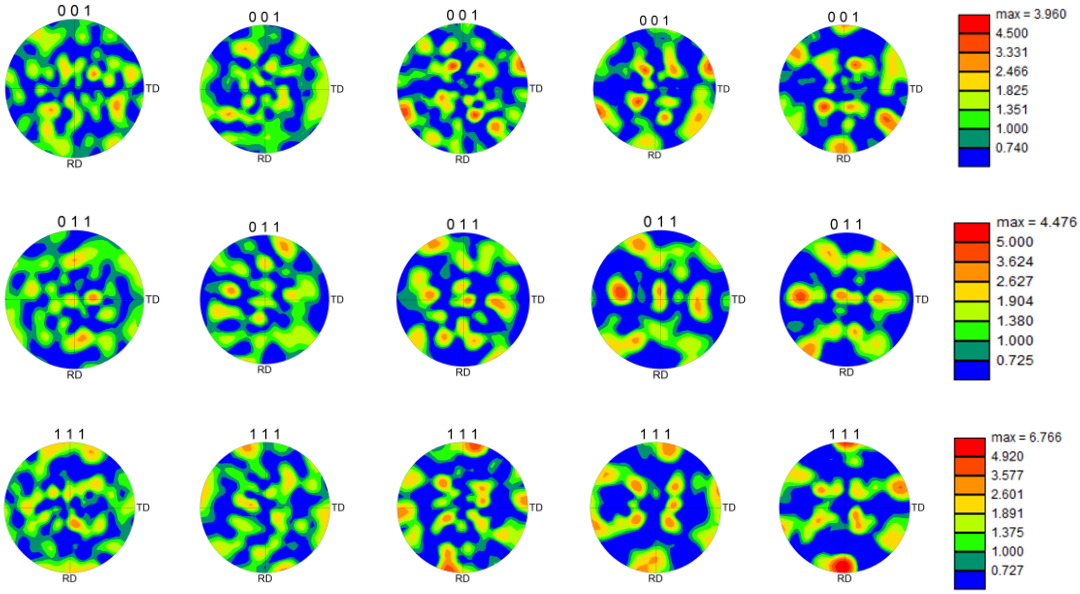
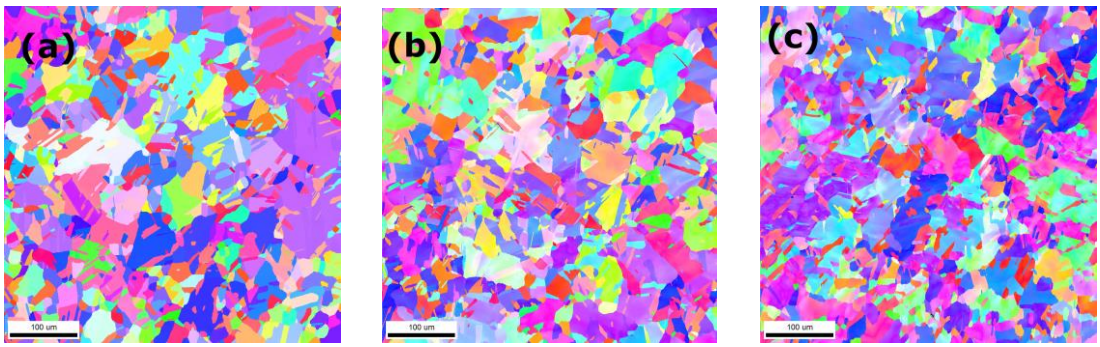



**Figure 5-9, texture plots of {001} {011} and {111} pole figures on 0%, 6%,10%,22.5% and 40% strained copper samples. The external loading axis is aligned with RD**



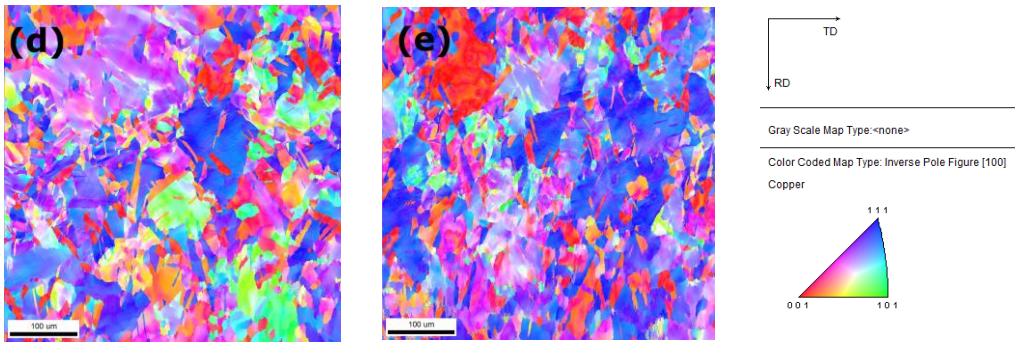



**Figure 5-10, EBSD generated 500 μm x 500 μm orientation maps with 0.5 μm step size on the central regions of (a) 0%, (b) 6%, (c) 10%, (d) 22.5% and (e) 40% strained copper samples. The loading direction is aligned along RD. Note the best direction to colour code IPF would be tensile axis RD.**

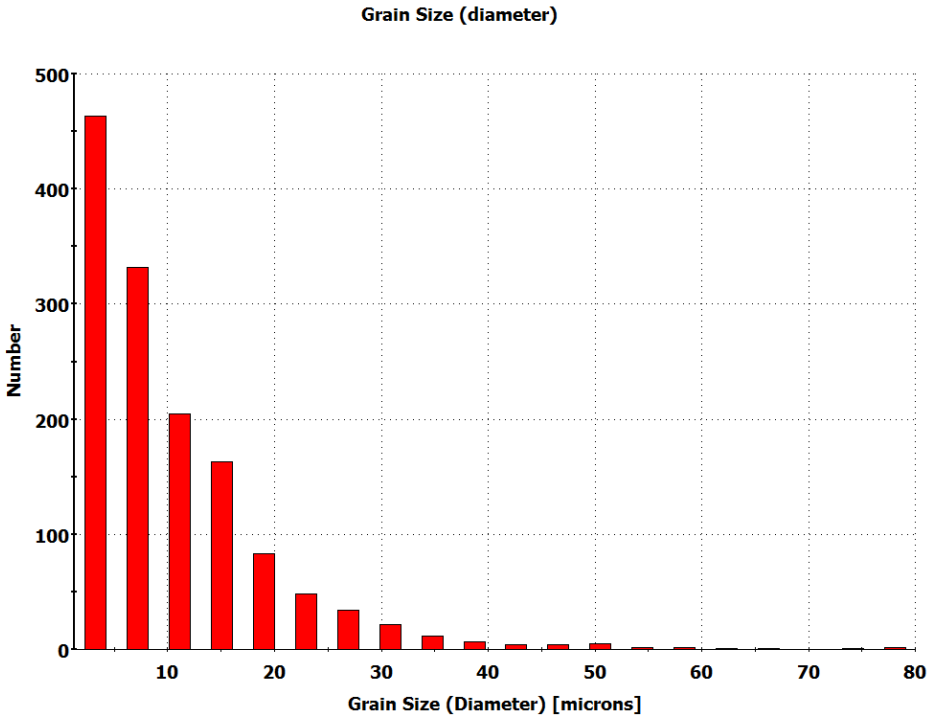



**Figure 5-11, histogram of grain size distribution in the annealed copper sample.**

A weak texture is found in the undeformed copper sample in forms of [001] [011] and [111] pole figures in Figure 5-9. An approximately random orientation distribution is obtained after the annealing process. The evolutions of a weak texture during plastic straining are also shown in Figure 5-9. As the external loading axis was aligned with RD, it is apparent that the intensities of [111] and [100] fibre textures in RD (as shown in pole figures) consistently increase with strain level. In contrast, the [011] texture deviates away from RD.

Figure 5-10 shows the development of orientation maps in the central areas of 0%, 6%, 10%, 22.5%, and 40% strained copper samples. The colour axis is generated along the RD (loading axis). It directly illustrates the texture development in which grains close to [101] orientation (showing as green colour) are disappearing with increasing strain and eventually [111] and [001] oriented grains predominate. Furthermore, minimal orientation gradients are observed in small and moderate deformed samples (0% and 6%) but large orientation gradients become noticeable in highly deformed ones. The annealed sample contains roughly 1600 grains (grain boundary misorientation angle >7 degrees) and reveals that the average grain diameter is 10.5 μm (grain number averaged) though a significant variation of grain size is presented in the distribution (see Figure 5-11). A large proportion of annealing twins exists in the annealed sample due to low stacking fault energy in pure copper. This results in rather complex grain morphologies.

A summary of map average microstructure variables evolutions including GND density, Taylor factor and Schmid factor for 0%, 6%, 10%, 22.5% and 40% sample is presented in Table 5-2. Note that map clean-up processes were carried out on each map in which a grain is defined with grain boundary misorientation angle >7 degrees and minimum size of 5 pixels (1.25 $\mu m^2$). The fraction of data points changed due to clean-up is also included in Table 5-2. Relatively small fluctuation is found in the number of mapped grains and grain size. However the map average grain size seems to decrease with plastic straining. The map average GND density, Taylor factor and Schmid factor follow a consistent tendency with plastic deformation.

| $\varepsilon$) | | | | | |
|---|---|---|---|---|---|
| **Number of Grain** | 1583 | 1673 | 1667 | 1568 | 1517 |
| **Fraction of changed data points in clean up** | 0.1% | 0.2% | 0.2% | 0.9% | 2.2% |
| **Grain diameter(μm)** | 10.5 | 9.9 | 9.7 | 9.5 | 9.2 |
| **Average $\rho_{gnd}$($m^{-2}$)** | 0.2 x $10^{14}$ | 1.2 x $10^{14}$ | 2.1 x $10^{14}$ | 3.7 x $10^{14}$ | 5.3 x $10^{14}$ |
| **Average Taylor factor** | 3.05 | 3.05 | 3.10 | 3.08 | 3.12 |
| **Average Schmid factor** | 0.44 | 0.45 | 0.43 | 0.43 | 0.41 |

**Table 5-2, a summary of map average behaviours during plastic straining**

### 5.2.2 Taylor Factor

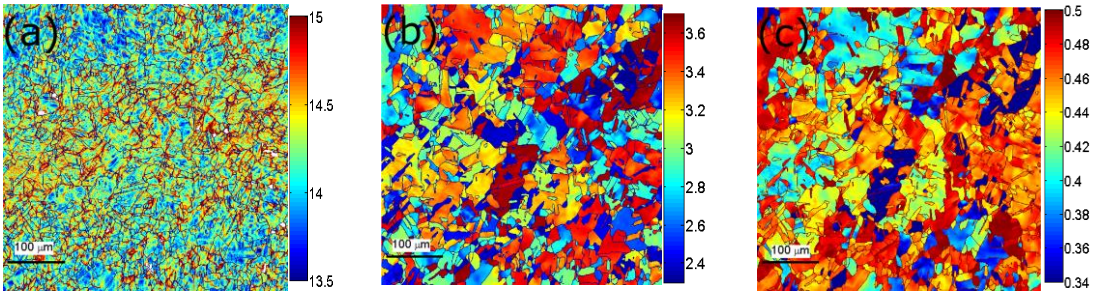



**Figure 5-12, on the 10% tensile strained copper sample (a) HR-EBSD derived lower bound GND density map with 0.5 μm step size. The colour scale is shown in $\log_{10}$ scale and grain boundaries (>7° misorientation) are indicated as the dark blue lines. The low reliable points in cross-correlation analysis were rejected and shown as white area. (b) OIM Analysis 6.1 generated Taylor factor map for which the input slip system is {111} <1 -1 0> and the imposed deformation gradient is -0.5 along the ND, -0.5 along the TD and 1 along the RD. (c) OIM Analysis 6.1 generated Schmid factor map with slip system of {111} <1 -1 0>. The imposed stress state is 1 along the RD and zero for remaining eight components. The grain boundaries are shown as red lines.**

An example Taylor factor map on 10% strain copper sample is presented in Figure 5-12 (b). The Taylor factors were calculated based on the methodology showing in the Analytical method section. The point based and grain average based analyses were presented in Figure 5-13 and Figure 5-14 respectively. The point to point correlation analysis between the stored GND content and its Taylor factor at various strain levels is shown in Figure 5-13. In general, a weak correlation is found between dislocation density and Taylor factor. The three percentile lines are virtually flat in all five samples. Similar to point based analysis, no consistent correlation was found in grain averaged analysis in Figure 5-14.

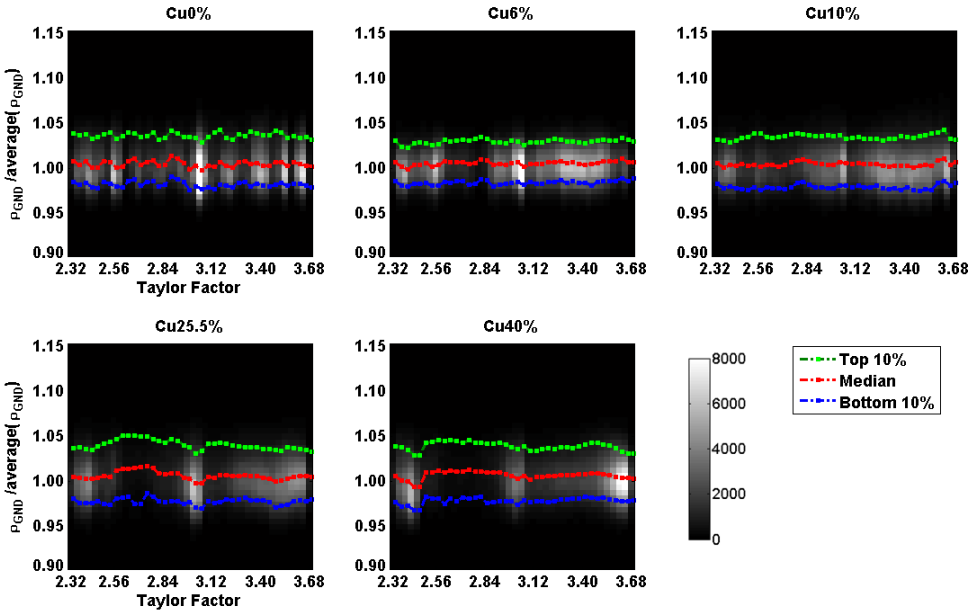



**Figure 5-13, plots of normalised GND density ($\rho_{gnd}/map\ average\ \rho_{gnd}$) as a function of Taylor factor (see Figure 5-12 (b)) in 0%, 2% ,6% 10%, 22.5% and 40% polycrystal copper samples. For each datasets, points were binned with respect to the associated Taylor factor into 40 bins with a bin width of 0.07 and then binned with respect to normalised GND density with a bin width of 0.0063. The top 10%, median and bottom 10% GND density at each Taylor factor range were determined and plotted as green, red and blue lines respectively. Grey scale indicates the number of points filled into a bin.**

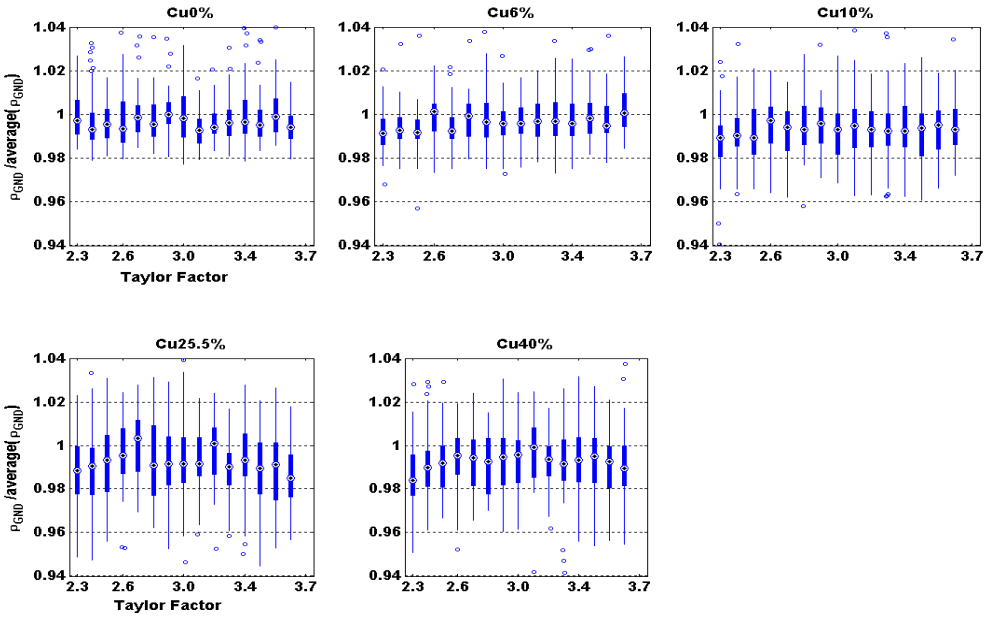



**Figure 5-14, box plots of grain average normalised GND density as a function of grain average Taylor factors in all five samples. Data sets were divided into 16 groups with the group width of 0.075. Any points closer than 2 μm to a grain boundary were rejected from analysis to reduce the grain boundary, grain to grain interaction and triple junction effects. On each box, the central mark is the median, the edges of the box are 25$^{th}$ and 75$^{th}$ percentiles, the whiskers extend to the most extreme data points not considered outliers, and the outliers are plotted as circles. Points are considered as outliers if they are larger than 75$^{th}$ percentiles + 1.5 x (75$^{th}$ percentiles -25$^{th}$ percentiles) or smaller than 25$^{th}$ percentiles - 1.5 x (75$^{th}$ percentiles -25$^{th}$ percentiles).**

### 5.2.3Schmid Factor

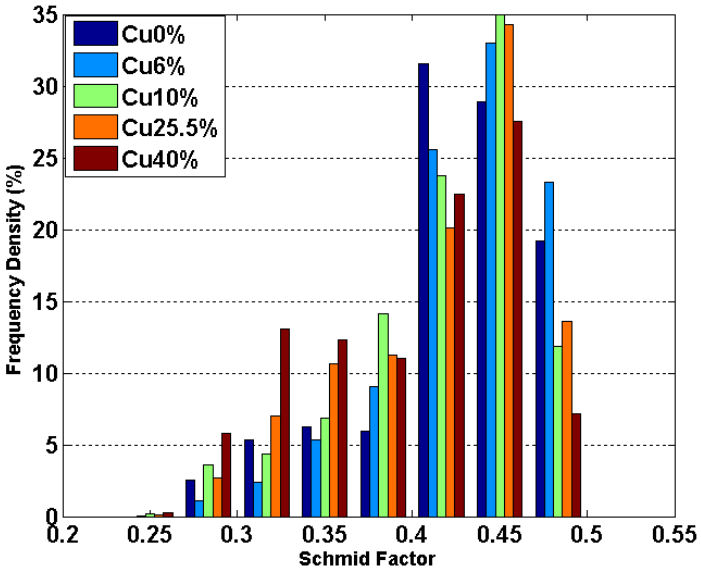



**Figure 5-15, histograms of Schmid factors distributions in 0%, 6%, 10%, 25.5% and 40% tensile strained copper samples. For each dataset, Schmid factors are divided into 10 bins with bin width of 0.333.**

The Schmid factor map of 10% deformed copper is presented in Figure 5-12(c) as an example to show general Schmid factors distribution in probed samples. Systematic analysis in Schmid factor distribution and evolution is shown in Figure 5-15. The histogram shows that initially Schmid factors are highly skewed to the higher end ('soft') and this skew becomes less pronounced with progressive straining (i.e. soft grains are being reoriented towards harder orientations). Significant frequency reduction from annealed sample occurs at the first and third bins from the left hand side. It seems these points evolved into relatively lower Schmid factors (hard).

Figure 5-16 shows the point to point correlation analysis between GND density and Schmid factors. For the annealed sample, no correlation can be seen. However even for deformed samples, only a relatively small increase in dislocation density is found to appear at points with high Schmid factors. This weak tendency is most noticeable in 25.5% strained sample. Small

increases as well as decreases in dislocation density are found in the lower Schmid factor end ('hard') in 10% and 40% samples. However, these changes are not consistent with progressive straining. Similarly in Figure 5-17 no correlation was found in the grain averaged analysis.

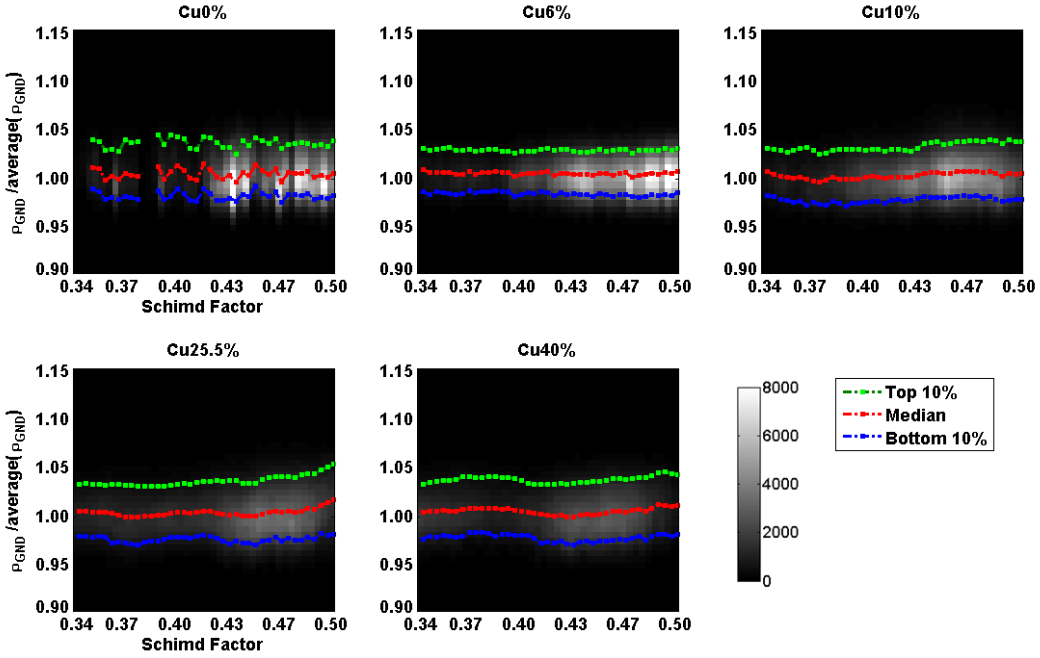



**Figure 5-16, plots of normalised GND density ($\rho_{gnd}/map\ average\ \rho_{gnd}$) as a function of Schmid factor (see Figure 5-12 (c)) in 0%, 2% ,6% 10%, 22.5% and 40% polycrystal copper samples. For each datasets, points were binned with respect to the associated Schmid factor into 40 bins with a bin width of 0.07 and then binned with respect to normalised GND density with a bin width of 0.0063. The top 10%, median and bottom 10% GND density at each Schmid factor range were determined and plotted as green, red and blue lines respectively. Grey scale indicates the number of points filled into a bin. Minimum 3000 data points within a bin are required to plot percentile lines.**

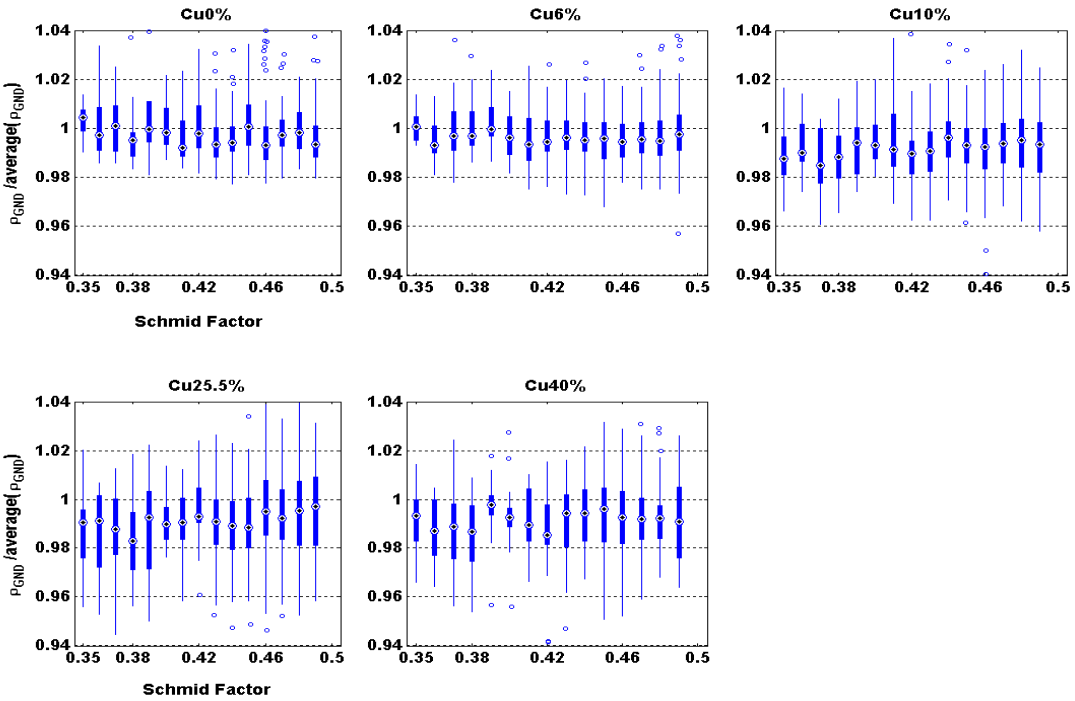



**Figure 5-17, similar box plots as Figure 5-14 but showing grain average normalised GND density as a function of grain average Schmid factors in all five samples. Data sets were divided into 16 groups with the group width of 0.0075. Any points closer than 2 μm to a grain boundary were rejected from analysis to reduce the grain boundary, grain to grain interaction and triple junction effects.**

## 5.2.4Inclination angle

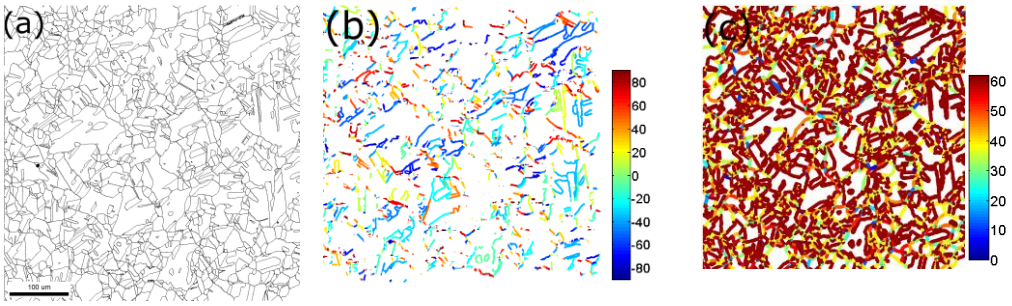



**Figure 5-18, for the annealed copper sample (see Figure 5-10 (a)), (a) grain boundary 'skeleton' map. A grain boundary is defined as neighbouring points with misorientation larger than 7 degrees; (b) the calculated grain boundary inclination angles with regard to the external loading axis based on the method present in the section; (c) determined grain boundary disorientation map. Detailed method description is presented in the Analytical method section.**

The geometries of grain boundaries with regards to loading axis for all five samples were determined based on the method presented in Analytical method section. An example of inclination angle map on the annealed sample is illustrated in Figure 5-18 (b). As shown in Figure 5-19, large fluctuations appear in the dislocation density and grain boundary inclination angle relation analysis. However, in general no correlation between these two variables is found and there is little difference in various straining levels.

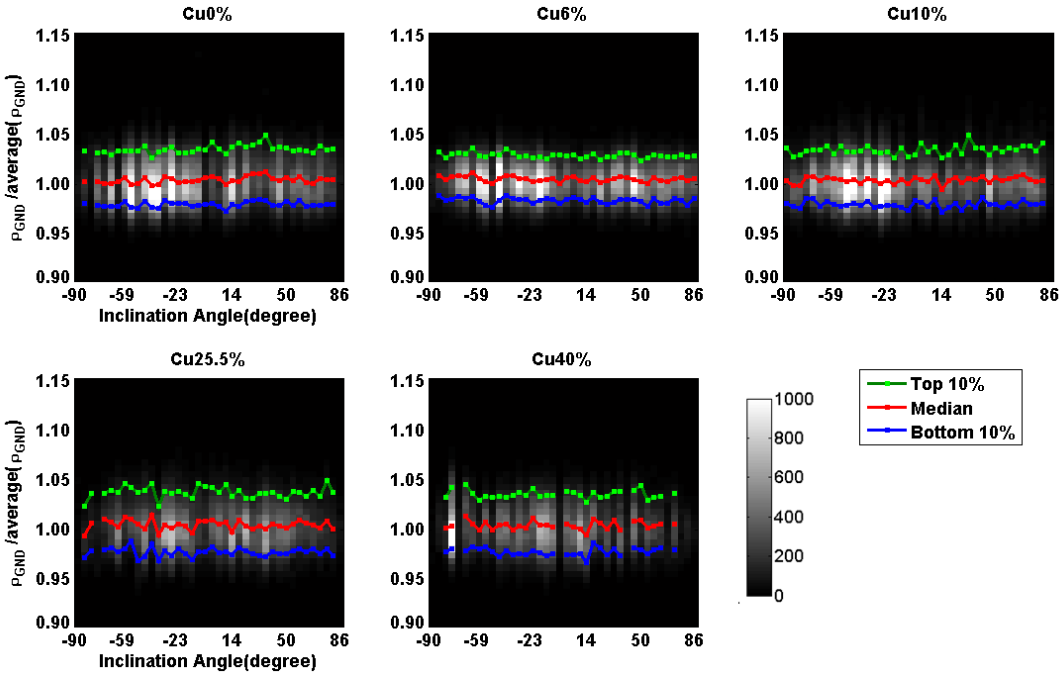



**Figure 5-19, plots of normalised GND density ($\rho_{gnd}/map\ average\ \rho_{gnd}$) as a function of grain boundary inclination angle with regard to loading axis in 0%, 2% ,6% 10%, 22.5% and 40% strained samples, points closer than 3 μm to grain boundaries are included in this analysis and their inclination angles are assigned to the inclination angle of the closest grain boundaries. For each datasets, points were binned with respect to the associated disorientation factor into 40 bins with a bin width of 8 degrees and then binned with respect to normalised GND density with a bin width of 0.0063. The top 10%, median and bottom 10% GND density at each inclination angle range were determined and plotted as green, red and blue lines respectively. Grey scale indicates the number of points filled into a bin. Minimum number of 1000 data points within each bin is required to plot these percentile lines.**

## 5.2.5Disorientation angle

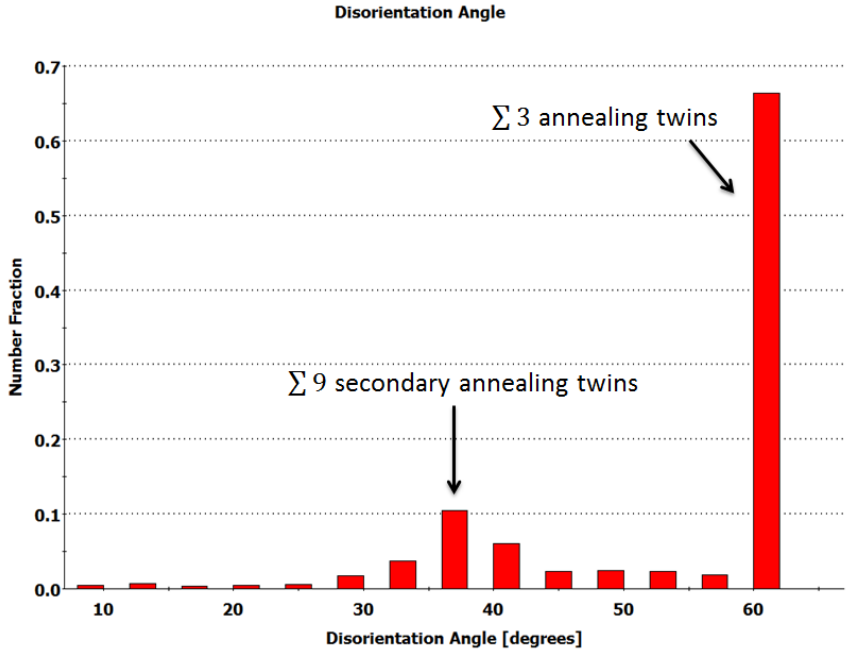



**Figure 5-20, the histogram of disorientation angle distribution for the annealed sample. Data sets were divided into 15 bins with bin width of 3.7 degrees.**

The minimum misorientation angles (disorientation angle) between two neighbouring grains were evaluated and an example for the annealed sample is presented in Figure 5-18 (c). The associated disorientation angle distribution is shown in Figure 5-20. As noted in Figure 5-10 (a), the primary and secondary annealing twinning boundaries $\sum 3$ and $\sum 9$ predominate

(~75%) in disorientation angles. The evolution of disorientation angle during plastic deformation is shown in Figure 5-21. The initial annealing twins began to rotate with plastic deformation such that highly populated twinning disorientation angles spread out.

Statistical analysis suggests no correlation between GND density and disorientation angle in all five samples, though the range of normalised dislocation density increases with plastic deformation. The annealing twin

boundaries, low and high disorientation grain boundaries do not manifest any special effects on dislocation accumulation.

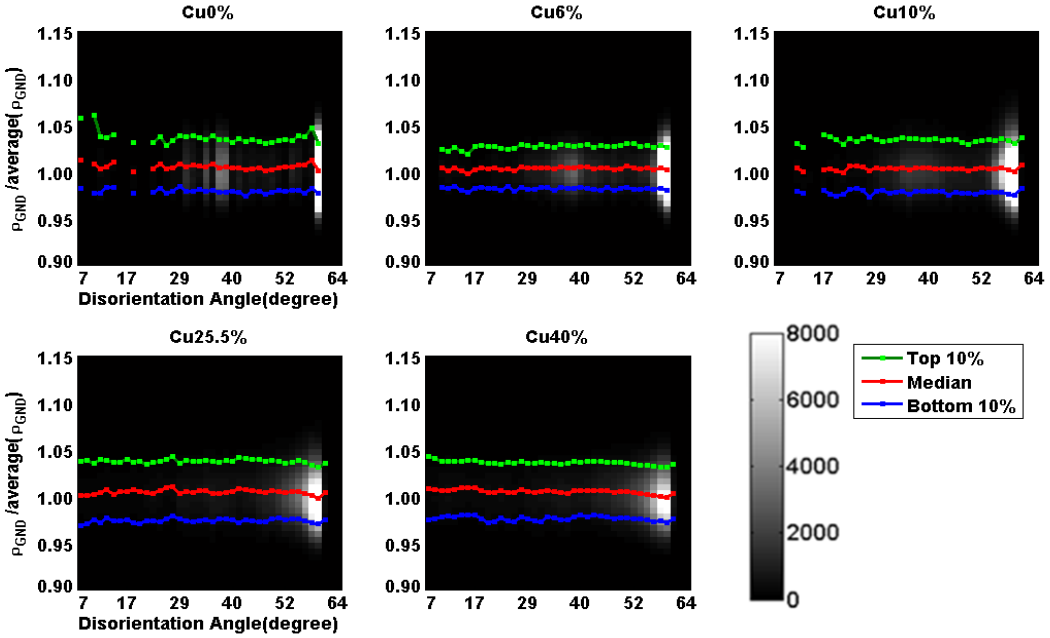



**Figure 5-21, plots of normalised GND density ($\rho_{gnd}/map\ average\ \rho_{gnd}$) as a function of disorientation angle between a tested point (closer than 3 μm to the nearest grain boundary) and its nearest neighbouring grain in 0%, 2% ,6% 10%, 22.5% and 40% polycrystal copper samples. For each datasets, points were binned with respect to the associated disorientation factor into 40 bins with a bin width of 2 degrees and then binned with respect to normalised GND density with a bin width of 0.0063. The top 10%, median and bottom 10% GND density at each disorientation angle range were determined and plotted as green, red and blue lines respectively. Grey scale indicates the number of points filled into a bin. Minimum number of 1000 data points within each bin is required to plot these percentile lines.**

## 5.3 Discussion

The lower bound GND content was recovered using HR-EBSD technique on 0%, 6%, 10%, 22.5% and 40% uniaxial tensile strained copper samples with a probing area of 500 μm x 500 μm containing ~1600 grains. In this chapter, systematic statistical analyses to study the GND behaviours as a function of materials microstructure were extended to lattice orientation dependence e.g. Taylor factor and Schmid factor and grain boundary effects e.g. grain boundary inclination angle to loading axis and grain boundary disorientation angle. In addition, the texture evolution for copper under tension was studied.

The development of texture for FCC copper agrees with expectation that grains close to [101] orientation tended to deform first due to the highest resolved shear stress acting on this orientation. These grain continued to rotate toward [001] and [111] orientations which results in highly concentrated fibre texture in RD in the [111] and [001] pole figures (see Figure 5-9). As a result of texture evolution the map average Taylor factors and Schmid factors move toward to the 'hard' ends with progressive straining as shown in Table 5-2. This suggests that during plastic deformation soft grains deformed first and became harder. Therefore, grains with low Taylor factors or high Schmid factors would expect deformation occur first or would have relatively higher deformation state than the 'hard' grains. Therefore a higher dislocation density would expect to exist in the soft grains and a relatively lower dislocation density would present in those hard grains. These have been indirectly substantiated by microhardness assessment [44], X-ray [43, 172] and neutron diffraction [173] line broadening strain energy measurements and

recent EBSD Hough based GND density analysis [45] on copper, steel and aluminium deformed under cold rolling and uniaxial tension. Also direct qualitative TEM characterisations showed distinct dislocation patterns formed in various orientations during plastic deformation [41, 42, 174, 175].

Conversely, the point to point statistical analyses suggest the HR-EBSD estimated dislocation density is almost independent of crystal orientations using either Taylor or Schmid approach at all five straining levels. In order to make comparison with other quantitative techniques e.g. X-ray, neutron and microhardness for which measurements had been obtained in grain interiors due to their coarse spatial resolutions, the statistical analysis on GND density as a function of crystal orientation was therefore furthered to examine grain average GND density as a function of grain average orientation in which the effects from grain boundaries, triple junctions, grain-grain interaction were minimised by excluding points having distance smaller than 2 μm to grain boundaries.

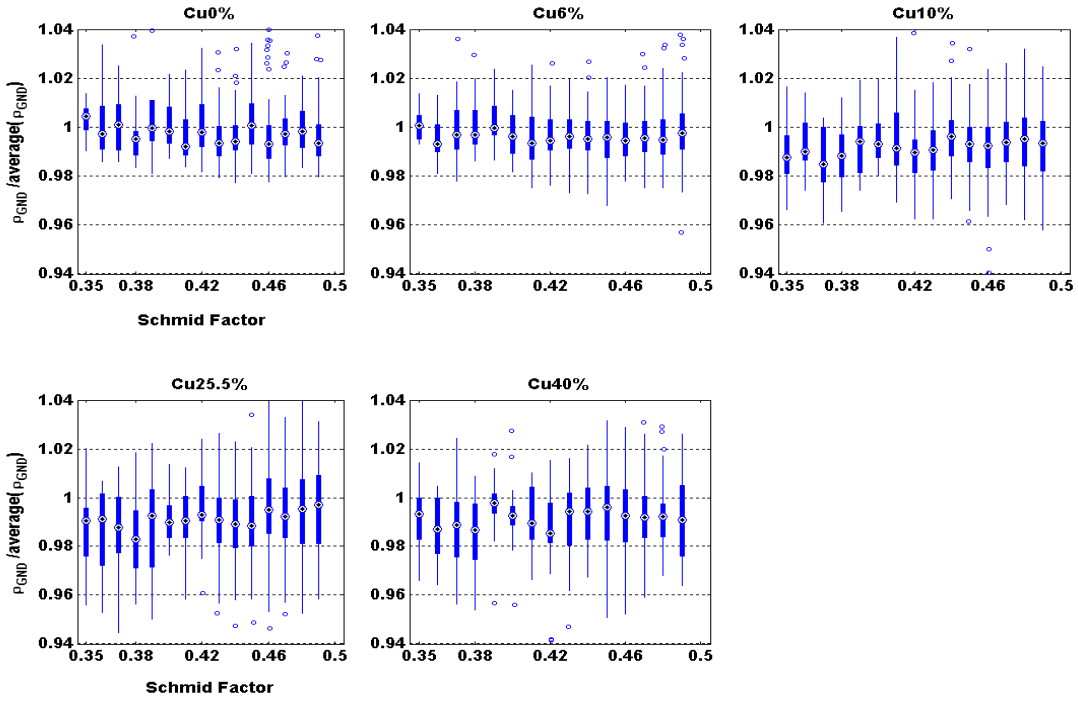


Figure 5-14 and Figure 5-17 show considerable fluctuations with respect to Taylor factor or Schmid factor. However, in neither approach is a consistent tendency observed with progressive loading.

To date, all reported quantitative analysis on orientation dependence with stored energy (dislocation density) show a large scattering even for moderately deformed samples. Despite the different testing materials and mechanical testing methods, two common drawbacks existed in the previous quantitative investigations are the limited number of samples to various strain levels and the constrained number of probed grains. For instance in the microhardness analysis [44], only the annealed and 6% cold rolled steel samples were accessed. And in each sample merely ~100 grains were tested (see Figure 5-22) which is far from being representative of bulk materials (>1000 grains) [176]. If we only focus on a single deformed copper sample in Figure 5-14 or Figure 5-17, a similar trend can also be claimed. However due to the consistency with other deformed samples and the scattering of that dataset, claiming a weak correlation is statistically questionable.

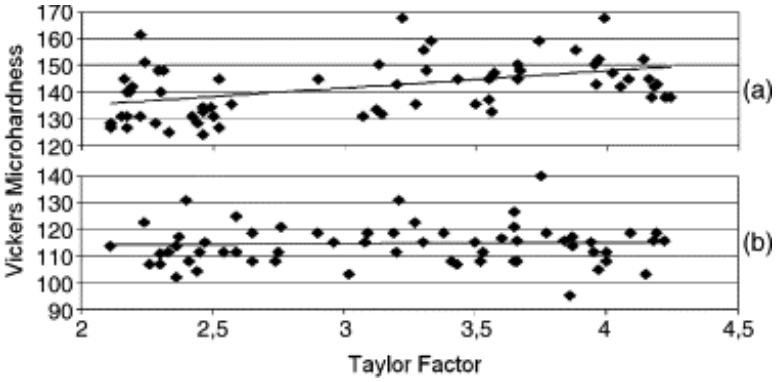



**Figure 5-22, microhardness measurements as a function of Taylor factor in individual ferrite grains. (a) 6% cold rolled sample. (b) anneal sample[44].**

The observed large scatter implies that lattice orientation is not one of the primary factors affecting dislocation accumulation. As pointed out by Trivedi [172] and Allain-Bonasso [177] that the interactions with neighbouring grains in polycrystal may be more significant. It should be emphasised that the obtained Taylor or Schmid factors were calculated based on post deformation orientations. I n other words, the initial factors prior to deformation were unknown. Therefore the final Taylor or Schmid factors are a mixture of grains transformed from those soft grains and the original hard grains as seen from texture development in Figure 5-9. Also, the probed free surface regions might not represent the bulk behaviour due to the lack of constraint at the free surface comparing to bulk materials.

Although the texture evolution results suggested soft (high Schmid factor) grains had deformed first and rotated toward the lower Schmid factors, assuming that high dislocation density should exist in the soft grains is unnecessarily because grain rotation process can be accomplished by other means such as the activation of more slip systems, formation of dipoles and dislocation absorption by grain boundaries. Fundamentally, Taylor factor is directly linked to the number of active slip systems rather than the stored dislocation density. It is often assumed that high number of slip systems results in more stored dislocation density however no quantitative experimental results have been found in literature to support this hypothesis. Although qualitative TEM observations [42, 175] demonstrated different dislocation patterns were developed in various orientations, these results do not directly support dislocation density dependence upon crystal orientations.

They could also be interpreted as different dislocation mechanisms operating in various orientations.

The observed fluctuations in grain average analysis in Figure 5-14 and Figure 5-17 especially for the annealed sample might suggest that larger number of grains need to be sampled. The number of sampled grain in this analysis has been reduced from initial ~1600 to ~900 due to the rejection of small grains (less than 4 μm) to reduce the grain boundaries effects.

More recent work by Allain-Bonasso [177] quantitatively investigated orientation dependence with five IF steel samples under 0% 4.7% 6.7% 12% and 17% uniaxial tensile straining by using conventional Hough based EBSD method. 1300-2200 grains were mapped in each sample. Their results agreed with our findings and also suggested that plastic heterogeneity (equivalent to GND density) is independent of texture.

It was seen in the Chapter 4. that grain boundaries were primary locations for dislocations to accumulate particularly in the annealed sample in which almost all dislocations concentrated near or at grain boundaries. However, this correlation became progressively weaker as the imposed strain increased. Based on bi-crystals studies one of the speculations was that at highly deformation state various grain boundary manifested distinct characters to interact with dislocations e.g. some might act as dislocation barriers [178] while some might be dislocation sinks [122]. It was reasonable to link these to the nature of grain boundaries (disorientation angle) and the morphology of grain boundaries (inclination angle to loading axis). It is of great interest to note that in the present statistical analysis no obvious correlation was found

between the dislocation content and these two important grain boundary properties. These results suggest that during the annealing process grain boundaries are where dislocations assembled or possibly were emitted. With the progressively imposed plastic strain, dislocation density increased and these dislocations arrange themselves to form a more energy efficient configuration. Although this configuration is near grain boundaries, its development does not seem to depend upon the above two properties. This may explain the observations made by Sun et al that dislocations aggregated at grain boundary at slightly strained sample but penetrated through grain boundaries at highly strained sample.

It is well known that there are many possible approaches to further the investigation on grain boundary properties. However the observed total independence is rather surprising given the extensive studies on dislocation-grain boundary interactions. Three distinctions between the present analysis and literature should be noted here. Frist, to the author's knowledge, the present data sets are the most quantitative ones which have been reported for studying dislocation- grain boundary interactions as a function of imposed strain level (in terms of resolution, area and number of grains studied, as well as strain levels). The previous investigations for both TEM and EBSD methods were constrained in rather limited number of grain boundaries or strain states. Second, EBSD technique can probe more bulk representative results than TEM method as EBSD samples do not require ultra thin foil for electrons to transmit through. Third, the majority of previous studies were carried out on bicrystals rather than polycrystals where other microstructure

variables might have higher priority or be more energetically favoured to interact with dislocations than grain boundaries e.g. possibly triple junctions.

The present results on grain boundary inclination angle are actually in a good agreement with recently developed micromechanical modelling using crystal plasticity finite element method(CPFEM) [179] based on advanced Lamel (ALAMEL) model [180] in which the plastic heterogeneity arising from the influence of a grain boundary on the cooperative deformation of neighbouring grain. A critical assumption was that the adjacent grains undergo opposite shears parallel to the grain boundary. No marked difference was found in their simulation in the behaviour of grain boundaries with different inclination angles with regard to external loading. However triple junction revealed high stress gradients with oscillatory behaviour.

Finally, it should be noted that all current results were collected on pure FCC copper samples, the deformation mechanisms are different in BCC and HCP materials due to the altered crystal structures [147]. This is evident in HCP titanium, for which the limited number of slip systems makes the orientation dependence become more obvious as revealed by nano-indentation [135].

## 5.4 Conclusions

In this chapter, the general texture evolution in polycrystalline copper under uniaxial tension was presented. And quantitative analysis on HR-EBSD recovered GND content as functions of grain orientations related parameters e.g. Taylor factors and Schmid factors, grain boundary morphologies and disorientation angles were conducted. The following conclusions can be drawn.

1. The texture of polycrystalline copper under uniaxial tension were developed that [011] oriented grain deformed first and rotate toward to the [111] and [001] orientations. This agrees well with the texture prediction made by Taylor models.
2. The point to point quantitative analysis showed no consistent correlation between dislocation density and Taylor factors or Schmid factors.
3. Large scatter was presented in grain average dislocation density as a function of Taylor or Schmid factors analysis. The obtained results suggest the development of dislocation density is independent of grain orientations.
4. No correlation is found in dislocation density as a function of grain boundary disorientation analysis at all five straining levels. The special grain boundaries such as $\sum 3$ and $\sum 9$ CSL boundaries show little special character to interact with dislocations in either annealed or deformed ones.
5. In the annealed and plastically deformed samples, grain boundary inclination was also found irrelevant to dislocations density distribution and evolution in which minimal trend could be observed.
6. These results might imply that at least dislocation density is not controlled by a single local microstructural parameter. Perhaps several parameters are in conjunction or effects over several grains are more important.

# Chapter 6. Qualitative Analysis of Dislocation Structures

In Chapter 4. and Chapter 5. , the evolution of the dislocation density distribution in progressively deformed polycrystalline copper samples as functions of tensile plastic strain and microstructure characters e.g. grain boundaries (GBs), triple junctions (TJs) and crystal orientations, have been quantitatively studied. Some interesting findings were made such as TJs are preferential sites for accumulating dislocations; dislocations assemble near GBs at low and moderate deformation level, and this tendency gradually reduces with increasing strain. The combination of quantitative analyses with direct visual qualitative inspections provides a comprehensive assessment on the development of dislocation networks morphology and patterning. In this chapter the main emphasis is on qualitative microscopic observations of dislocation networks morphology and their development with respect to microstructure features.

There are five aims for this chapter: (1) present general observed deformation microstructural features and make comparisons with the literature, primarily TEM observations; (2) assess qualitatively the effect of grain orientation on the dislocation network structure; (3) visually assess the effects of grain-grain interactions on deformation microstructures and their development with further straining; (4) assess the impact of the twin network on dislocation accumulation; (5) inspect the nature of dislocation structures near TJs.

# 6.1 Analytical methods

## 6.1.1 Grain orientation dependence

A number of grains with three orientations ([011], [001] and [111]) will be selected from the IPF and their associated dislocation structures will be examined and compared with TEM measurements. As twins and triple junctions (TJs) effects on deformation microstructure will be addressed in the later sections, the structures formed in the interior of large grains will be examined.

As the calculated IPF in EBSD associated OIM analysis software cannot be directly loaded in Matlab for further analysis, a Matlab script were created to transform the EBSD measured three Euler angles into IPF. The detailed transformation process is described as following.

First, grain averaged orientations were determined from the collected EBSD maps by applying cleaning process using the OIM analysis software. The EBSD measured three Euler angles ($\varphi_1$, $\varphi_2$ and $\emptyset$) were loaded into Matlab.

Subsequently the Orientation matrix, **g**, according to Equation 6-1 was calculated for each point.

$$\boldsymbol{g} = \begin{pmatrix} cos\varphi_1 cos\varphi_2 - sin\varphi_1 sin\varphi_2 cos\emptyset & sin\varphi_1 cos\varphi_2 + cos\varphi_1 sin\varphi_2 cos\emptyset & sin\varphi_2 sin\emptyset \\ -cos\varphi_1 sin\varphi_2 - sin\varphi_1 cos\varphi_2 cos\emptyset & -sin\varphi_1 sin\varphi_2 + cos\varphi_1 cos\varphi_2 cos\emptyset & cos\varphi_2 sin\emptyset \\ sin\varphi_1 sin\emptyset & -cos\varphi_1 sin\emptyset & cos\emptyset \end{pmatrix}$$

Equation 6-1

Since loading and rotation axis is along the RD ([100] axis) and can be represented as:

$$\boldsymbol{a} = \begin{pmatrix} 1 \\ 0 \\ 0 \end{pmatrix}$$ Equation 6-2

Applying the orientation matrix **g** to the unit vector **a** results in a vector **n** where **n** is expressed as:

$$\boldsymbol{n} = \boldsymbol{g}\boldsymbol{a} = \begin{pmatrix} cos\varphi_1 cos\varphi_2 - sin\varphi_1 sin\varphi_2 cos\emptyset \\ -cos\varphi_1 sin\varphi_2 - sin\varphi_1 cos\varphi_2 cos\emptyset \\ sin\varphi_1 sin\emptyset \end{pmatrix}$$ Equation 6-3

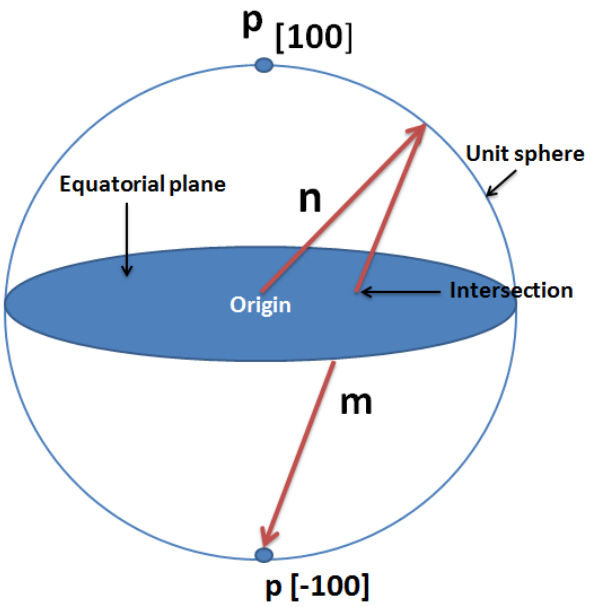



Figure 6-1, schematic illustration showing how a stereogram is generated.

A stereogram was prepared by pointing the vector $\boldsymbol{n}$ out of the origin and striking at a unit sphere (see Figure 6-1). A vector **m** which falls back to the plane of the page toward to the opposite pole was calculated. In this case, if $n_1$ is positive the opposite pole **p** = [-1 0 0] is used else using pole **p** = [1 0 0]. The line can be expressed as $\boldsymbol{r} = \boldsymbol{p} + \lambda \times \boldsymbol{m}$. The **r** intersection with the

equatorial plane can be found by finding a $\lambda$ such that $r_1$ is equal to zero. As 24 symmetries exist in fcc crystals, 24 symmetric operations were applied and the points fell in the IPF unit triangle are plotted in Figure 6-2.

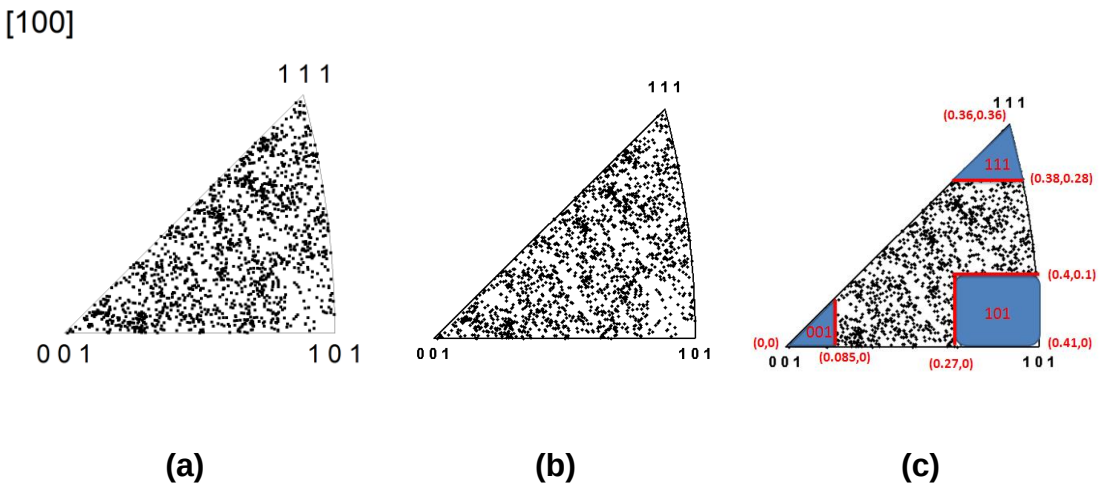



**Figure 6-2, IPFs rotate along [100] axis on 6% tensile strained copper sample generated by (a) OIM software (b) Matlab script. (c) Highlighting the selected [111] [001] and [101] regions with threshold line coordinators.**

This scipt was envaluated by comparing the calculated IPF on 6% strained copper in Figure 6-2 (b) to OIM determined IPF Figure 6-2 (a). As these two IPFs are identical, the matlab obtained IPF were used to further define three regions [001], [111] and [110] for orienation dependence study. The coordinors of threhold lines and divided regions are highlighted in Figure 6-2 (c). It should be noted that the boundaries of these three regions are rather subjective and not attemtos has been made to keep the angular arears of th three regions the same. The <101> region is larger because the grain orientations tend to rotate away from this corner during deformation.

### 6.1.2 Annealing twins

Generally, two criteria are used to define twins. First, within some given tolerance the orientation of the twin is related to the parent through a specific

misorientation angle. Second, the twinning plane must be coincident with the grain boundary plane. If a twin fulfils both criteria, it is defined as a coherent twin. If a twin only satisfies the first criterion, it is defined as incoherent twin. The coherent and incoherent twins are considered to behave differently. However, as EBSD is a two dimensional measurement tool, the crystallography information along surface normal is not accessible unless serial sectioning is performed. Therefore the second criterion in our case can not be unambiguously determined. Hence coherent twin boundaries and incoherent twin boundaries are not going to be distinguished. Only twin boundaries which satisfy the first criterion are going to be determined.

Previously grain boundary misorientation angles have been determined. In FCC copper, the primary annealing twins $\sum 3$ can be characterised as 60° rotation about a <111> axis with an angular tolerance of 8.7° [171]. The secondary recrystallization twins $\sum 9$ are described as 38.9° rotation about a <110> axis with 5° angular tolerance [171]. These two types of twin are separated from ordinary high angle GBs in Matlab. Results were compared to OIM generated GBs in which both misorientation angle and rotation axis were used. Little difference was found between these two approaches. Direct qualitative visual inspections on dislocation structures near twin boundaries are carried out.

### 6.1.3 Triple junctions

| | | | | | | |
|---|---|---|---|---|---|---|
| $\sum 3, \sum 3$ , $\sum 3$ | HA,HA, HA | HA, $\sum 3, \sum 3$ Or HA,HA, $\sum 3$ | HA, $\sum 9, \sum 9$ Or HA,HA, $\sum 9$ | HA, $\sum 3, \sum 9$ | $\sum 3, \sum 9, \sum 9$ Or $\sum 3, \sum 3, \sum 9$ | $\sum 9$, $\sum 9, \sum 9$ |
| 333 | HHH | 3H0 | 9H0 | 39H | 390 | 999 |

**Table 6-1, the classified TJs consist of various set of constitutional GBs. HA is used to represent the high angle GBs.**

Different combinations of GBs at TJs might possess distinct properties to interact with dislocations. In Chapter 4. , the locations of TJs where three or more grains intersect were determined. And, in the preceding subsection, the $\sum 3$, $\sum 9$ and high angle (HA) GBs were distinguished. Having obtained both TJ locations and GBs types, it is not very difficult to directly determine the three constitutional GBs for each TJ. Thus seven types of TJs were classified as shown in Table 6-1.

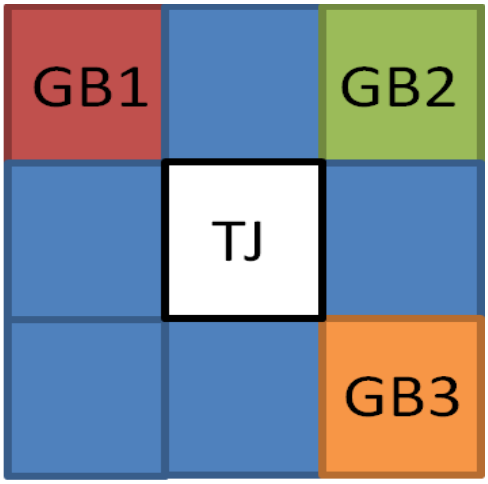



**Figure 6-3, a diagram shows the structure of a triple junction within a 3x3 pixel window. By interrogating each pixel, the three constitutive GBs can be determined.**

For each TJ, a 3x3 pixel window was created around it with TJ in the middle as seen in Figure 6-3. By determining the types of GBs contained within the eight neighbouring pixels, the type of TJ can hence be calculated. It should be noted that all TJs are assumed to have only three GB components. If three constitutional GBs consist of only two types GBs for example, a TJ consists of $\sum 3$, $\sum 3$ and $\sum 9$ GBs, for the sake of simplicity only the types of GBs are considered. Therefore as shown in Table 6-1, two possible sets exist in type 2, 6 and 7 TJs.

In quantitative analysis, TJ associated dislocation density need to be calculated. Hence the dislocation-TJ interacting area was defined within 0.5 μm from TJs. In other words, for each TJ point the dislocation density value was calculated as the mean of dislocation densities in the 3x3 pixel window. One pixel away from TJs is the smallest distance away from TJs. If the distance is too large, this zone may include many TJ unaffected data points.

## 6.2 Results

### 6.2.1 Characteristic deformation microstructures

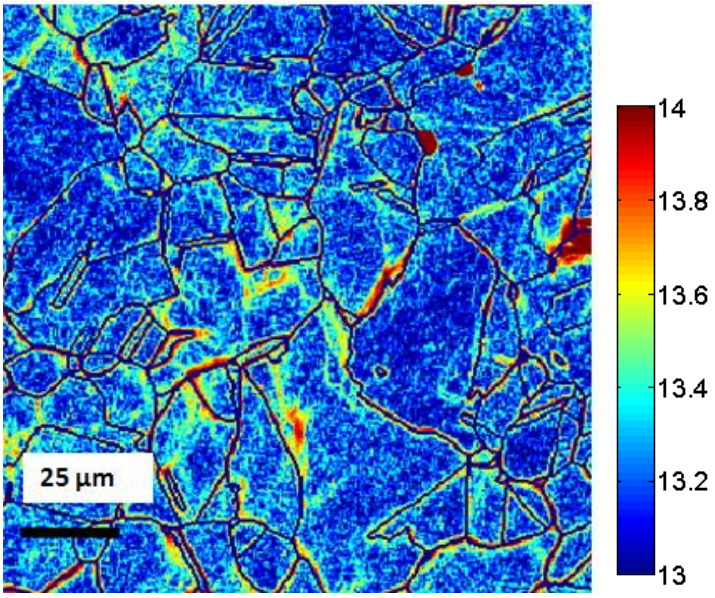



**Figure 6-4, an enlarged 150µm x150 µm GND density map of the undeformed copper sample extracted from the central region of the large 1000 µm x1000 µm GND map. The colour scale is on $\log_{10}$ scale and dark blue lines represent GBs with minimum misorientation angle of 10 degrees between adjoined pixels.**

As shown in Figure 6-4, after 15 minutes annealing at 550 degrees ($0.5T_m$), most deformation structure is removed. There are some remaining dislocations accumulated near GBs rather than grain interiors, and the accumulation near boundaries is heterogeneous. Also some dislocation structures seem remaining in a small number of grains as highlighted in Figure 6-4. Furthermore few small grains and TJs cluster a significant number of dislocations. However investigations on the recovery and recrystallization process are beyond the scope of this project thus no further analysis will be carried out.

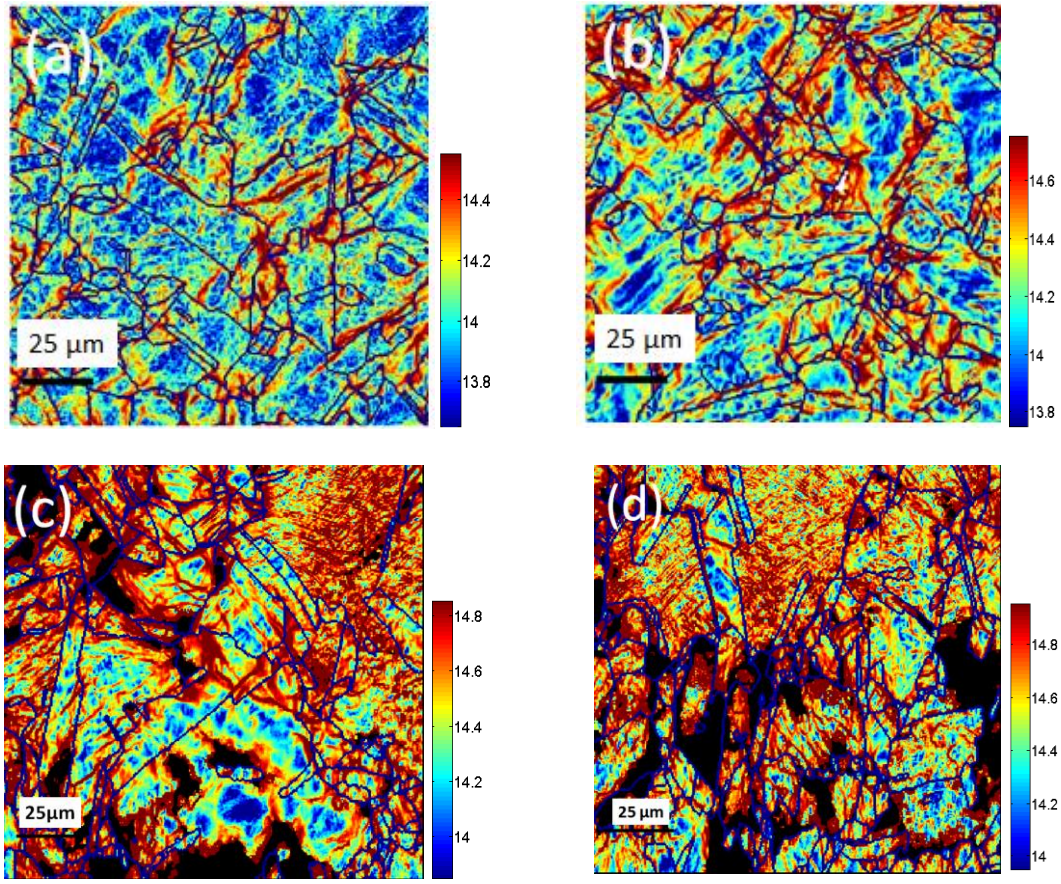



**Figure 6-5, 150 µm x150µm GND density maps extracted from the central regions of 1000 µm x1000µm GND maps in copper samples (as shown in Figure 4-1)) which were deformed under tensile strains at (a) 6%, (b) 10%, (c) 25.5%,(d) 40%. The colour scales were in $\log_{10}$ scale and were adjusted for individual map to highlight dislocation structures. Dark blue lines represent GBs with minimum misorientation angle of 10 degrees between neighbouring pixels. The dark areas showing in (c) and (d) are consisting of rejected points from reliability assessment in cross-correlation process. The failure to pass cross-correlation quality examination may due to the present of large GND densities. For all the GND maps, the tensile loading axis is along the vertical direction.**

Significantly heterogeneous deformation microstructures were developed during plastic deformation. At 6% strain, as shown in Figure 6-5(a), dislocation cells are observed in almost all grains. The dislocation density stored in dislocation cell walls is estimated as $1.88 \times 10^{14}$ $m^{-2}$ where in dislocation cell interiors the dislocation density is estimated as $0.19 \times 10^{14}$ $m^{-2}$.

The most pronounced feature in this map is curved band-liked dislocation structures. High dislocation densities are stored within them. Most of these bands are oriented in a range between 35-55 degrees to the loading axis.

Some of them are formed within grains and others span across grains and GBs and therefore form a connected dislocation network. The morphologies of these bands vary in different grains e.g. wavy, curved and straight bands.

With increasing deformation to 10% strain (see Figure 6-5 (b)) a higher fraction of dislocation bands were formed. Comparing to 6% strained map, the bands have evolved into a thicker forms and have more branches. Wavy bands are commonly observed. In some grains, some straight dislocation bands are perpendicular to each other.

High dislocation density (~$1x10^{15}$ $m^{-2}$) is found within those dislocation cell walls and relatively low dislocation density is found within dislocation cell interiors (~$3.2x10^{13}$ $m^{-2}$). In some grains dislocation cells are well defined by these regions, and they are relatively uniformly distributed. In other grains subdivision takes place such that grains are divided by dislocation bands into a few domains. The paths of some main dislocation bands follow along some GBs.

At higher deformation levels (25.5%) a clear dislocation cell arrays are displayed e.g. at the top right corner. Comparing with the former maps (6% and 10%), the dislocation cell arrays evolved into more compact arrangements. Long range dislocation bands are absent within the grains. In other grains the dislocation density difference between dislocation cell interiors (~$8x10^{13}$ $m^{-2}$) and dislocation cell boundaries (~$2.5x10^{15}$ $m^{-2}$) are enlarged. Despite the missing areas, dislocation networks are still well defined. The further development of grain subdivision can also be found.

In the final map (40%) as shown in Figure 6-5 (d), the size of cell arrays is kept almost constant grain to grain, but it is more homogeneous distributed within grains. More grains in this map have developed uniform deformation microstructures and furthermore long range dislocation bands are no longer observed.

At these levels of deformation, significant misorientation present in some grains such that a small fraction of map was not able to be analysed using cross correlation method. By checking the EBSD patterns quality and adding more than one reference points within single grain, the results show that more of these black areas were recovered. Thus the unresolved areas are not just that the patterns are completely blurred out but large misorientation present between the reference patterns and test patterns.

### 6.2.2 Grain orientation and deformation microstructures

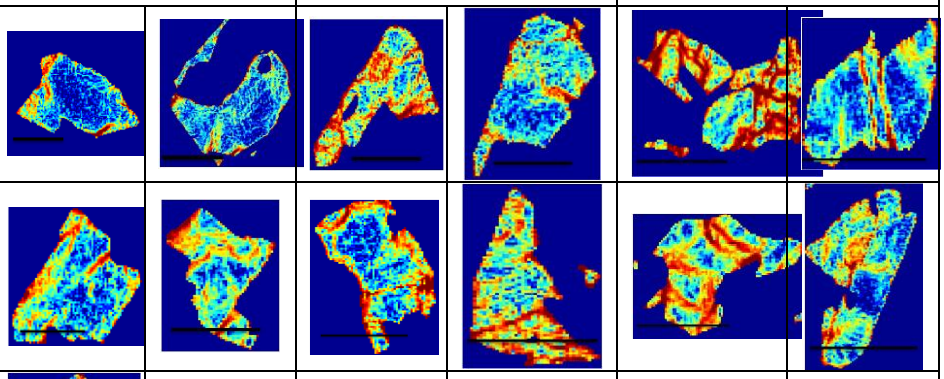
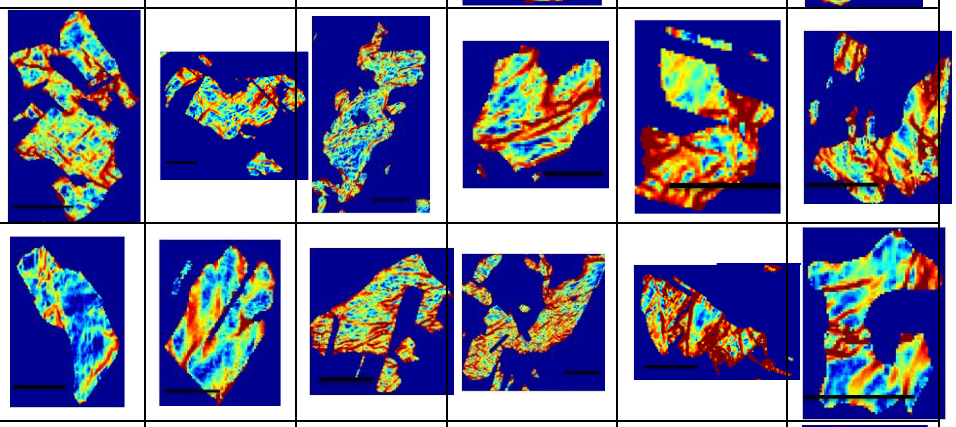
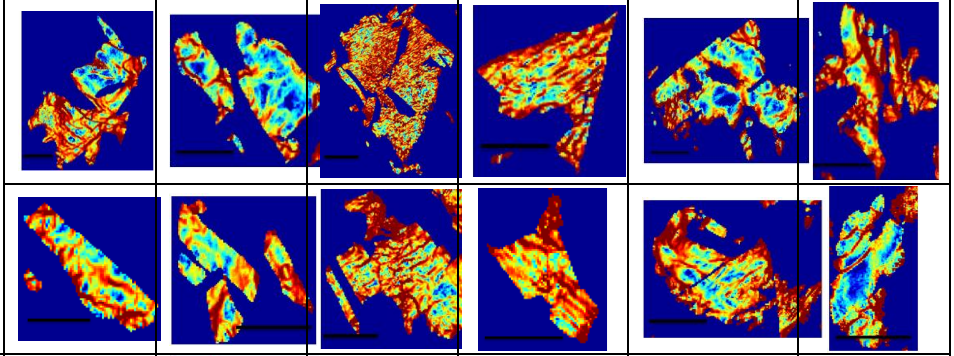
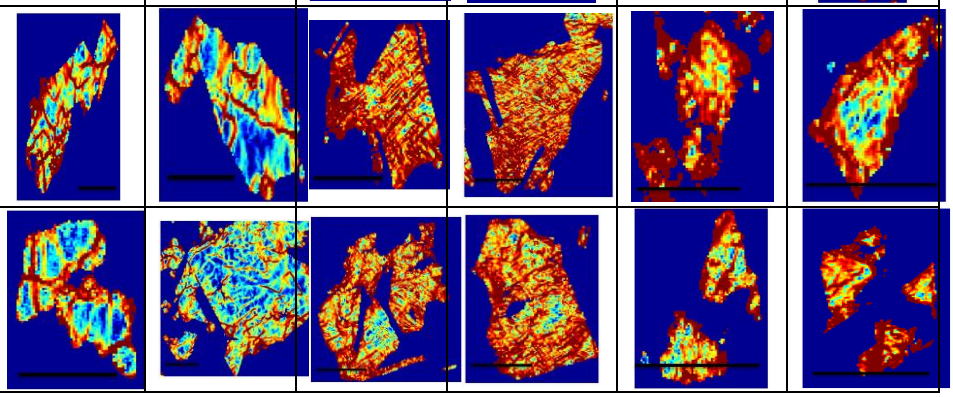
| Orientation / Strain | [001] | | [111] | | [110] | |
|---|---|---|---|---|---|---|
| 6% |  | | | | | |
| 10% |  | | | | | |
| 22.5% |  | | | | | |
| 40% |  | | | | | |

**Table 6-2, for each orientation ([001], [111] and [110]) four different grains were randomly selected at each strain: 6%, 10% 22.5% and 40% to display dislocation structures developed within them. The same colour scale as Figure 6-5 is used at each strain. The scale bar for each figure is 20μm.**

Examples of the dislocation structures formed at various strains in grains of different orientation are shown in Table 6-2. Grains with specific orientations were selected according to Figure 6-2(c). At moderate strains (6% and 10%), dislocation boundaries and cell arrays are formed in all three selected orientations and little morphological difference can be found in all three orientations. Dislocation boundaries are arranged in rather wavy forms in all grains. With further deformation, it is of interest to note that grains with different orientations exhibit distinct dislocation structures. In [111] orientated grains more homogenous, linear and dense dislocation cell arrays are formed and fewer dislocation boundaries are present. However the dislocation boundaries which divide grains into several domains are common features found in [110] grains. Both dislocation cells and dislocation boundaries are presented in [001] grains.

These orientation dependent tendencies seem to become more obvious with increasing strains. More homogenous cell array structures in [111] orientated grains are developed at 40% strain. The size of dislocation cells formed mainly in [100] grains is reduced and more well defined dislocation networks are formed within the grains. Furthermore, the number of [110] grains is reduced significantly due to texture evolution. However the remaining [110] grains show relatively higher grain average dislocation density comparing to [111] and [100] ones and in which GBs become the preferential sites for dislocation accumulation. It should be noted that the number of grains

visually assessed being significantly lower here than the quantitative analysis in the previous chapters.

### 6.2.3 Grain-grain interactions

In this section GND density micrographs of four specific orientations with distinct grain-grain interaction behaviours predicted by the theoretical modelling [80], namely $RZ_{fcc}$, Brass, Goss and Copper are presented in Table 6-3 and Table 6-4.

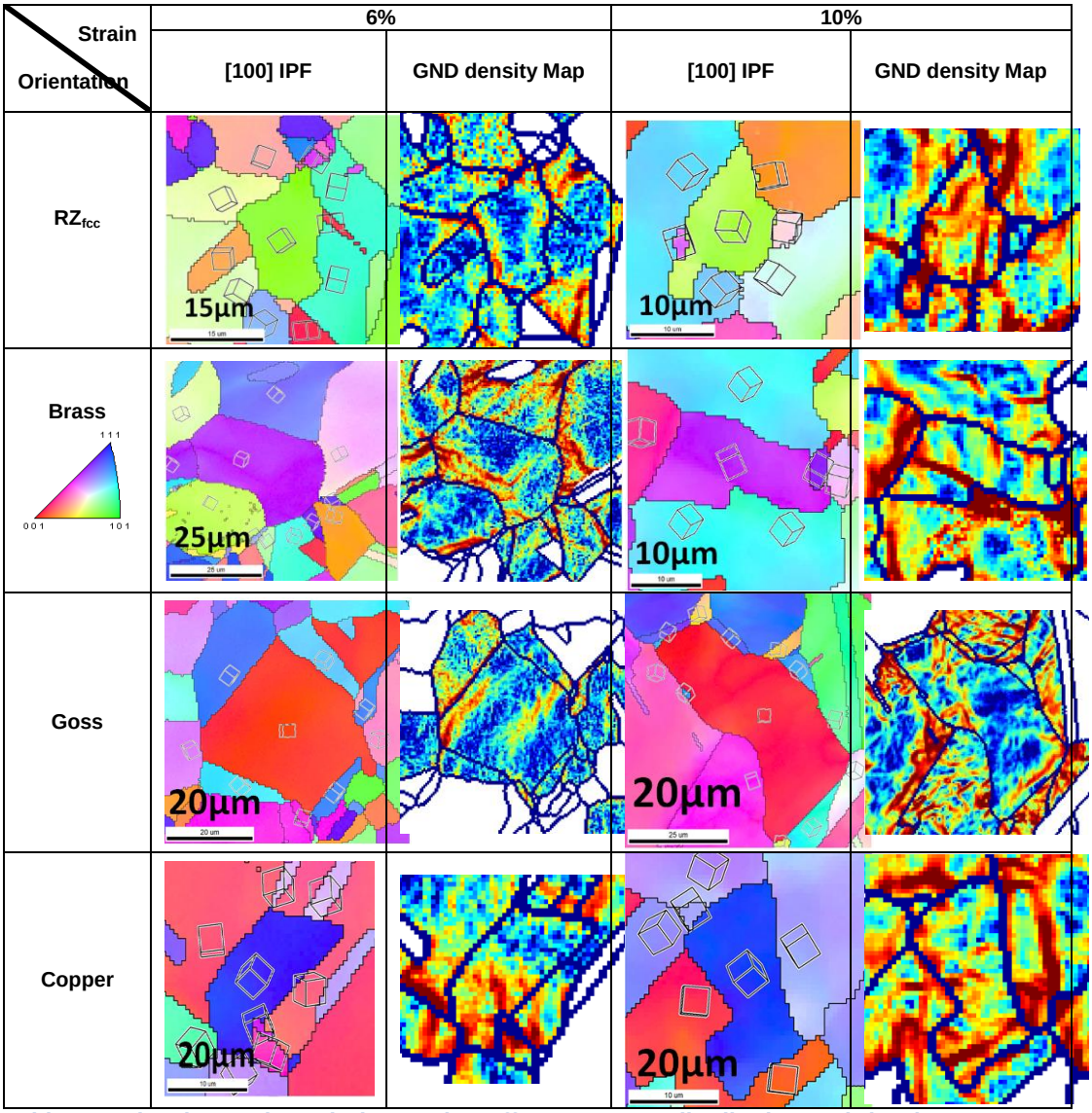



**Table 6-3, showing grain-grain interaction effects on GND distribution and development at 6% and 10% tensile strains; Central grain was one of the four selected orientations (RZfcc, Brass, Goss and Copper). The IPF and GND density maps of the host grain and neighbouring grains were presented. The IPF was generated along the RD as shown along the orientation column in Brass cell and loading axis was aligned along the RD as well. Schematic cubes illustrate the orientation of host grain and neighbouring grains. The black and dark blue lines in IPF and GND density maps are GBs with misorientation angle larger than 7° between adjacent pixels. The colour scale for GND density maps are on $\log_{10}$ scale with unit of $m^{-2}$. To highlight dislocation**

**structure, at each strain, the colour scale is optimised as shown in Figure 6-5. Non-neighbouring grains or those failed to be HR-EBSD derived points are marked as white regions.**

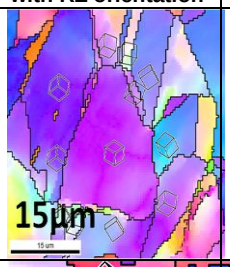
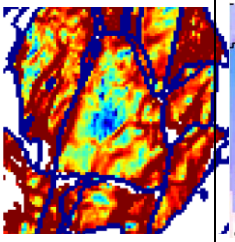
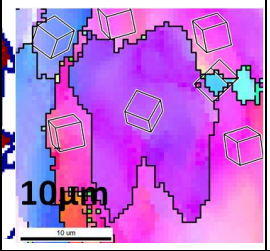
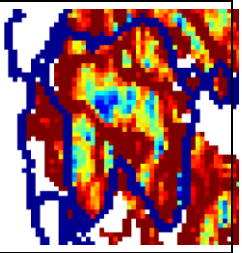
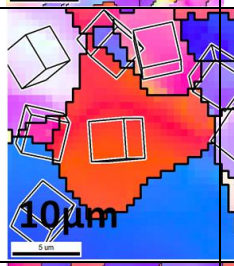
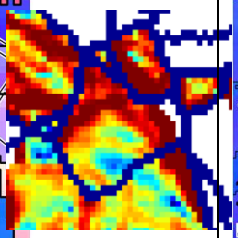
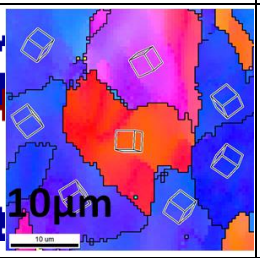
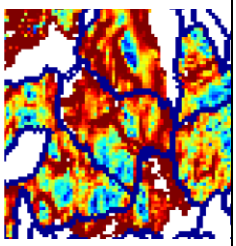
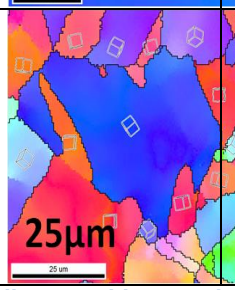
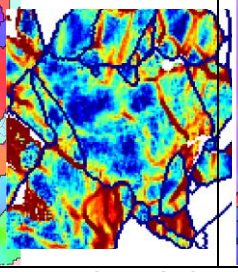
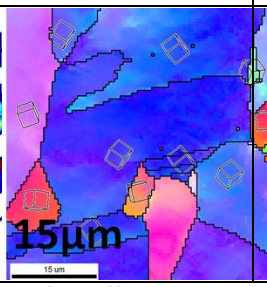
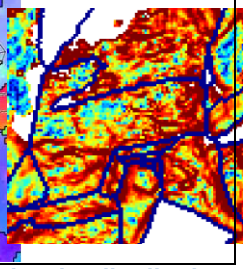
| Strain / Orientations | 22.5% | | 40% | |
|---|---|---|---|---|
| | [100] IPF | GND density Map | [100] IPF | GND density Map |
| $RZ_{fcc}$ | No grains observed in maps with RZ orientation | No grains observed in maps with RZ orientation | No grains observed in maps with RZ orientation | No grains observed in maps with RZ orientation |
| Brass |   |  |   |  |
| Goss |   |  |   |  |
| Copper |   |  |   |  |

**Table 6-4, similar to Table 6-3 shows grain-grain interaction effect on GND density distribution and evolution but at 22.5% and 40% tensile strains.**

In the preceding subsection, in the highly deformed samples strong dislocation structure dependences on grain orientations were reported. However, Inspecting GND density maps in Table 6-3 and Table 6-4, it is found that grains do not deform independently. Instead, all grains were strongly affected by their adjacent grains. Dislocation bands (dislocation boundaries) are the most common features presenting in all maps. These bands are rarely constrained within a single grain at all strains. They tend to run through neighbouring grains or join the dislocation network at TJs regardless of host grain orientation or neighbouring grain orientations. The Brass and Copper orientation grains are expected from Raabe's kinematic stability analysis to have rather isolated dislocation structure development

tendency from their neighbours. However, dislocation bands are still found to connect to the dislocation networks in their surrounding grains. Of course the neighbour grain structures could be changing to match in with the Brass and Copper grains.

### 6.2.4 Annealing twins

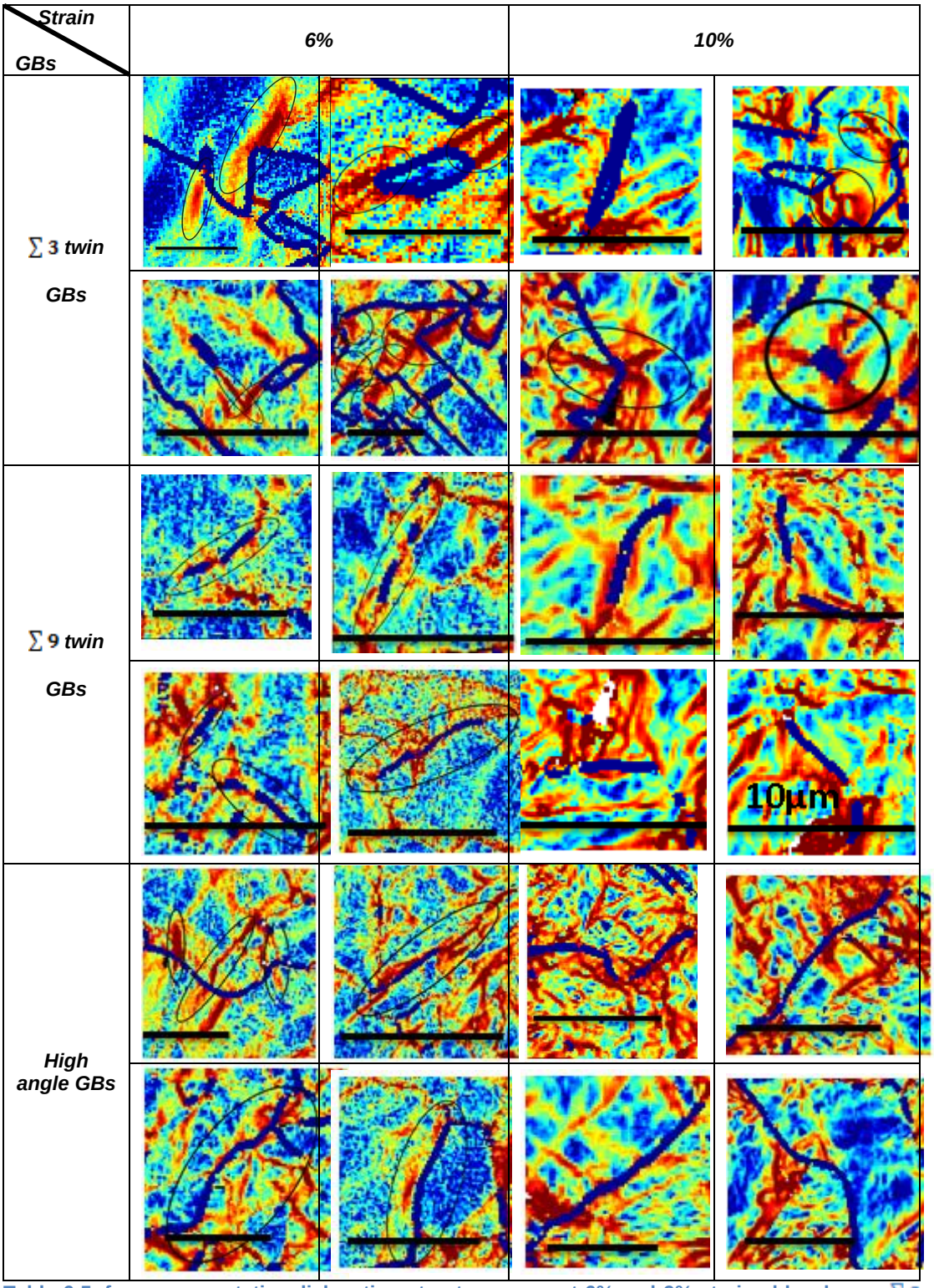



Table 6-5, four representative dislocation structure maps at 6% and 9% strained levels near∑3, ∑9 and high angle GBs are selected from various places in the large 500 μm x500 μm GND density maps. Dark blue lines represent the GBs. The colour axes for all GND density maps are kept the same as Figure 6-5. White regions are points that were failed to be recovered during cross-correlation process. For each row of the table only specified GBs are showing. The black lines show 20μm scale bar. For figures less than 20 μm, the scale bar is specified in the figure.

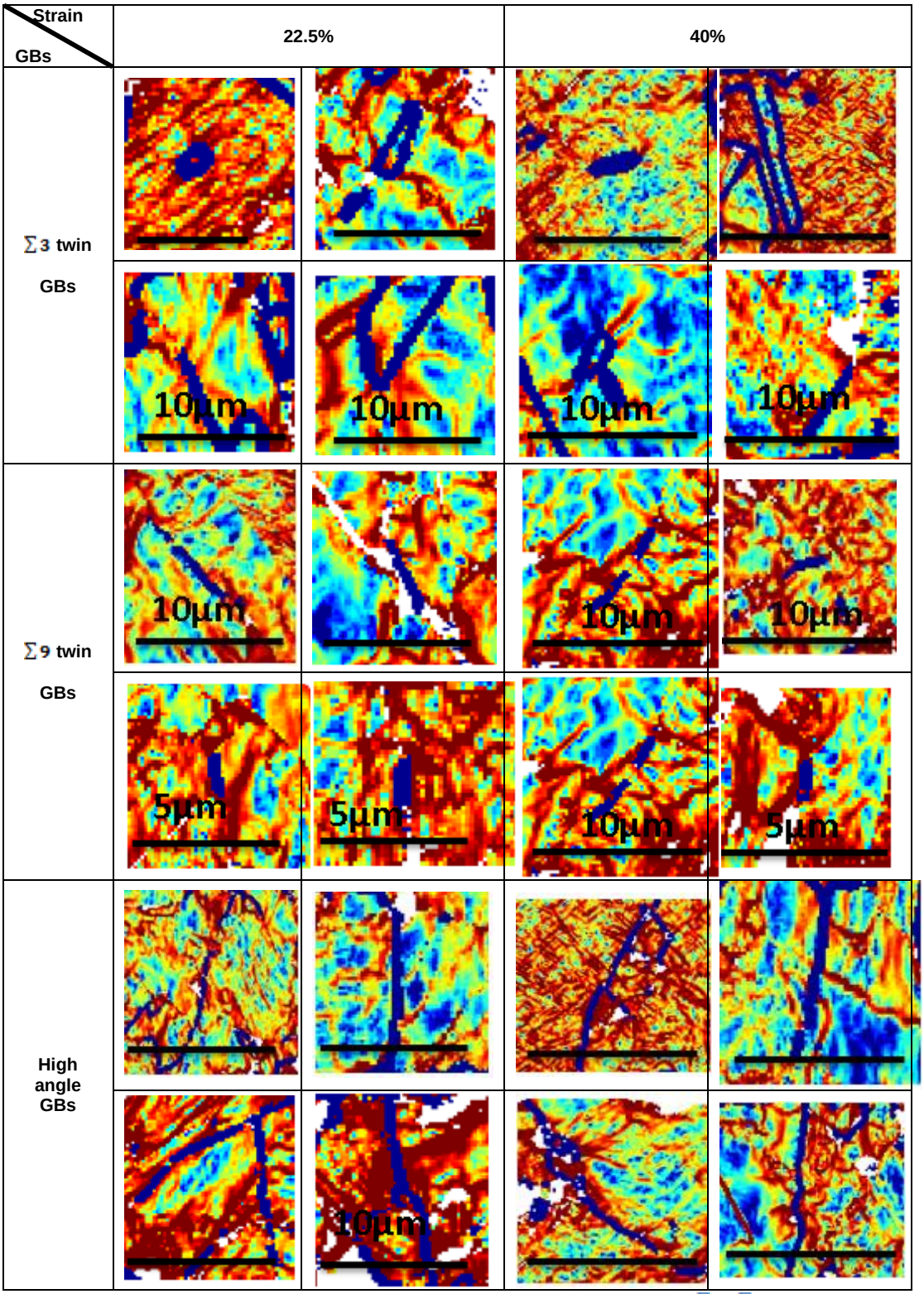



Table 6-6, is similar to Table 6-5 showing the dislocation structure near∑3, ∑9 and high angle GBs at 22.5% and 40% strain levels. The black lines show 20μm scale bar. For figures less than 20 μm, the scale bar is specified in the figure.

Table 6-5 and Table 6-6 show dislocation structures development near∑3, ∑9 and high angle GBs. The dislocation boundaries often connect to the tips

of small $\Sigma 3$ grains which are embedded in some large grains. Sharp corners of large $\Sigma 3$ GBs are also favourable sites for dislocation boundaries to connect.

Several dislocation boundaries are linked to these tips and sharp corners and radiate out in various directions.

With increasing deformation, more homogenous dislocation structures emerged in some grains as shown in Figure 6-5. Grain orientations started to play an important role to determine the dislocation structures around $\Sigma 3$ GBs (see Table 6-6). If $\Sigma 3$ GBs are contained within a cell structured grain, rather uniform dislocation structures are developed around them. However, $\Sigma 3$ GBs still act as dislocation boundary terminals where dislocation boundaries intersect.

In 2D space, it is rather difficult to separate the different influences to draw any conclusions. At moderate strains (6% and 10%), dislocation boundaries prone to develop along $\Sigma 9$ GBs. However this may be a coincidence as the few excising $\Sigma 9$ GBs are oriented approximately 45° to the loading axis for which generally dislocation boundaries tend to point along that direction as well.

No consistent dislocation structure development dependence was found near high angle GBs. Both high and low dislocation density patterns are present

near high angle GBs. If dislocation boundaries are not aligned with high angle GBs, it is noted that the continuity of dislocation boundaries are often maintained spanning across the high angle GBs.

### 6.2.5 Triple junctions

| | | | | | | | |
|---|---|---|---|---|---|---|---|
| | $\Sigma 3, \Sigma 3, \Sigma 3$ | $\Sigma 9, \Sigma 9, \Sigma 9$ | $\Sigma 3, \Sigma 9, \Sigma 9$ Or $\Sigma 3, \Sigma 3, \Sigma 9$ | HA, $\Sigma 3, \Sigma 9$ | HA, $\Sigma 3, \Sigma 3$ Or HA,HA, $\Sigma 3$ | HA, $\Sigma 9, \Sigma 9$ Or HA,HA, $\Sigma 9$ | HA,HA, HA |
| | 333 | 999 | 390 | 39H | 3H0 | 9H0 | HHH |
| | 482 | 21 | 4976 | 8158 | 13160 | 1297 | 1107 |
| | 679 | 0 | 3177 | 7691 | 16701 | 1309 | 1282 |
| | 305 | 10 | 637 | 3823 | 13189 | 1145 | 2158 |
| | 225 | 0 | 263 | 2971 | 10024 | 1448 | 2755 |

**Table 6-7, the classified TJs consist of various set of constitutional GBs. HA is used to represent the high angle GBs. The abbreviations and the number of TJs found for each type of TJs that are used in the later figures are also shown.**

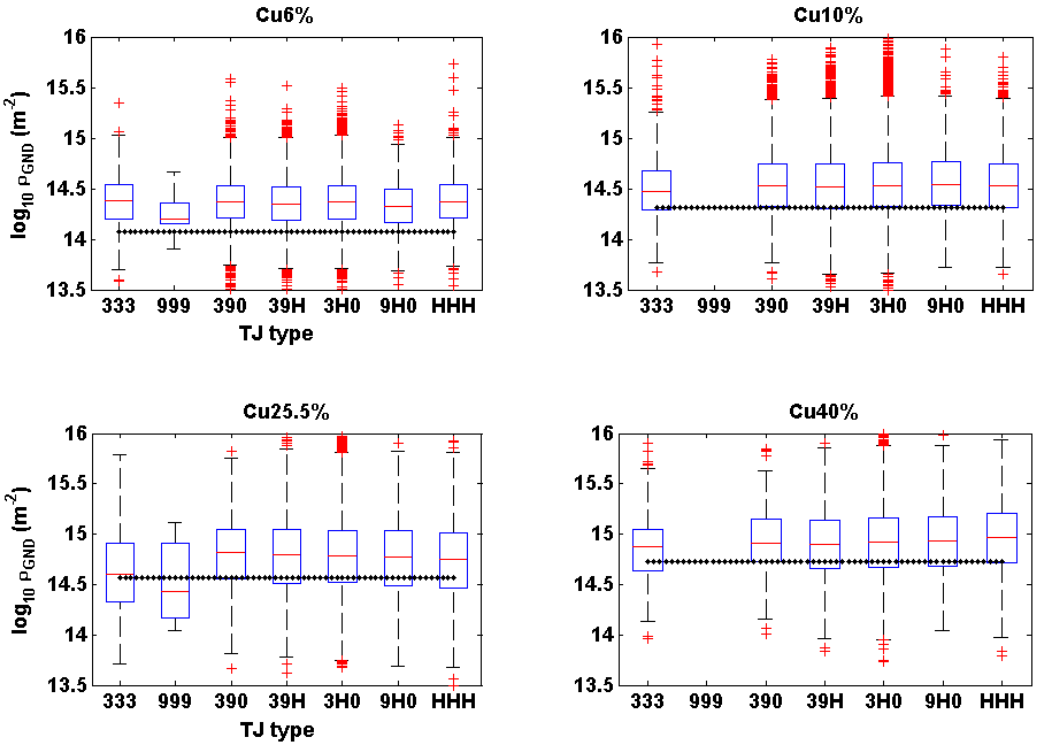



**Figure 6-6, in each box plot the general dislocation density distributions near different TJ types are presented. The general evolution of dislocation density near different TJ types as a function of plastic strain level is also shown. The TJ abbreviations are used to label x axis. The details of TJ types and the number of TJs can be referred to Table 6-7. On each box the central mark is the median value and the edges of the blue box are the 25$^{th}$ and 75$^{th}$ percentiles. The whiskers describe approximately +or – 2.7 times standard deviation, any point beyond this range is considered as outliers. The dotted black line in each plot indicates the magnitude of map averaged dislocation density.**

In Chapter 4. , it is found that the GND density near TJs was found to be higher than the average value in all samples. Depending on the constitutional GBs, seven types of TJs were classified and the corresponding dislocations structures were systematically analysed (Figure 6-6). Note that due to the low fraction of $\sum 9$ twin GBs, the number of related TJs is also low especially for the TJs formed by three $\sum 9$ GBs. This is the reason why no 999 TJs results are shown in 10%, 25.5% and 40% strained samples.

In general, there are relatively small variations on a log axis between different types of TJs. However systematic tendencies can still be observed. It seems that twin boundaries formed TJs such as 333, 999 and 390 are slightly less

favourable for dislocations to pile up. Although in 6% strained sample the 333 TJ is an exception, the lowest median values in all four samples are all found in twin boundary formed TJs. In 22.5% strained sample, there is marked dislocation density drop in 333 TJs comparing to other TJs. In contrast the TJs consisting of high angle GBs (HHH, 3H0 and 9H0) seem to be slightly more favourable ones for dislocations to pile up. Comparing to other TJs, the HHH TJs have the highest dislocation density around them.

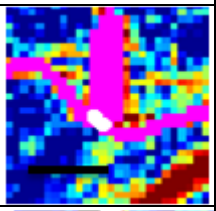
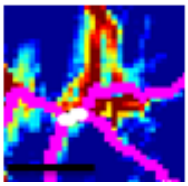
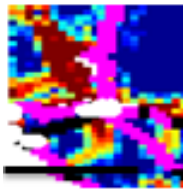
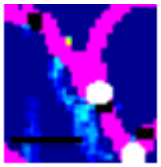
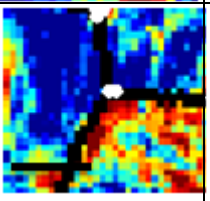
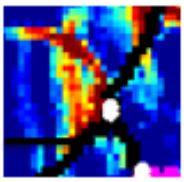
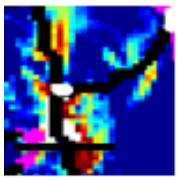
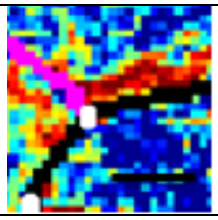
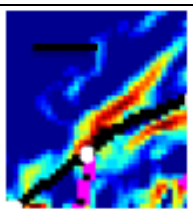
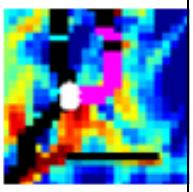
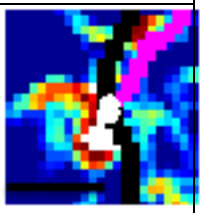
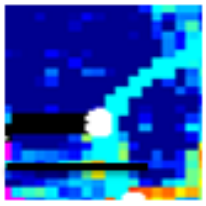
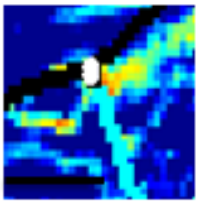
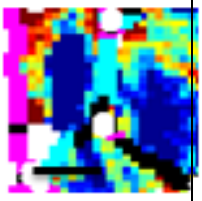
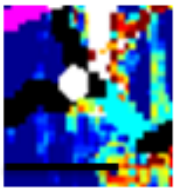
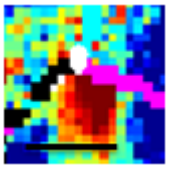
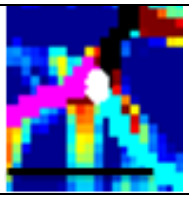
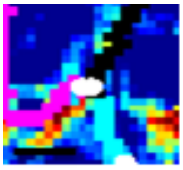
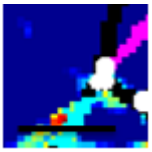
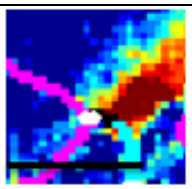
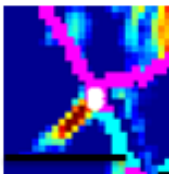
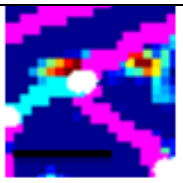
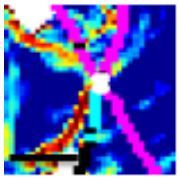
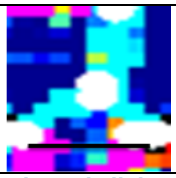
| Strain / TJ Types | 6% | 10% | 22.5% | 40% |
|---|---|---|---|---|
| 333 |  |  |  |  |
| HHH |  |  |  |  |
| 3H0 |  |  |  |  |
| 9H0 |  |  |  |  |
| 39H |  |  |  |  |
| 390 |  |  |  |  |
| 999 |  | No such TJs observed in maps | | |

**Table 6-8, shows selected dislocation structures near various types of TJs at different strain levels. Black lines indicate high angle GBs; magenta lines represent $\sum 3$ twin boundaries and cyan lines are used to show $\sum 9$ twin boundaries. White circles denote the locations of TJs. Pixel size in all maps is 0.5 µm. For each map the colour scale is adjusted to highlight the high density dislocation structures.**

Qualitative analysis is conducted in parallel to the quantitative analysis to reveal the dislocation structures adjacent to various types of TJs. One TJ for

each type at each strain level was selected and overlapped with dislocation arrangements near it (see Table 6-8). Due to the large scatter of dislocation density near TJs as shown in Figure 6-6, the selected TJs can not be fully representative. At each strain level, some TJs do not manifest as special sites for high dislocation density to accumulate and hence no dislocation structure can be found near them. Furthermore, at 22.5% and 40% strain, due to the presence of large lattice rotation, the cross-correlation method was not able to recover dislocation structures for all probed points such that the high density structure developed near TJs are often inaccessible. However, micrographs shown in Table 6-8 allow general visual inspections on dislocation arrangements which could complement the obtained quantitative analysis (Figure 6-6).

Minimal difference can be observed in various types of TJs or in different strain levels. In general, most TJs act as 'hot' spots to accumulate dislocations. However, instead of forming a circular shape, it is found that dislocations tend to pile up on single side of TJs as seen very clearly in HHH 40% micrograph in Table 6-8. The TJs seem to act as dislocation boundary terminals. These dislocation boundaries tend to bridge across a grain between two TJs or a TJ and a sharp corner of $\sum 3$ twin boundaries.

Multiple dislocation boundaries within the same grain or in two or more grains are often joined up at TJs. These dislocation boundaries do not always follow the traces of GBs. Instead, they span over entire grains and so subdivide grains into a number of dislocation cells.

It is rather rare to observe two dislocation boundaries from different grains are aligned and intersected at TJs. Typically, those joined dislocation boundaries point to distinct directions when crystal orientation changes.

A comet-tail-like shaped dislocation formation can also be found such as the 390 TJ at 10% in Table 6-8.

## 6.3 Discussion

### 6.3.1 Characteristic deformation microstructures

As discussed in Chapter 2. , the TEM method is capable of charactering all dislocations due to its ultrafine spatial and angular resolution. Prior to the emergence of EBSD, virtually all detailed quantitative investigations of deformation microstructures were carried out by TEM. However the main drawback of TEM is the localised probing area. A systematic comparison for analysing deformation structures in FCC materials using TEM and Hough based EBSD has been carried out by Mishin et al [127]. They showed that due to the relatively low angular resolution Hough-based EBSD technique is not able to probe all deformation microstructural characteristics e.g. low angle misorientation dislocation boundaries. The HR-EBSD derived dislocation density maps clearly revealed most of the characteristic dislocation structures reported in the literature such as dislocation cells, microbands, shear bands and 'herring bone' dislocation network. Clearly larger areas have been mapped in this study than is possible in TEM work. Areas from these maps where analysed primarily qualitatively to understand the morphological relationship between dislocation network structure and microstructure. Their developments with increasing strain are also in a good agreement to TEM observations.

These studies extend previous observations significantly, as most existing studies focus only on selected grain boundary combinations, due to the difficulties of TEM based observation. Even in examining dislocations in

polycrystals, focus was directed on the structure within grain interiors rather than in relation to the local grain neighbourhood [181]. How a host grain interacts with its neighbouring grains in order to main geometrical compatibility is proved to be a very important factor to determine dislocation structures [3] but it has not been well captured by TEM. To author's knowledge, it is the first time that the dislocation structures in both individual grain and the grain neighbourhood were mapped. This allowed us to conduct detailed analysis on grain-grain interaction and orientation dependence.

### 6.3.2 Grain orientation dependence

Previous analysis (Chapter 5. ) demonstrated that the grain averaged GND density as a function of crystal orientation did not yield any significant variation within the quantitative analysis, which is likely due to the vast number of potential variables and therefore the complex parameter space. Here qualitative assessments of local orientation selected from the large maps reveal that the development of dislocation network morphology depends on grain orientation. More homogenous cell arrays were formed in [111] grains whereas in [001] and [110] grains larger dislocation cells were commonly observed features. This is in support with Raabe's model [80]. In their model [011] grains have pronounced kinematical instability and significant dependence to form heterogeneous deformation on the neighbouring grains whereas the [111] grains are most kinematically stable and have the lowest tendency to form heterogeneous deformation structure. Raabe et al [80] model also showed that [111] oriented grains have low tendency to form heterogeneous dislocation structures but they are strongly

affected by neighbouring grains. This might explain the observed dislocation boundaries present in [111] grains in the maps.

However the observed dislocation structures are in contrast with TEM observations made by Huang et al [93]. They reported that in more homogenous equiaxed dislocation cell structures tended to be generated in [001] grains rather than larger scale dislocation boundaries in polycrystal copper under tension. This observation coincides with other TEM observations made in single crystal copper with [001] orientation [182, 183]. However, in Huang's TEM measurements, only dislocation boundary free regions were characterised. "In some grains, large grain orientation gradients were found over a long distance. In this case, the structural analysis was made for different regions within the grain." Large grain orientation gradients (dislocation boundaries in my case) regions were excluded from their measurements. Therefore some important features might have been missed in Huang's study.

From the evolution of dislocation structure with increasing strain (see Table 6-2), mechanisms of dislocation structure development might be deduced. At low or moderate strain, to maintain the compatibility condition dislocation arrangements in individual grain are strongly influenced by its neighbouring grains. This can explain why at 6% strain more heterogeneous deformation structures are formed in all orientations.

As the imposed plastic deformation level increases, there are more dislocations stored in grains. It seems that the general development tendency is to reduce the heterogeneity generated from different orientations

and to form a more uniform dislocation structure. In order to accommodate the abrupt orientation difference between grains, [001] and [110] grains are further subdivided into smaller dislocation cells.

As seen from texture measurements in Chapter 5. , [001] and [110] are metastable orientations during deformation. With increasing strain, they generally tend to rotate toward [111] orientation. Presumably, in this process the dislocation cells were subsequently divided into even smaller dislocation cells. Eventually more homogenous dislocation cell arrays are formed in these newly developed [111] grains. This may explain why in highly deformed sample more homogenous dislocation cell arrays are present in [111] grains and also the existence of transition structure (from large dislocation cell structure to more regular cell structure) in highly deformed [001] grains.

### 6.3.3 Grain-grain interactions

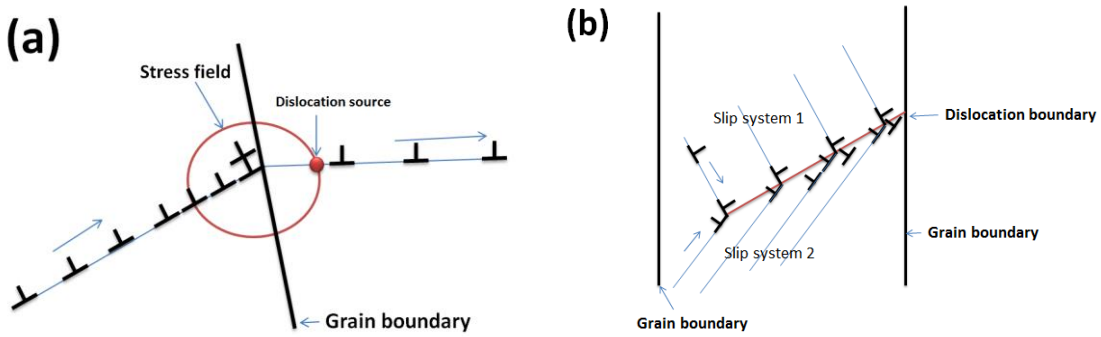



**Figure 6-7, diagrams show the two proposed dislocation boundary formation mechanisms. In (a) dislocations are stored and piled up along slip lines and so the pile up initiates dislocation source in the neighbouring grains. In (b), dislocation storages are due to the intersection of different slip systems.**

In Table 6-3 and Table 6-4, it was found that the development of dislocation networks is not isolated within single grains. Dislocation boundaries tend to span across GBs and connect to the dislocation boundaries formed in neighbouring grains. Assuming the dislocation storage is mainly along

dislocation bands, the connected dislocation boundaries may be caused by the high stress field generated by dislocation pile up at the GBs as Britton et al observed in Titanium[136]. Once the stress at the grain boundary reaches the critical resolved shear stress of the neighbouring grain, slip in the neighbouring grain can be initiated and it results in a connected dislocation boundary (see Figure 6-7 (a)). However, dislocation activities are rather complicated in the moderately deformed polycrystals where multiple slip systems are activated. As observed that grain tend to form sub-domains within which independent slip systems are active. The second mechanism of dislocation boundary formation is proposed as a result of the intersection between different slips systems within a grain (see Figure 6-7(b)). The tendency of forming a dislocation network seems independent of grain orientations and strain levels. This tendency is more pronounced in low and moderately deformed samples. Although in highly deformed sample more homogenous dislocation structures developed in grains with Copper orientation, the influence of dislocation boundaries from neighbouring grain is still traceable.

These experimental observations do not completely agree with Raabe's prediction on grain-grain interaction in which Brass and Copper orientations were predicted to have marked weaker dependence on their neighbouring grains comparing to RZfcc, Goss. This may due to the assumption made in their model that uniform stress field across GBs. In practice, in Quantitative Analyses on GND Density Distributions and Evolution (I)Chapter 4. It was found that highly heterogeneous dislocation structures are observed adjacent

to GBs and magnitude stress field arising from these dislocation structures is significantly high than low dislocation density regions.

Several attempts have been made using conventional EBSD to study the GND behaviours in deformed polycrystals [45, 184]. Although they concluded that grain-grain interaction is an important factor in determining the final GND arrangements, both theoretical mechanisms and experimental evidence were absent.

### 6.3.4 Twin boundaries

Current results show that the $\sum 3$ annealing twins manifested interesting characters to affect dislocation structures in polycrystal copper. Dislocation boundaries tend to end up at $\sum 3$ annealing twins especially at tips or sharp corners. These observations provide experimental evidences to confirm that $\sum 3$ boundaries are very effective obstacles to dislocation movement [185-188]. In other words dislocations hardly pass $\sum 3$ twins boundaries.

One explanation is that if a $\sum 3$ twin is embedded in a large grain, homogenous dislocation slip is inhibited near twin boundary and hence dislocations start to accumulate. The subsequent gliding dislocations are stacked up to form a dislocation boundary (similar to Figure 6-7(a)). $\sum 3$ twin boundaries are hence often found to be the initiation sites for dislocation boundaries. Furthermore, if this accumulation mechanism is correct the 'hot' end of the dislocation boundary should appear at the intersection point with

the twin boundary. This agrees well with our observations. This explains why cracks are difficult to penetrate through $\sum 3$ twin boundaries.

Nevertheless as we only observed the post deformation maps, another possible explanation for observations dislocation structures around $\sum 3$ twin boundaries is that as TEM observed [187, 189] annealing twins emit dislocations as dislocation sources. The twin emitted dislocations may interact with gliding dislocations in the matrix and entangled together to form the observed dislocation boundaries. The exact mechanisms cannot be identified unless in situ tests are carried out in TEM.

As the probability of finding $\sum 3$ twins is significantly higher $\sum 9$ twins, it is difficult to make a direct comparison with $\sum 9$ twins.

### 6.3.5 Triple junctions

Similar to $\sum 3$ twin boundaries, in the maps TJ were also found to be favourable dislocation accumulation sites where dislocation boundaries initiate. A comet-tail-like shaped dislocation formation can also be found such as the 390 TJ at 10% in Table 6-8. This kind of dislocation formation seems like immature form of dislocation boundaries.

No evidence suggests triple junction are active dislocation sources or effect dislocation motion obstacles, although during annealing process TJs were found to be recrystallization nucleation sites due to high stored energy [163]. The possible mechanism to form such dislocation boundaries is thought to be

due to grain-grain interactions. It is well known that relatively homogenous slip activities occur in the interiors of individual grains. Slip systems change near GBs. This slip system change may result in a transition zone. Dislocations from different sets of active slip systems may be entangled to form dislocation boundaries. Grains are thus subdivided into several domains with different orientations. If the proposed mechanism is true, then TJs should be the sites to initiate dislocation boundaries. The obtained observations indeed support this model. Furthermore the directions of dislocation boundaries are found to extend one of the three constitutional GBs. This may give indication of which one of the two neighbouring grain have stronger effect on host grains.

Investigating dislocation accumulation at various triple junction types showed some variations between different types of TJs. This implies that there is some influences of TJ type but it is not the only aspect (alignment of the three boundaries with the load axis and many other parameters could play a role) to determine the dislocation structure developed near them. Probably the grain-grain interactions play a more significant role here.

## 6.4 Conclusion

Qualitative analyses on HR-EBSD derived dislocation structure were conducted in this chapter. A general comparison between obtained dislocation structures with TEM characteristic observation was made. Also dislocation structures developed near a number of microstructural features such as orientation, grain-grain interactions, twin boundaries and TJs were visually assessed. The following conclusion can be draw:

1. Typical TEM observed dislocation structures such as dislocation cells, boundaries, bands and networks are also found in HR-EBSD derived dislocation density maps.
2. Dislocation structures have strong dependence on grain orientations although the average dislocation density does not. In moderate and highly deformed samples, more homogenous cell arrays are formed in [111] grains whereas dislocation boundaries are generated in [001] and [110] grains.
3. Grain-grain interactions played a significant role in dislocation structure development. Irrespective of orientations and strain levels, all grains demonstrated a pronounced dependence tendency on neighbouring grain.
4. $\sum 3$ twin boundaries showed marked difference from high angle GBs. Dislocation boundaries tend to initiate from the tips and sharp corners of $\sum 3$ twin boundaries. $\sum 3$ twin boundaries are effective sources to promote the occurrences of grain subdivision.

5. Some variation in dislocation density was observed between different types of triple junctions. $\sum 3$ twin boundaries formed triple junctions have the lowest dislocation density while high angle boundaries composed triple junctions have the highest dislocation density.
6. Triple junctions act as favourite dislocation boundaries initiation points. It is proposed due to the neighbouring grain effects.

# Chapter 7. Summary

This thesis has comprehensively studied the lower bound GND density distribution and evolution in progressively tensile deformed polycrystalline copper samples at room temperature by using the newly developed HR-EBSD technique.

Firstly a single crystal silicon sample with few stored dislocation has been used to explore the sensitivity of the HR-EBSD technique in GND density measurement with various step size and detector binning levels. The sensitivity of GND measurement has been found to decrease with increasing detector binning levels and decreasing step sizes. However the increasing binning level and decreasing step size enlarge the size of EBSD probed area within limited mapping time. By balancing GND measurement sensitivity and size of sampling area, an optimum setting with the step size of 0.5μm and the binning level of 4x4 for copper sample has been found. The GND density measurement noise level for these settings was estimated as ~$5.6 \times 10^{12}$ $m^{-2}$. Also the HDF5 file storage method has been employed to save all EBSD pattern images such that in each EBSD map all associated EBSD pattern images can be stored in a single file which allows large number of EBSD patterns (>1million) to be stored with significant improvement in data transfer speed. Therefore HR-EBSD technique has been successfully developed to extend it applications from maps containing less than 30 grains to more statistically relevant maps (>1000 grains).

The improvement of the HR-EBSD technique has allowed quantitative GND density analysis to be conducted. Five OFHC polycrystalline copper samples

with average grain diameter of 10.5 μm were uniaxially deformed to tensile strains of 0%, 6%, 10%, 25.5% and 40%. The step size of 0.5μm and 4x4 binning level have been used to collect 500μm x500μm EBSD map on each sample. From the statistical analyses, it has been found that the map averaged GND density increased with the increasing plastic strain. A good agreement between the experimental stress strain curve and the predicted stress strain curve based on Ashby hardening model has been found. This implies GND density may be used as a single parameter to represent the plastic deformation state. Furthermore, the general distribution of GND density has been found to be best described by Log-normal distribution function. These statistical analyse have extended our current understanding in the GNDs' general behaviours. The obtained experimental results will greatly benefit the plasticity modelling community by validating their simulation results.

Detailed and systematic studies to correlate GND density distribution and evolution with crystallographic features have also been carried out. Grain boundaries and triple junctions have been identified as favourite sites for GNDs to accumulate. High GND density was found near grain boundaries and the low GND density tended to appear in the grains' interiors. This tendency is particularly obvious in the annealed and moderately deformed samples. By investigating the grain averaged GND density and grain size, it has been found that this relation in fact provides direct experimental evidence to rationalise the empirical based Hall-patch relation. This tendency gradually decreased with the increasing plastic strain. These have been further studies by direct visual assessment on GND structures. From the observations made

on GND structure evolution, it has been found that the initial heterogeneous GND structures (e.g. dislocation boundaries) were evolved into a more uniform GND structure (regular cell arrays). This has explained the reduced GND density tendency to accumulate near grain boundaries. However points with high GND density invariably appear near triple junctions. Triple junctions have been observed as dislocation boundaries intersection points. Evidence of some comet-tail-like shaped dislocation structures have been observed near triple junctions, such that the triple junctions seemed to be dislocation boundary nucleation sites. It has been proposed that dislocation boundaries intersection at triple junctions was due to grain-grain interaction effects.

More detailed assessments have been conducted on GND density with grain boundaries and triple junctions such as the grain boundary disorientation angle, grain boundary inclination angle with respect to loading axis and the constitution of triple junctions. Relatively weak correlations have been found between GND density and these features.

The dependence of GND density on grain orientation has been examined. Distinct dislocation structure development in various grain orientations has been observed. For example, dislocation boundaries have been observed in grains with [001] and [110] orientations and regular cells have been formed in [111] grains. Note that these indices are defined with respect to the loading direction. However no correlation was found in statistical analysis between grain averaged GND density and grain orientation.

GND structures near twin boundaries have been also examined. Twin boundaries have been found to be prohibitive for dislocations to pass.

Comet-tail-like shaped dislocation boundaries have also been observed near the tips and sharp corners of twin boundaries. Therefore twin boundaries seem to be dislocation nucleation sites.

Based on the obtained observations, single slip dislocations pile up and the intersection of multi slip systems have been proposed to be two possible mechanisms for forming dislocation boundaries.

This thesis has demonstrated that how polycrystals accommodate the imposed plastic deformation is a complex problem. It is not predominately influenced by any single microstructural aspect. The final heterogeneous deformation structures are due to the contributions from many microstructural parameters, which reduce the impact of any single parameter examined in isolation.

The development of HR-EBSD has demonstrated its increasing strength on studying deformation problems in polycrystals by providing significantly richer information on dislocation structures and crystallographic information than these obtained from conventional TEM and X-ray measurements. More insights have been provided on fundamental dislocation plasticity studies. This is important to further understand and solve materials problem used in real engineering applications. HR-EBSD has emerged as a powerful dislocation structure characterisation tool to study deformation problems and has started to make significant impact on this research field.

# References

[1] Ashby M. Philosophical Magazine 1970;21:399.
[2] Kocks U, Mecking H. Progress in Materials Science 2003;48:171.
[3] Taylor G. Proceedings of the Royal Society of London. Series A, Containing Papers of a Mathematical and Physical Character 1934;145:362.
[4] Bishop J, Hill R. Philosophical Magazine 1951;42:414.
[5] Kocks U. Acta Metallurgica 1958;6:85.
[6] Kelly A, Nicholson R. Strengthening methods in crystals: Halstead Press Division, Wiley, 1972.
[7] Hull D, Bacon DJ. Introduction to dislocations. Amsterdam ; London: Elsevier Butterworth-Heinemann, 2011.
[8] Bay B, Hansen N, Kuhlmann-Wilsdorf D. Materials Science and Engineering: A 1989;113:385.
[9] Larson B, Yang W, Ice G, Budai J, Tischler J. Nature 2002;415:887.
[10] Jakobsen B, Poulsen HF, Lienert U, Almer J, Shastri SD, Sørensen HO, Gundlach C, Pantleon W. Science 2006;312:889.
[11] Pantleon W, Wejdemann C, Jakobsen B, Lienert U, Poulsen HF. Materials Science and Engineering: A 2009;524:55.
[12] Hefferan C, Li S, Lind J, Lienert U, Rollett A, Wynblatt P, Suter R. Computers, Materials, & Continua 2010;14:209.
[13] Nye J. Acta metallurgica 1953;1:153.
[14] Pantleon W. Scripta Materialia 2008;58:994.
[15] Wilkinson AJ, Randman D. Philosophical Magazine 2010;90:1159.
[16] Dingley D. Journal of Microscopy 2004;213:214.
[17] Lassen NCK. Journal of Microscopy 1998;190:375.
[18] Wright SI. Journal of Computer-Assisted Microscopy (USA). Vol. 5, no. 3, pp. 207-221. 1993;Vol. 5:pp. 207.
[19] Humphreys FJ. Scripta Materialia 2004;51:771.
[20] Wilkinson A, Randman D. Philosophical Magazine 2010;90:1159.
[21] Wilkinson AJ, Meaden G, Dingley DJ. Ultramicroscopy 2006;106:307.
[22] Wilkinson AJ, Meaden G, Dingley DJ. Materials Science and Technology 2006;22:1271.
[23] Adams BLG, C.J.; Fullwood, D.T. Diffusion and Defect Data Part B (Solid State Phenomena) 2010;160:3.
[24] Vaudin MD, Gerbig YB, Stranick SJ, Cook RF. Applied Physics Letters 2008;93:193116.
[25] Britton TB, Liang H, Dunne FPE, Wilkinson aJ. Proceedings of the Royal Society A: Mathematical, Physical and Engineering Sciences 2009;466:695.
[26] Villert S, Maurice C, Wyon C, Fortunier R. Journal of microscopy 2009;233:290.
[27] Wilkinson AJ, Randman D. Philosophical Magazine 2010;90:1159.
[28] Karamched PS, Wilkinson AJ. ACTA MATERIALIA 2010.
[29] Littlewood PD, Britton TB, Wilkinson AJ. Acta Materialia 2011;59:6489.
[30] Britton TB, Wilkinson AJ. Acta Materialia accepted for publication.
[31] Britton TB, Birosca S, Preuss M, Wilkinson AJ. Scripta Materialia 2010;62:639.
[32] Fang TH, Chang WJ. Microelectronic engineering 2003;65:231.
[33] Staker M, Holt D. Acta metallurgica 1972;20:569.
[34] Doherty R, Hughes D, Humphreys F, Jonas J, Jensen DJ, Kassner M, King W, McNelley T, McQueen H, Rollett A. Materials Science and Engineering: A 1997;238:219.
[35] Ralph B, Barlow C, Ecob N. RELATIONSHIPS BETWEEN GRAIN BOUNDARY STRUCTURE AND MATERIAL PROPERTIES. Proceedings of the annual meeting, 1980. p.366.

[36] Wyrzykowski J, Grabski M. Philosophical Magazine A 1986;53:505.
[37] Lim L, Watanabe T. Acta metallurgica et materialia 1990;38:2507.
[38] Palumbo G, Lehockey E, Lin P. JOM Journal of the Minerals, Metals and Materials Society 1998;50:40.
[39] Gleiter H. physica status solidi (b) 2006;45:9.
[40] Bishop J, Hill R. Philosophical Magazine Series 7 1951;42:1298.
[41] Field DP, Weiland H. The dependence of dislocation density and cell size on crystallographic orientation in aluminum. Materials Science Forum, vol. 157: Trans Tech Publ, 1994. p.1181.
[42] Winther G, Huang X, Hansen N. Acta Materialia 2000;48:2187.
[43] Sam DD, Adams BL. Metallurgical and materials transactions A 1986;17:513.
[44] Castro S, Gallego J, Landgraf F, Kestenbach HJ. Materials Science and Engineering: A 2006;427:301.
[45] Merriman C, Field D, Trivedi P. Materials Science and Engineering: A 2008;494:28.
[46] Schmid E, Boas W, Rawlins F. The Journal of Physical Chemistry 1935;39:1248.
[47] Hosford WF. The mechanics of crystals and textured polycrystals. New York ; Oxford: Oxford University Press, 1993.
[48] Mises R, Central Electricity Generating Board L. Math Mech 1928;8:161.
[49] Warnes WH. 2011.
[50] Sachs G. Z. Ver. Dtsch. Ing 1928;72:734.
[51] Cox H, Sopwith D. Proceedings of the Physical Society 2002;49:134.
[52] Taylor GI. J. Inst. Met. 1937;62.
[53] Taylor GI. Timoshenko Aniv 1938;Macmillan:218.
[54] Mecking H, Grinberg A. Strength of metals and alloys. Proc. Conf., ICSMA5, ed. P. Haasen y col., Pregamon Press, Nueva York, vol. 1, 1980.
[55] Letters NHAHT, Lilholt H. 1981.
[56] Kocks U. Metallurgical and Materials Transactions B 1970;1:1121.
[57] Kocks U. Acta Metallurgica 1960;8:345.
[58] Partridge P. International Materials Reviews 1967;12:169.
[59] Kocks U, Chandra H. Acta Metallurgica 1982;30:695.
[60] Honneff H, Mecking H. Textures of Materials 1978;1:265.
[61] Tome C, Canova G, Kocks U, Christodoulou N, Jonas J. Acta Metallurgica 1984;32:1637.
[62] Fleischer R. Acta Metallurgica 1987;35:2129.
[63] Hosford W. Acta Metallurgica 1966;14:1085.
[64] Chin G, Nesbitt E, Williams A. Acta Metallurgica 1966;14:467.
[65] Wonsiewicz B, Chin G. Metallurgical and Materials Transactions B 1970;1:2715.
[66] Gottler E. Phil. Mag 1973;28:1057.
[67] Wilson D. Acta Metallurgica 1965;13:807.
[68] Wilson D, Konnan Y. Acta Metallurgica 1964;12:617.
[69] Wu T, Drucker DC. Journal of Applied Mechanics 1967;34:195.
[70] Fisher J, Hart EW, Pry R. Acta Metallurgica 1953;1:336.
[71] Kelly A, Nicholson R. Strengthening methods in crystals. London: Applied Science Publishers Ltd, 1971.
[72] Ashby M, Johnson L. Philosophical Magazine 1969;20:1009.
[73] Nabarro FRN, Basinski ZS, Holt D. Advances in Physics 1964;13:193.
[74] Ma Q, Clarke DR. Journal of Materials Research 1995;10:853.
[75] Stölken J, Evans A. Acta Materialia 1998;46:5109.
[76] Nix WD, Gao H. Journal of the Mechanics and Physics of Solids 1998;46:411.
[77] Gao H, Huang Y. Scripta Materialia 2003;48:113.

[78] Fleck N, Muller G, Ashby M, Hutchinson J. Acta Metallurgica et Materialia 1994;42:475.
[79] Fleck N, Ashby M, Hutchinson J. Scripta materialia 2003;48:179.
[80] Raabe D, Zhao Z, Park S-J, Roters F. Acta Materialia 2002;50:421.
[81] Hansen N, Kuhlmann-Wilsdorf D. Materials Science and Engineering 1986;81:141.
[82] Leffers T. A kinematical model for the plastic deformation of face-centred cubic polycrystals. Metallurgy Department, Danish Atomic Energy Commission Research Establishment Risø, 1975.
[83] Kuhlmann-Wilsdorf D, Wilsdorf H. Acta Metallurgica 1953;1:394.
[84] Chalmers B. Proceedings of the Royal Society of London. Series A-Mathematical and Physical Sciences 1937;162:120.
[85] Livingston J, Chalmers B. Acta metallurgica 1957;5:322.
[86] Hook R, Hirth J. Acta Metallurgica 1967;15:1099.
[87] Howell P, Jones A, Horsewell A, Ralph B. Philosophical Magazine 1976;33:21.
[88] Li JCM. Trans. AIME 1963;227:239.
[89] Hirth JP. Metallurgical and Materials Transactions B 1972;3:3047.
[90] Hull D. Introduction to dislocation. (The Commonwealth and international library: Structures and solid body mechanics division). Oxford ; New York: Pergamon Press, 1968. p.P22.
[91] Kocks U, Embury J, Cotton J, Chen S, Beaudoin A, Wright S, Rollett A. The Metallurgical Society of AIME, Warrendale (PA) 1994:459.
[92] Schwartz AJ. Electron backscatter diffraction in materials science. New York: Springer, 2009.
[93] Huang X, Winther G. Philosophical Magazine 2007;87:5189.
[94] Lang A. Journal of Physics D: Applied Physics 1999;26:A1.
[95] Wilkens M. Physica status solidi (a) 1970;2:359.
[96] Barabash R. Materials Science and Engineering: A 2001;309:49.
[97] Ungár T. Materials Science and Engineering: A 2001;309:14.
[98] Wilkinson AJ, Britton TB. Materials Today 2012;15:366.
[99] Chen D, Kuo J-C, Wu W-T. Ultramicroscopy 2011;111:1488.
[100] Dingley D. Journal of Microscopy 2004;213:214.
[101] Humphreys F. Journal of materials science 2001;36:3833.
[102] Randle V. Materials Characterization 2009;60:913.
[103] Wright SI, Nowell MM, Field DP. Microscopy and Microanalysis 2011;17:316.
[104] Wilkinson A, Dingley D. Acta metallurgica et materialia 1991;39:3047.
[105] Wilkinson A, Dingley D. Acta Metallurgica et Materialia 1992;40:3357.
[106] Mukherjee S, Garmestani H, Chandra N. Scripta metallurgica et materialia 1995;33:93.
[107] Wilkinson AJ, Hirsch PB. Micron 1997;28:279.
[108] Tao X. An EBSD study on mapping of small orientation differences in lattice mismatched heterostructures, 2003.
[109] Wright SI, Nowell MM. Microsc. Microanal 2006;12:72.
[110] Krieger Lassen N, Juul Jensen D, Condradsen K. Automatic recognition of deformed and recrystallized regions in partly recrystallized samples using electron back scattering patterns. Materials Science Forum, vol. 157: Trans Tech Publ, 1994. p.149.
[111] Kunze K, Wright S, Adams B, Dingley D. Texture, Stress, and Microstructure 1993;20:41.
[112] Wright S. Quantification of recrystallized fraction from orientation imaging scans. National Research Council of Canada, Proceedings of the Twelfth International Conference on Textures of Materials(ICOTOM-12). vol. 1, 1999. p.104.

[113] Lehockey E, Lin Y, Lepik O. Electron backscatter diffraction in materials science 2000:247.
[114] Wright SI. Journal of Computer-Assisted Microscopy(USA) 1993;5:207.
[115] Brewer LN, Othon MA, Young LM, Angeliu TM. Microscopy and Microanalysis 2002;8:684.
[116] Field D, Trivedi P, Wright S, Kumar M. Ultramicroscopy 2005;103:33.
[117] Kamaya M, Wilkinson AJ, Titchmarsh JM. Nuclear engineering and design 2005;235:713.
[118] Brewer L, Othon M, Young L, Angeliu T. Microscopy and Microanalysis 2006;12:85.
[119] Brewer LN, Field DP, Merriman CC. Electron Backscatter Diffraction in Materials Science 2009:251.
[120] Arsenlis A, Parks D. Acta Materialia 1999;47:1597.
[121] Kröner E. Continuum theory of dislocations and internal stresses. New York: Springer Verlag, 1958.
[122] Sun S, Adams B, King W. Philosophical Magazine A 2000;80:9.
[123] El-Dasher B, Adams B, Rollett A. Scripta materialia 2003;48:141.
[124] Wheeler J, Mariani E, Piazolo S, Prior D, Trimby P, Drury M. Journal of microscopy 2009;233:482.
[125] Kamaya M, Wilkinson AJ, Titchmarsh JM. Acta Materialia 2006;54:539.
[126] Zisman A, Van Boxel S, Seefeldt M, Van Houtte P. Materials Science and Engineering: A 2008;474:165.
[127] Mishin OV, Godfrey A, Jensen DJ. Electron Backscatter Diffraction in Materials Science 2009:263.
[128] Humphreys FJ, Brough I. Journal of Microscopy 1999;195:6.
[129] Prior DJ, Boyle AP, Brenker F, Cheadle MC, Day A, Lopez G, Peruzzi L, Potts G, Reddy S, Spiess R. American Mineralogist 1999;84:1741.
[130] Humphreys F, Bate P, Hurley P. Journal of Microscopy 2001;201:50.
[131] Wilkinson AJ. Ultramicroscopy 1996;62:237.
[132] Wilkinson A, Meaden G, Dingley D. Materials Science and Technology 2006;22:1271.
[133] Britton T, Wilkinson A. Ultramicroscopy 2011;111:1395.
[134] Britton T, Wilkinson A. Ultramicroscopy 2012.
[135] Britton T, Liang H, Dunne F, Wilkinson A. Proceedings of the Royal Society A: Mathematical, Physical and Engineering Science 2010;466:695.
[136] Benjamin Britton T, Wilkinson AJ. Acta Materialia 2012.
[137] Karamched PS, Wilkinson AJ. Acta Materialia 2011;59:263.
[138] Murphy J, Wilkinson A, Roberts S. Characterisation of plastic zones around crack-tips in pure single-crystal tungsten using electron backscatter diffraction. IOP Conference Series: Materials Science and Engineering, vol. 3: IOP Publishing, 2009. p.012015.
[139] Littlewood P, Britton T, Wilkinson A. Acta Materialia 2011;59:6489.
[140] Littlewood P, Wilkinson A. International Journal of Fatigue 2012.
[141] Littlewood P, Wilkinson A. Acta Materialia 2012;60:5516.
[142] Schwartz AJ. Electron backscatter diffraction in materials science. New York: Springer, 2009. p.p234
[143] Demir E, Raabe D, Zaafarani N, Zaefferer S. Acta Materialia 2009;57:559.
[144] Field D, Merriman C, Allain-Bonasso N, Wagner F. Modelling and Simulation in Materials Science and Engineering 2012;20:024007.
[145] Hardin T, Adams B, Fullwood DT. Advances in Heterogeneous Material Mechanics: Ichmm-2011 2011:169.
[146] Zhang Y. Optimization Methods and Software 1998;10:1.
[147] Britton T, Randman D, Wilkinson A. Journal of Materials Research 2009;24:607.

[148] Murphy JD, Wilkinson AJ, Roberts SG. IOP Conference Series: Materials Science and Engineering 2009;3:012015.
[149] Jiang J, Britton TB, Wilkinson AJ. Philosophical Magazine Letters 2012:1.
[150] Staker MR, Holt DL. Acta Metallurgica 1972;20:569.
[151] Adams BL, Kacher J. Computers, Materials, & Continua 2010;14:185.
[152] Jiang J, Britton T, Wilkinson A. Ultramicroscopy 2013;125:1.
[153] Standard A. Annual book of ASTM standards 1996;3:56.
[154] Pinard PT, Lagacé M, Hovington P, Thibault D, Gauvin R. Microscopy and Microanalysis 2011;17:374.
[155] Jiang J, Britton TB, Wilkinson AJ. Philosophical Magazine Letters 2012;92:580.
[156] Pantleon W, Hansen N. Acta Materialia 2001;49:1479.
[157] Kröner E. Physics of defects 1981;35:217.
[158] Hughes D, Liu Q, Chrzan D, Hansen N. Acta Materialia 1997;45:105.
[159] Kamaya M. Materials Characterization 2009;60:1454.
[160] Kobayashi S, Tsurekawa S, Watanabe T. Acta Materialia 2005;53:1051.
[161] Randle V, Hansen N, Jensen DJ. Philosophical Magazine A 1996;73:265.
[162] Hansen N, Mehl RF, Medalist A. Metallurgical and materials transactions A 2001;32:2917.
[163] Miura H, Sakai T, Andiarwanto S, Jonas J. Philosophical Magazine 2005;85:2653.
[164] Littlewood P, Britton TB, Wilkinson AJ. Acta Materialia 2011;59:6489.
[165] Li JCM. Transactions of the Metallurgical Society of AIME 1963;227:239.
[166] Zhu TT, Bushby AJ, Dunstan DJ. Mater. Technol. 2008;23:193.
[167] Clausen B, Lorentzen T, Leffers T. Acta Materialia 1998;46:3087.
[168] Wright SL, Field DP, Dingley DJ. Electron Backscatter Diffraction in Materials Science 2000:141.
[169] A.D.Rollett. Texture, Microstructure & Anisotropy. 2011.
[170] Bunge HJ. Clausthal, FRG, 25-29 Mar. 1985 1985:1986.
[171] Randle V. The measurement of grain boundary geometry: Institute of Physics Pub., 1993.
[172] Kallend J, Huang Y. Metal science 1984;18:381.
[173] Rajmohan N, Hayakawa Y, Szpunar J, Root J. Physica B: Condensed Matter 1997;241:1225.
[174] Trivedi P, Field DP, Weiland H. International Journal of Plasticity 2004;20:459.
[175] Hansen N, Huang X, Pantleon W, Winther G. Philosophical Magazine 2006;86:3981.
[176] Bunge HJ. Statistical crystallography of the polycrystal. Materials Science Forum, vol. 157: Trans Tech Publ, 1994. p.13.
[177] Wagner F, Allain-Bonasso N, Berbenni S, Field DP. On the Use of EBSD to Study the Heterogeneity of Plastic Deformation. Materials Science Forum, vol. 702: Trans Tech Publ, 2012. p.245.
[178] Zaefferer S, Kuo JC, Zhao Z, Winning M, Raabe D. Acta Materialia 2003;51:4719.
[179] Kanjarla AK, Van Houtte P, Delannay L. International Journal of Plasticity 2010;26:1220.
[180] Van Houtte P, Li S, Seefeldt M, Delannay L. International Journal of Plasticity 2005;21:589.
[181] Liu Q, Hansen N. Physica status solidi (a) 1995;149:187.
[182] Kawasaki Y, Takeuchi T. Scripta Metallurgica 1980;14:183.
[183] Mughrabi H, Ungar T, Kienle W, Wilkens M. Philosophical Magazine A 1986;53:793.
[184] Allain-Bonasso N, Wagner F, Berbenni S, Field DP. Materials Science and Engineering: A 2012.
[185] Armstrong R, Codd I, Douthwaite R, Petch N. Philosophical Magazine 1962;7:45.
[186] Wert JA, Huang X, Winther G, Pantleon W, Poulsen HF. Materials Today 2007;10:24.

[187] Flinn J, Field D, Korth GE, Lillo TM, Macheret J. Acta Materialia 2001;49:2065.
[188] Llanes L, Laird C. Materials Science and Engineering: A 1992;157:21.
[189] Field D, True B, Lillo T, Flinn J. Materials Science and Engineering: A 2004;372:173.